



# Anisotropies in (Ga,Mn)As

Measurement, Control and Application in Novel Devices

Dissertation

zur Erlangung des  
naturwissenschaftlichen Doktorgrades  
der Julius-Maximilians-Universität Würzburg

vorgelegt von  
Katrín Pappert  
aus Mühlhausen\Thür.

Würzburg 2007

Eingereicht am: 3. Mai 2007

bei der Fakultät für Physik und Astronomie

Gutachter der Dissertation:

1. Gutachter: Prof. Dr. L.W. Molenkamp
2. Gutachter: Prof. Dr. R. Claessen
3. Gutachter: Prof. Dr. T. Dietl

Prüfer im Promotionskolloquium:

1. Prüfer: Prof. Dr. L.W. Molenkamp
2. Prüfer: Prof. Dr. R. Claessen
3. Prüfer: Prof. Dr. R. Oppermann

Tag des Promotionskolloquiums: 3. Juli 2007

Doktorurkunde ausgehändigt am: ...

**Parts of this thesis have been published elsewhere; other manuscripts are in preparation:**

- C. Gould, K. Pappert, C. Rüster, R. Giraud, T. Borzenko, G. M. Schott, K. Brunner, G. Schmidt, and L. W. Molenkamp, *Current Assisted Magnetization Switching in (Ga,Mn)As Nanodevices* Japanese Journal of Applied Physics Vol. **45**, No. 5A, 3860 (2006); cond-mat/0602135
- K. Pappert, M. J. Schmidt, S. Hümpfner, C. Rüster, G.M. Schott, K. Brunner, C. Gould, G. Schmidt, and L.W. Molenkamp *Magnetization-Switched Metal-Insulator Transition in a (Ga,Mn)As Tunnel Device* Physical Review Letters **97**, 186402 (2006); cond-mat/0608683
- K. Pappert, S. Hümpfner, J. Wenisch, K. Brunner, C. Gould, G. Schmidt, and L.W. Molenkamp, *Transport Characterization of the Magnetic Anisotropy of (Ga,Mn)As*, Applied Physics Letters **90**, 062109 (2007); cond-mat/0611156.
- C. Gould, K. Pappert, G. Schmidt and L.W. Molenkamp, *Magnetic Anisotropies and (Ga,Mn)As Based Spintronic Devices*, Advanced Materials **19**, 323 (2007).
- S. Hümpfner, K. Pappert, J. Wenisch, K. Brunner, C. Gould, G. Schmidt, and L.W. Molenkamp, *Lithographic Engineering of Anisotropies in (Ga,Mn)As*, Applied Physics Letters **90** 102102 (2007); cond-mat/0612439.
- J. Wenisch, C. Gould, L. Ebel, J. Storz, K. Pappert, M.J. Schmidt, C. Kumpf, G. Schmidt, K. Brunner, and L.W. Molenkamp, *Control of Magnetic Anisotropy in (Ga,Mn)As by Lithography-induced Strain Relaxation*, submitted, cond-mat/0701479
- K. Pappert, S. Hümpfner, C. Gould, J. Wenisch, K. Brunner, G. Schmidt, and L.W. Molenkamp, *Exploiting Locally Imposed Anisotropies in (Ga,Mn)As: a Non-volatile Memory Device*, Nature Physics advance online publication, 1 July 2007 (DOI 10.1038/nphys652); cond-mat/0701478
- M.J. Schmidt, K. Pappert, C. Gould, G. Schmidt, R. Oppermann, L.W. Molenkamp, *Bound Hole States in a Ferromagnetic (Ga,Mn)As Environment*, submitted; cond-mat/0704.2028



# Contents

<b>Zusammenfassung</b>	<b>4</b>
<b>Summary</b>	<b>8</b>
<b>1 Introduction</b>	<b>9</b>
<b>2 The Ferromagnetic Semiconductor (Ga,Mn)As</b>	<b>13</b>
2.1 Ferromagnetism in (Ga,Mn)As . . . . .	13
2.2 Anisotropic Transport Properties . . . . .	14
2.2.1 Anisotropic Magnetoresistance . . . . .	14
2.2.2 Planar Hall Effect . . . . .	15
2.3 Magnetic Anisotropy . . . . .	16
2.3.1 Typical Anisotropy of (Ga,Mn)As Layers . . . . .	16
2.3.2 Shape Anisotropy . . . . .	18
2.3.3 Magnetization Reversal . . . . .	19
<b>3 Analyzing Magnetization Behaviour in Transport</b>	<b>23</b>
3.1 Biaxial Magnetic Anisotropy . . . . .	23
3.1.1 The Anisotropy Fingerprint Technique . . . . .	27
3.1.2 Signature of a $\langle 010 \rangle$ Uniaxial Term . . . . .	29
3.1.3 Signature of a $\langle \bar{1}10 \rangle$ Uniaxial Term . . . . .	30
3.1.4 (Ga,Mn)As at 4 K - A Fingerprint Gallery . . . . .	33
3.2 Uniaxial Magnetic Anisotropy . . . . .	37
3.3 Temperature Dependence of the (Ga,Mn)As Anisotropy . . . . .	41
<b>4 Current Assisted Magnetization Manipulation</b>	<b>49</b>
<b>5 Magnetization-Switched MIT in a TAMR Device</b>	<b>55</b>
5.1 Previous Work . . . . .	55
5.1.1 Tunnelling Anisotropic Magnetoresistance (TAMR) . . . . .	55
5.1.2 TAMR in an Epitaxial Structure . . . . .	57
5.2 Origin of the Giant Amplification . . . . .	58
5.2.1 The Metal Insulator Transition (MIT) . . . . .	59
5.2.2 Density of States Spectroscopy . . . . .	59

---

5.2.3	The Wave Function Overlap Determines the MIT . . . . .	62
<b>6</b>	<b>Lithographic Engineering of Anisotropies</b>	<b>65</b>
6.1	Nanobars . . . . .	66
6.2	SQUID Investigations . . . . .	67
6.3	Transport Characterization . . . . .	68
6.4	Anisotropic Strain Relaxation . . . . .	71
6.5	Strength of the Induced Anisotropy . . . . .	73
<b>7</b>	<b>Exploiting Locally Imposed Anisotropies in (Ga,Mn)As</b>	<b>77</b>
7.1	Device Operation . . . . .	78
7.2	Magnetic States . . . . .	80
7.3	Origin of the Resistance Signal . . . . .	81
7.4	Domain Wall Manipulation . . . . .	84
7.5	Detailed Magnetoresistance Measurements . . . . .	88
7.6	A Non-volatile Memory Cell . . . . .	90
<b>8</b>	<b>Conclusions and Outlook</b>	<b>91</b>
	<b>Bibliography</b>	<b>93</b>

# Zusammenfassung

Ferromagnetische Halbleiter (ferromagnetic semiconductors, FS) versprechen die Integration von magnetischen Eigenschaften für Speicheranwendungen und halbleitenden Eigenschaften zur Informationsverarbeitung innerhalb des selben Materialsystems. (Ga,Mn)As ist als Modellsystem in den letzten Jahren in den Fokus der Halbleiterspintronik gerückt. Die Kopplung der magnetischen und elektrischen Eigenschaften über die Spin-Bahnwechselwirkung ist die Ursache vieler neuer Transportphänomene in diesem Materialsystem. Sie sind vielfach die Grundlage für neuartige Anwendungen, Bauteil-Designs und Wirkprinzipien. In dieser Arbeit beschäftigen wir uns mit den Herausforderungen, die die Entwicklung einer halbleitenden Speicher- und Informationsverarbeitungsarchitektur mit sich bringt. Der besondere Fokus liegt hierbei auf den Speicheranwendungen.

Die genaue Kenntnis der magnetischen Anisotropie ist die Grundlage für die magnetische Informationsspeicherung in FS. Der erste Teil der Arbeit beschäftigt sich deshalb mit der Untersuchung des Verhaltens der Magnetisierung in kompressiv verspannten (Ga,Mn)As Schichten durch elektrische Messungen. Bei Magnetfeld-Scans entlang vieler Richtungen in der Schichtebene wird der von Strom und Magnetisierung eingeschlossene Winkel mittels des Anisotropen Magnetowiderstandseffektes (AMR) [Baxt 02] oder des Planaren Hall Effektes (PHE) [Tang 03] beobachtet. Eine vollständige winkelabhängige Reihe solcher Messungen, dargestellt in einem farbkodierten Widerstandspolardiagramm, kann zur Identifizierung und quantitativen Bestimmung der Symmetriekomponenten der magnetischen Anisotropie von (Ga,Mn)As bei 4 K verwendet werden. Solche "Anisotropiefingerabdrücke" werden von vielen (Ga,Mn)As Schichten aus Würzburg und anderen Laboratorien aufgenommen; alle bestätigen das Vorhandensein von drei Anisotropiekomponenten bei 4 K. Der vierzählige Anteil mit weichen Achsen entlang der [100] und [010] Kristallrichtung dominiert die magnetischen Eigenschaften. Ein weiterer Anteil, mit zweizähliger Symmetrie, mit typischerweise einer Anisotropiekonstante von etwa 10% der vierzähligen, hat seine weiche Achse entlang einer der beiden  $\langle 110 \rangle$  Richtungen. Eine zweite zweizählige Komponente mit weicher Achse entlang [100] oder [010] [Goul 04] wird wegen seiner kleinen Anisotropiekonstante (nur 1% der vierzähligen) in SQUID Messungen meist übersehen. Der hier eingeführte Anisotropiefingerabdruck beruht auf der Winkelverteilung der durch Domänenwandnukleation und -ausbreitung hervorgerufenen Schaltvorgänge. Er ist deshalb gegenüber dieser zweiten uniaxialen Anisotropiekompo-

nente besonders empfindlich, da diese eine Symmetriebrechung zwischen den beiden weichen Achsen des vierzähligen Hauptanisotropieanteils verursacht [Cowb 95]. Auch die Temperaturabhängigkeit der magnetischen Anisotropie von (Ga,Mn)As wird untersucht und anschaulich gemacht. Der Übergang von der hauptsächlich vierzähligen Symmetrie bei 4 K zu einer überwiegend zweizähligen Symmetrie nahe der Curie Temperatur, der schon früher in SQUID Studien herausgestellt wurde [Wang 05b], ist aus der Symmetrie der Anisotropiefingerabdrücke intuitiv ablesbar.

Anstelle von Magnetfeldern, wie in den oben gezeigten Beispielen, könnte ein elektrischer Schreibvorgang für kommerziell interessante magnetische Halbleiterspeicher verwendet werden. In unserem Experiment demonstrieren wir strominduziertes Magnetisierungsschalten in einer lateralen (Ga,Mn)As Struktur bei 4 K (weit unter der Curie Temperatur  $T_C$ ). Wir lesen den großen Widerstand aus, der durch das geometrische Confinement von Domänenwänden in Verengungen entsteht [Rust 03]. So kann das stromunterstützte Umschalten der Magnetisierung einer kleinen Insel durch ladungsträgerübermittelten Spin-Transfer (carrier-mediated spin transfer [Tata 04, Yama 04]) von den größeren Zuleitungen nachgewiesen werden.

Eine Möglichkeit zur nicht-zerstörenden Messung des Magnetisierungszustandes eines Halbleiterspeicherelementes ist die Nutzung des Anisotropen Tunnelmagnetowiderstandseffekts (Tunneling Anisotropic MagnetoResistance TAMR) [Goul 04, Rust 05]. In der vorliegenden Arbeit wird der Ursprung der großen Verstärkung des Effektes in einer Struktur mit epitaktisch gewachsenener Tunnelbarriere bei niedrigen Temperaturen untersucht und erklärt. Es wird gezeigt, dass eine dünne (Ga,Mn)As Injektorschicht vom metallischen in den isolierenden Zustand übergeht, wenn die Magnetisierungsrichtung in der Schichtebene gedreht wird. In teilweise verarmtem (Ga,Mn)As hängt die Ausdehnung der gebundenen Wellenfunktionen, die am Hoppingtransport beteiligt sind, von der Magnetisierungsrichtung ab. Deshalb kann eine Drehung der Magnetisierung in einer Schicht nahe dem Metall-Isolatorübergang (metal-insulator-transition, MIT), das Material vom ungeordnet metallischen (disordered metal [Alts 79]) Zustand durch das Perkollationslimit in den isolierenden Zustand versetzen. Diese Zustände nahe dem MIT sind durch eine weiche Energielücke (soft gap) in der Zustandsdichte nahe der Fermienergie charakterisiert. Zustände auf der metallischen Seite des MIT können leicht von Zuständen auf der isolierenden Seite (mit Efros-Shklovskii-Gap [Efro 75]) am Anstieg der Tunnelleitfähigkeitskennlinie unterschieden werden.

Magnetische Eigenschaften von (Ga,Mn)As Strukturen waren bisher nicht einzeln einstellbar, sondern immer von der unstrukturierten Mutterschicht ererbt. Um den Anforderungen von komplexeren Architekturen und Designs gerecht zu werden, wird hier eine Methode eingeführt, um erstmals die magnetische Anisotropie lokal zu kontrollieren. In ferromagnetischen Metallen wird die Anisotropie routinemäßig durch Formanisotropie eingestellt. Berechnungen für typische (Ga,Mn)As Strukturen ergeben aber eine ver-



nachlässigbar kleine Formanisotropie verglichen mit der wesentlich grösseren kristallinen Anisotropie, was hauptsächlich durch die kleine Volumenmagnetisierung bedingt ist und dazu führt, dass Formanisotropie in (Ga,Mn)As nicht angewendet werden kann.

Wir zeigen eine neuartige Methode zur lokalen Einstellung der magnetischen Anisotropie, die auf der Mikrostrukturierung und der damit verbundenen anisotropen Relaxation des Kristallgitters beruht. SQUID- und Transportmessungen demonstrieren die uniaxiale magnetische Anisotropie der lithographisch definierten Submikrometer-Streifen (Nanobars), die im gesamten Temperaturbereich von 4 K bis zu  $T_C$  die magnetischen Eigenschaften der Strukturen bestimmt.

Im letzten Teil der Arbeit nutzen wir die dargestellte Methode der Anisotropiekontrolle zum Design eines nicht-flüchtigen ferromagnetischen Halbleiter-Speicherelementes. Zwei senkrecht zueinander angeordnete, magnetisch uniaxiale Nanobars sind an einer Ecke über eine Verengung elektrisch verbunden. Die relative Orientierung ihrer Magnetisierungsvektoren wird durch ein Magnetfeld eingestellt. Der geschriebene Magnetisierungszustand bleibt bei ausgeschaltetem Feld erhalten und ist durch die Messung des elektrischen Widerstandes der Verengung auslesbar. Feldlinienbilder der verschiedenen magnetischen Zustände in Kombination mit dem AMR Effekt können dieses Verhalten erklären. Das Auslesesignal, also der Widerstandsunterschied zwischen den Zuständen, kann bedeutend verstärkt werden, indem eine Struktur mit teilweise verarmter Verengung verwendet wird. Wie in der TAMR Struktur, ist die Verstärkung auf einen Metall-Isolator-Übergang beim Drehen der Magnetisierung zurückzuführen. Die anisotrope Wellenfunktion der gebundenen Löcher in verarmtem (Ga,Mn)As ist in Richtung der Magnetisierung abgeflacht. Der für den Hoppingtransport entscheidende Überlapp der einzelnen Wellenfunktionen in Stromrichtung ist dadurch vom Winkel zwischen Strom und Magnetisierung abhängig, was den beobachteten verstärkten AMR Effekt mit umgekehrtem Vorzeichen hervorruft.

Das vorgestellte Design für ein Halbleiter-Speicherelement beruht auf ähnlichen Prinzipien wie die Struktur, die zur Demonstration des stromassistierten Magnetisierungsschreibens verwendet wurde. Wir sind deshalb zuversichtlich, dass sich das elektrische Schreiben des Magnetisierungszustandes in einem solchen oder ähnlichen Design verwirklichen lässt. Damit entstünde eine elektrisch beschreib- und auslesbare halbleitende Speicherzelle.



# Summary

Ferromagnetic semiconductors (FS) promise the integration of magnetic memory functionalities and semiconductor information processing into the same material system. The prototypical FS (Ga,Mn)As has become the focus of semiconductor spintronics research over the past years. The spin-orbit mediated coupling of magnetic and semiconductor properties in this material gives rise to many novel transport-related phenomena which can be harnessed for device applications. In this thesis we address several challenges faced in the development of an all-semiconductor memory and information processing architecture, focussing especially on memory applications.

A starting point for information storage in FS is the knowledge of their detailed magnetic anisotropy. The first part of this thesis concentrates on the investigation of the magnetization behaviour in compressively strained (Ga,Mn)As by electrical means. The angle between current and magnetization is monitored in magnetoresistance (MR) measurements along many in-plane directions using the Anisotropic MR (AMR) [Baxt 02] or Planar Hall effect (PHE) [Tang 03]. It is shown, that a full angular set of such measurements displayed in a color coded resistance polar plot can be used to identify and quantitatively determine the symmetry components of the magnetic anisotropy of (Ga,Mn)As at 4 K. We compile such "anisotropy fingerprints" for many (Ga,Mn)As layers from Würzburg and other laboratories and find the presence of three symmetry terms in all layers. The biaxial anisotropy term with easy axes along the [100] and [010] crystal direction dominates the magnetic behaviour. An additional uniaxial term with an anisotropy constant of  $\sim 10\%$  of the biaxial one has its easy axis along either of the two  $\langle 110 \rangle$  directions. A second contribution of uniaxial symmetry with easy axis along one of the biaxial easy axes has a strength of only  $\sim 1\%$  of the biaxial anisotropy and is therefore barely visible in standard SQUID measurements. The anisotropy fingerprint method relies on the angular distribution of the domain wall (DW) nucleation / propagation related switching events. It is therefore especially sensitive to this second uniaxial anisotropy component, which is responsible for the symmetry breaking between the two  $\langle 100 \rangle$  directions [Cowb 95]. Furthermore we investigate and visualize the temperature dependence of the magnetic anisotropy. The transition from a mainly biaxial to a mainly uniaxial magnetic anisotropy reported earlier from SQUID studies [Wang 05b] is intuitively apparent from the symmetry of our fingerprints.

Instead of writing the information into FS elements by a magnetic field, as in the above laboratory demonstrations, an all-electrical writing scheme would be desirable for commercialization. Here we report on a current assisted magnetization manipulation experiment in a lateral (Ga,Mn)As nanodevice at 4 K (far below the Curie temperature  $T_C$ ). Reading out the large resistance signal from DW that are confined in nanoconstrictions [Rust 03], we demonstrate the current assisted magnetization switching of a small central island through a hole mediated spin transfer from the adjacent leads [Tata 04, Yama 04].

One possible non-perturbative read-out scheme for FS memory devices could be the recently discovered Tunneling Anisotropic MagnetoResistance (TAMR) effect [Goul 04, Rust 05]. Here we clarify the origin of the large amplification of the TAMR amplitude in a device with an epitaxial GaAs tunnel barrier at low temperatures. We prove with the help of density of states spectroscopy that a thin (Ga,Mn)As injector layer undergoes a metal insulator transition upon a change of the magnetization direction in the layer plane. The effect can be explained with the magnetization direction dependent wave function extend of bound hole states in partly depleted (Ga,Mn)As. The magnetization reorientation causes a change in the wave function extend, driving the material in a thin injector layer through the percolation limit, from the soft gapped insulating [Efro 75] into a disordered metal [Alts 79] state or vice versa. The two states can be distinguished by their typical power law behaviour in the measured conductance vs voltage tunneling spectra [Lee 99].

While all hereto demonstrated (Ga,Mn)As devices inherited their anisotropic magnetic properties from their parent FS layer, more sophisticated FS architectures will require locally defined FS elements of different magnetic anisotropy on the same wafer. Local anisotropy control is easily established in metallic ferromagnets using demagnetization field related effects (shape anisotropy). We show that the same approach is not applicable in FS because of their low volume magnetization. The shape anisotropy contribution for typical FS structures is approximated using the ferromagnetic prism model [Ahar 98] and it is negligible in comparison with the intrinsic crystalline magnetic anisotropy. We present a method to lithographically engineer the magnetic anisotropy of (Ga,Mn)As by submicron patterning. Anisotropic strain relaxation in submicron bar structures (nanobars) and the related deformation of the crystal lattice introduce a new uniaxial anisotropy term in the energy equation. We demonstrate by both SQUID and transport investigations that this lithographically induced uniaxial anisotropy overwrites the intrinsic biaxial anisotropy at all temperatures up to  $T_C$ .

The final section of the thesis combines all the above into a novel device scheme. We use the above described anisotropy engineering to fabricate two orthogonal, magnetically uniaxial, nanobars which are electrically connected through a constriction. We find that the constriction resistance depends on the relative orientation of the nanobar magnetiza-

tions, which can be written by an in-plane magnetic field. This effect can be explained with the AMR effect in connection with the field line patterns in the respective states. The device offers a novel non-volatile information storage scheme and a corresponding non-perturbative read-out method. The read out signal is shown to increase drastically in samples with partly depleted constriction region. This could be shown to originate in a magnetization direction driven metal insulator transition of the material in the constriction region. The latter can be explained with calculations of the wave function extend similar to the ones discussed above to elucidate the giant amplification the TAMR signal. We find that the overlap of the anisotropic wave functions depends on the angle between current and magnetization and causes a strongly amplified inverse AMR signal in partly depleted (Ga,Mn)As.

The presented device design is highly compatible with the lateral nanoconstriction scheme used for the demonstration of current assisted magnetization manipulation. We are thus optimistic, that current induced magnetization writing can be incorporated into a similar device, yielding an all-electrical, all-semiconductor memory cell.



# Chapter 1

## Introduction

The very topical field of spintronics, or spin-electronics, investigates ways to use the spin degree of freedom of carriers in addition to their charge, which is used to encode information in classical electronics. One spin-electronics application, Magnetoresistive Random Access Memory (MRAM), will soon be available to everyone in the marketplace. Built out of magnetic tunnel junctions (MTJ) it provides non-volatile data storage: information is not lost when the instrument is powered down and does not need to be refreshed during operations[Aker 05]. This is especially interesting for portable electronic devices promising instant on/off functionality and reduced battery consumption. MRAM combines non-volatility and low power consumption with other advantages such as relatively fast read and write times and no wear out during write cycles. This makes it a promising candidate as a "universal" memory device, eliminating the need for multiple memory categories e.g. for fast access or cost effective data storage. However, MRAM storage cells, being made out of metallic elements, are part of the metal interconnect layer far away and largely independent from the semiconductor devices below. Magnetic material is used to store data and semiconductor devices to process the information.

A new class of materials, ferromagnetic semiconductors (FS), promises to overcome this restriction, combining magnetic and semiconducting properties within the same material. This was highlighted in a recent review [Awsc 07] describing the tremendous potential of semiconductor spintronics offering not only integratability of memory, information transport and logic operations in the same material system, but also providing a huge variety of novel effects. This enhanced potential for integration suggests that semiconductor based memory devices could become successors/alternatives to technologies such as MRAM.

Some of the most discussed potential applications of FS include the following: Current induced magnetization manipulation is expected to be more effective (lower switching currents) in FS because of their dilute nature [Tata 04, Yama 04] and removing the necessity of magnetic fields from the data storage process and by that overcoming the challenge of half selected bits in the MRAM scheme[Aker 05]. A second and more fundamental point is that FS can provide a spin-polarized carrier source for semiconductor devices which

circumvents the conductance mismatch problem [Schm 00].

The main drawback of FS is the hereto low ferromagnetic transition temperature, limiting the known materials, such as (Ga,Mn)As to laboratory applications. This material, obtained from the standard III-V semiconductor GaAs by doping with magnetic Mn acceptors [Ohno 98], has become the prototypical FS. The spin-orbit mediated coupling of magnetic and semiconductor properties in this material [Diet 00] gives rise to many novel transport-related phenomena which can be harnessed for device applications. Much progress in understanding and implementing FS has been made with the help of this material system. While its Curie temperature of up to 173 K [Wang 04] may, despite large efforts, never reach room temperature, the knowledge gained is expected to port to other FS. Promising material development research is ongoing world wide in the search for a room temperature FS.

As the field of semiconductor spintronics [Awsc 07] continues to mature and more and more of the fundamental issues become resolved, researchers are increasingly turning their attention to harnessing the spin transport properties of magnetic semiconductors into industrially relevant devices. One widely explored avenue towards the design of spintronic devices with novel functionalities is based on using the position of individual domains in FS to store information, and the controlled movement of domain walls to manipulate and transport this information. For such devices to be industrially relevant, schemes are needed that are scaleable to large integration density, where the position of domain walls can be determined by electrical measurements, and where the walls can be manipulated using gate or bias voltages. One paradigm for such a memory device is the "race-track memory" concept which was disclosed by IBM in February 2005 [Park 05], another example is the demonstration of the domain-wall logic framework in ferromagnetic metals by Cowburn and coworkers [Allw 05].

The ultimate goal of an all-electrical all-semiconductor memory architecture poses several challenges in device design, writing, storing and retrieving of the information:

- Local engineering of the magnetic properties in FS to design a memory architecture: Previously reported device concepts in FS including strong anisotropic magnetoresistance (AMR) [Baxt 02], planar Hall effect [Tang 03], tunneling anisotropic magnetoresistance (TAMR) [Goul 04, Rust 05] and Coulomb blockade AMR [Wund 06] have been based on structures which had the same magnetic properties, inherited from the unstructured (Ga,Mn)As layer, throughout the device.
- Writing information into a device by electrical means.
- Storing information in a non-volatile FS device that is compatible with current induced magnetization writing.
- Effective non-perturbative read-out of the information, preferably with a large on/off resistance (current) ratio.



In this thesis we present advances on all these points. Chapter 2 introduces carrier mediated ferromagnetism in (Ga,Mn)As and the resulting transport and magnetic anisotropies of this material. In Ch. 3 a new method of measuring and visualizing the magnetic anisotropy by electrical means is presented. It is shown, with the help of this "anisotropy fingerprint" method, that the magnetic anisotropy of typical (Ga,Mn)As layers at 4 K is determined by three symmetry components; two uniaxial and the main biaxial. Chapter 4 focusses on electrical manipulation of the magnetization state in a lateral nanodevice. Here we show current assisted magnetization switching at 4 K in a (Ga,Mn)As double-constriction. Chapter 5 focusses on information read-out, explaining the giant amplification of the Tunneling Anisotropic MagnetoResistance (TAMR) signal at low temperatures in a device with epitaxial GaAs tunnel barrier. Density of states spectroscopy showed that a thin (Ga,Mn)As injector layer is driven through the metal insulator transition (MIT) by a magnetization reorientation. Chapter 6 presents a method to lithographically engineer the magnetic anisotropy of (Ga,Mn)As locally. Through anisotropic strain relaxation we create magnetically uniaxial "nanobars" by overwriting the parent layer anisotropy. Imposing the magnetic properties locally to various functional elements of the same device allows for the first time devices that are comprised of elements with different magnetic properties. Chapter 7 brings together many of the above advances into one such device. "Nanobars" with different engineered anisotropy are coupled electrically. We show that their relative magnetization state can be used for non-volatile information storage. Furthermore we demonstrate that the electrical read-out signal can be greatly amplified if the depleted material at the connection point between the two bars undergoes a MIT upon magnetization reorientation.

The presented memory concept could be a building block in a non-volatile semiconductor memory architecture. From the design point of view it is suitable for the integration of current driven magnetization manipulation as shown in Ch. 4. We thus believe that it constitutes a significant step forward towards an all-electrical all-semiconductor memory cell. Ch. 8 finally highlights the main conclusions of the presented work and indicates directions for future research.



# Chapter 2

## The Ferromagnetic Semiconductor (Ga,Mn)As

### 2.1 Ferromagnetism in (Ga,Mn)As

(Ga,Mn)As is the prototypical ferromagnetic semiconductor. It rose to its position as the most widely studied ferromagnetic semiconductor after a string of successes in the late 1990's, starting with the demonstration of a 110 K Curie temperature by Matsukura et al.[Mats 98, Ohno 96]. The material is a diluted magnetic semiconductor fabricated by introducing typically 2% to 6% Mn into a GaAs lattice. It thus has the same zinc blende structure as GaAs. The material must be grown at low temperatures (Typically  $\sim 230^\circ\text{C}$  to  $\sim 270^\circ\text{C}$ , compared to the normal  $\sim 600^\circ\text{C}$  for molecular beam epitaxy of GaAs) to avoid MnAs cluster formation. During growth, the Mn incorporates into the lattice principally in two distinct ways: Substitutionally at Ga sites and (in minority) interstitially. The two different types of incorporation lead to very different behavior. Because Mn is not isovalent with Ga, the substitutional Mn act as acceptors, giving the material its p-type doping character. The interstitial Mn on the other hand has donor character, and acts to compensate some of the carriers.

The most widely used theoretical approach to describe ferromagnetism in zinc blende magnetic semiconductors[Haur 97] in general and (Ga,Mn)As in particular, is the p-d mean field Zener model description of carrier mediated ferromagnetism. This model was originally proposed by T. Dietl in 2000 [Diet 00] and subsequently developed more thoroughly in [Diet 01] and [Abol 01]. In these works, the exchange coupling between the itinerant holes inside the (Ga,Mn)As  $sp^3$  valence band and the localized magnetic moments of the Mn 3d valence states is treated using a mean field approximation. Conceptually the physical mechanism leading to ferromagnetism[Ohno 02, Diet 02] can be understood as follows: The substitutional Mn impurities in GaAs are incorporated in a  $\text{Mn}^{2+}$  valence configuration which leads to localized magnetic moments of spin  $S=5/2$ , according to Hund's rules. The shallow acceptor Mn contributes a hole to the GaAs valence band.

The sp-d interactions between valence band holes and Mn-3d valence states are treated as an effective magnetic field acting on the delocalized hole system. The spin states in the valence band split in the presence of this magnetic field. The band splitting minimizes the energy of the free carrier system, while on the other hand the free energy of the localized magnetic spins is increased by the spontaneous magnetization. This energy cost of aligning the manganese moments is smaller at lower temperatures and below a given  $T$  will be less than the energy gain from redistributing the holes in the valence band. This is the Curie temperature  $T_C$  below which the system is ferromagnetic according to the mean field Zener model [Diet 00]. All Mn spins in regions visited by the quasi-freely propagating holes align ferromagnetically resulting in a long-range ferromagnetic order.

This spin-orbit mediated coupling of magnetic and semiconductor properties gives rise to many novel transport-related phenomena in (Ga,Mn)As (see the following section) which can be harnessed for device applications. (Ga,Mn)As' main handicap is however its low Curie temperature which currently excludes it from industrial applications. While Curie temperatures of up to 173 K [Wang 04], which have been achieved using low-temperature post-growth annealing, currently limit it to laboratory applications, none of the effects investigated needs to be unique to (Ga,Mn)As. Quite to the contrary, most of the effects are very likely to be present also in other magnetic semiconductors or even in metals with strong spin-orbit coupling. We thus believe that knowledge gained through the investigation of the prototypical semiconductor (Ga,Mn)As will be portable to other material systems.

## 2.2 Anisotropic Transport Properties

Ferromagnets in general and the ferromagnetic semiconductor (Ga,Mn)As in particular exhibit anisotropic transport properties. These are typically investigated in Hall-bar-like structures, where the longitudinal and/or transverse four probe resistance is recorded as a function of an applied magnetic field (magnetoresistance measurement, MR).

### 2.2.1 Anisotropic Magnetoresistance

(Ga,Mn)As shows a strong anisotropic magnetoresistance effect (AMR): The resistivity for a current flow perpendicular to the magnetization is larger than parallel to the magnetization[Baxt 02]. The resistivity  $\rho$  is thus no longer a number, but rather a tensor, and Ohm's law relating the electric field  $\mathbf{E}$  to the current  $\mathbf{J}$  is best expressed with the electric field broken up in components parallel and perpendicular to the magnetization  $\mathbf{M}$  [Jan 57, McGu 75]

$$\mathbf{E} = \rho_{\parallel}\mathbf{J}_{\parallel} + \rho_{\perp}\mathbf{J}_{\perp} \quad (2.1)$$

A projection onto the current path gives the longitudinal resistivity  $\rho_{xx}$

$$\rho_{xx} = \rho_{\perp} - (\rho_{\perp} - \rho_{\parallel}) \cos^2(\vartheta), \quad (2.2)$$

where  $\vartheta$  is the angle between  $\mathbf{M}$  and  $\mathbf{J}$ . If the magnetization in a Hall bar sample is rotated in the sample plane by a strong external magnetic field, a sinusoidal behaviour of the longitudinal resistance  $R_{xx}$  with respect to the field angle is thus expected.

The AMR effect is not yet fully understood at the first principle level, although various models exist for rare earth and 3d transition metals, where  $\rho_{\perp} < \rho_{\parallel}$ , in opposition to (Ga,Mn)As [Ohan 00, Jung 07]. Moreover there are experimental observations of the AMR in (Ga,Mn)As depending on the crystal direction of the current flow [Mats 04]. Recently it has been shown, that crystal direction dependent terms of the AMR play an increasing role in thin (Ga,Mn)As films, where not only the amplitude, but also the sign of the AMR can differ from those observed in thicker layers [Rush 06]. In chapter 7 we report on observations of a large inverse AMR effect in a depleted constriction and discuss its origin.

Additional to the AMR effect, (Ga,Mn)As samples typically show an almost linear isotropic decrease of resistance with increasing magnetic induction [Goen 05]. Its amplitude is sample dependent. This negative isotropic magnetoresistance effect is a result of a magnetic field dependent scattering rate as described in detail by Matsukura et al. [Mats 04].

### 2.2.2 Planar Hall Effect

It is well known in non-magnetic materials, that a magnetic field  $\mathbf{H}$  perpendicular to a Hall bar causes a Lorentz force and thus deflects the charge carriers from their path. An electric field is thus built up perpendicular to both the current and  $\mathbf{H}$ , leading to the ordinary Hall Effect.

Combining the anisotropic resistivity tensor discussed in relation to AMR with the spontaneous magnetization, it is clear that a ferromagnetic semiconductor can develop a spontaneous Hall voltage in response to fields and magnetization in the plane of the structure. This transverse voltage depends on the magnetization direction with respect to the current path, similar to the AMR. The dependence of the Hall resistivity  $\rho_{xy}$  on the magnetization direction follows directly from electric field component perpendicular to the current path.  $\rho_{xy}$  calculated from equation 2.1 is thus

$$\rho_{xy} = -\frac{\rho_{\perp} - \rho_{\parallel}}{2} \sin(2\vartheta), \quad (2.3)$$

In particular, if a magnetic field is applied in the sample plane, it can change the in-plane magnetization direction and thus the Hall resistance. This effect is called transverse AMR

or planar Hall effect (PHE) [Tang 03]. If a field of constant high amplitude is rotated in the sample plane  $R_{xy}$  has a sinusoidal dependence on the field angle, with no offset and extrema at  $\pm 45^\circ$  with respect to the current direction.

## 2.3 Magnetic Anisotropy

### 2.3.1 Typical Anisotropy of (Ga,Mn)As Layers

As one would expect from the symmetry rules governing the zinc blende structure, the magnetocrystalline anisotropy of bulk (Ga,Mn)As is cubic. The three symmetrically equivalent  $\langle 100 \rangle$  or four  $\langle 111 \rangle$  crystal directions are theoretically predicted preferred axes of magnetization (easy axes) reflecting the anisotropy of the crystals that is coupled to the magnetic properties via spin-orbit coupling. Experimentally easy axes along the  $\langle 111 \rangle$ -directions have never been observed. Given that (Ga,Mn)As is grown epitaxially, in practice, one never deals with the pure bulk properties, and the effect of the substrate on which the layer is grown will have an impact on its anisotropy. While there has been some recent interest in the growth of (Ga,Mn)As on substrates of various crystal orientations [Zung 05, Maha 04, Wang 05a, Omiy 01], the vast majority of work, including the studies in this thesis, has been done on  $[001]$  oriented substrates.

Due to a mismatch in lattice constants, (Ga,Mn)As layers grown on substrates will be strained in the growth direction, and exhibit an additional uniaxial anisotropy perpendicular to the layer. The (Ga,Mn)As layer can be tensile strained if grown on a substrate of larger lattice constant, such as for  $\text{In}_x\text{Ga}_{1-x}\text{As}$  buffers (with  $x \sim 8\%$ ) or compressively strained in the opposite case, such as with our GaAs buffers [Shen 97]. The former results in a strong out-of plane easy axis, and has been investigated in detail by [Liu 05, Xian 05]. Compressively strained (Ga,Mn)As exhibits rich anisotropy behaviour with the perpendicular to plane axis being easy or hard depending on the layer characteristics. In particular, the out of plane axis is easy for low doped layers, at very low temperatures [Sawi 04], with the easy axis falling into the plane only at temperatures closer to their Curie temperature. However, for the high hole concentration samples more commonly used in transport investigations, the layers usually show a strong hard axis perpendicular to the sample plane [Sawi 04]. From the above it is obvious that the (Ga,Mn)As magnetic anisotropy reacts sensitively to external strain. In chapter 6 we discuss how strain, and in particular strain relaxation, can be used to engineer in-plane magnetic anisotropies in a (Ga,Mn)As device locally.

While low-temperature annealing can help to increase the Curie temperature of the material, Ref. [Sawi 04] also suggests potential perils in using this technique. The authors show not only that the anisotropy of a given sample depends on its temperature, but also that the transition temperature at which easy axis reorientation takes place is dependent on the carrier concentration. Thus, as annealing causes an increase in carrier density, it can trigger a reorientation of the sample anisotropy for measurements at any given

temperature. This is not only the case for the out-of-plane to in-plane reorientation, but the dependence on carrier concentration also applies to in-plane anisotropy reorientations which play an important role in transport studies. Low-temperature processing is thus critical for (Ga,Mn)As devices and all samples discussed here were structured on as-grown (not annealed) material with minimal heat load to prevent accidental annealing.

In transport samples patterned on highly doped (Ga,Mn)As layers, for experimentally relevant hole densities, the easy axis is typically confined to the plane, but shows an important temperature dependence resulting from the interplay between three anisotropy components: The main biaxial anisotropy component yielding easy axes along [100] and [010], a uniaxial anisotropy term with easy axis along [110] or  $\bar{[110]}$  and a much smaller uniaxial anisotropy component with easy axis along [010] or [100] [Goul 04, Papp 07]. Because the biaxial anisotropy scales with  $M^4$  while the uniaxial goes as  $M^2$ , as the temperature approaches  $T_C$  and  $M$  decreases, the dominant anisotropy term changes from biaxial to uniaxial with increasing temperature [Wang 05b]. Summing up the anisotropy terms of different symmetry we can express the magnetostatic energy  $E$  of a magnetic domain with magnetization orientation  $\vartheta$  with respect to the [100]-crystal direction in the layer plane:

$$E = \frac{K_{cryst}}{4} \sin^2(2\vartheta) + K_{uni[\bar{110}]} \sin^2(\vartheta - 135^\circ) + K_{uni[010]} \sin^2(\vartheta - 90^\circ) - MH \cos(\vartheta - \varphi) \quad (2.4)$$

The first term describes the biaxial crystalline anisotropy contribution and the last term is the Zeeman energy. The origin of the [110] uniaxial term ( $K_{uni[\bar{110}]}$ ) is not yet fully understood. Theoretical models predict a  $\langle 110 \rangle$  anisotropy term [Wang 05b], but it is important to realize that this is a prediction of a biaxial easy axis along [110] and  $\bar{[110]}$ , and cannot account for the uniaxial behaviour observed empirically [Sawi 05] because there is nothing in the model to break the symmetry between the  $\langle 110 \rangle$  directions. So far, there is only speculation about the origin of this symmetry breaking. While the unrelaxed strain resulting from growth breaks the symmetry between the in-plane and the out-of-plane directions, no in-plane uniaxial axis would yet be expected. Moreover, the observed anisotropy field is found to be independent of layer thickness or of etching the surface, which appears to rule out surface effects. It is important to note, however, that the bulk symmetry may be reduced, either due to surface reconstruction effects on the GaAs buffer surface [Welp 03, Welp 04], or due to the finite thickness of the layer and a difference between the substrate/layer and layer/air interfaces. The true nature of this symmetry breaking however remains an open question, as no method of detection other than studies of the magnetic anisotropy, has yet been able to identify any symmetry breaking factors. The experimental proof of the existence of the additional small [010] anisotropy ( $K_{uni[010]}$  in equ. 2.4) will be discussed in section 3.1.1. Its source is also not understood theoretically, and given that it violates even the reduced group symmetry

rules for the (Ga,Mn)As structure with asymmetric interfaces [Sawi 04], it is likely to result from some extrinsic effect such as strain or magnetostriction, or from a symmetry breaking resulting from details of the growth. While the existence of such an anisotropy is unexpected and so far defies explanation, it is not unique to (Ga,Mn)As, as the same anisotropy has also been observed empirically in some epitaxial Fe layers grown on a GaAs substrate by Cowburn et.al. [Cowb 95].

Note however, that any linear combination of uniaxial anisotropy components with different easy axes can be expressed as a linear combination of  $[\bar{1}10]$  and  $[010]$  uniaxial anisotropy terms. It is known that:

$$a \sin \alpha + b \cos \alpha = \sqrt{a^2 + b^2} \cdot \sin(\alpha + \beta), \quad (2.5)$$

where  $\beta$  is given by  $\arctan(b/a)$  and  $\arctan(b/a) \pm \pi$  if  $a \geq 0$  and  $a < 0$  respectively. This relates two sine functions of the same period but with different phase to a third sine function with the same period and a new phase. Consequently, we can express any combination of two uniaxial anisotropy components in a (Ga,Mn)As layer by an equivalent linear combination of the  $[110]$  and the  $[010]$  uniaxial anisotropy term. The choice of only these two directions is thus in no way unique and does not exclude other uniaxial anisotropy components, e.g. due to specific strain conditions in a specific sample.

### 2.3.2 Shape Anisotropy

In addition to the magnetocrystalline and strain anisotropies discussed so far, which govern bulk and film behaviour, one might also expect shape anisotropy in patterned micro- and nano-structures, which has been widely used with metallic ferromagnets such as cobalt or iron [OHan 00]. Shape anisotropy describes the phenomenon that a long ferromagnetic rod or stripe is preferably magnetized along its long axis. Furthermore, the necessary external field for reversing the magnetization is larger, the narrower a stripe of the same length is. It is thus possible to switch parts of a sample independently and to set up different magnetic configurations in, for example, a pair of ferromagnetic metallic wires. It is important to note however that the strength of shape anisotropy depends on the saturation magnetization of the material, which is much smaller for (Ga,Mn)As than for ferromagnetic metals.

Shape anisotropy can be described as a uniaxial energy term that contributes to the total energy of the magnetic stripe. The magnetostatics energy equation thus contains a uniaxial energy term  $K_{uni} \sin^2(\vartheta - \vartheta_{uni})$  in addition to the terms in equ. 2.4. Note however that shape anisotropy is only one possible origin for uniaxial magnetic anisotropy. In this case  $K_{uni} = K_{shape}$  and  $\vartheta_{uni}$  denotes the direction parallel to the long edge of the ferromagnetic stripe. Based purely on magnetostatics considerations,  $K_{shape}$  is proportional to the saturation magnetization  $M_s$  squared [OHan 00]:



$$K_{shape} = \Delta N \frac{\mu_0 M_s^2}{2} \quad (2.6)$$

Even at 4 K,  $\mu_0 M_s$  is much lower in (Ga,Mn)As ( $\sim 0.05$  T) than in typical metallic ferromagnets (for example  $\sim 0.6$  T in Ni and  $\sim 2.2$  T in Fe) [Sawi 04].  $\Delta N$  is the difference in demagnetizing factors, which describes the geometry of the ferromagnet. For an infinitely long cylindrical rod  $N=1/2$  and  $K_{shape}$  would approximate to  $500 \text{ J/m}^3$ . However, typical (Ga,Mn)As nanostructures are made from thin epitaxial films. In the case of films grown on GaAs (001) substrates the magnetization is confined to the film plane because of growth strain. To estimate the typical shape anisotropy contribution in the plane, we calculate the demagnetizing factors for a typical sub-micron (Ga,Mn)As stripe structure (20 nm thick, 200 nm wide and  $1 \mu\text{m}$  long) using Aharoni's formulas for a rectangular ferromagnetic prism [Ahar 98]. In this model ratios of all three dimensions thickness, length and width of the structure are taken into account. The difference between the two in-plane demagnetizing factors parallel and perpendicular to the stripe is  $N=0.09$  and thus  $K_{shape} \sim 80 \text{ J/m}^3$ . Consequently the shape effect is very small compared to the biaxial crystalline anisotropy  $K_{cryst} \sim 3000 \text{ J/m}^3$ , which suggests caution when examining previous reports of shape anisotropy in (Ga,Mn)As at 4 K [Hama 03] or 10 K [Hama 06]. As we will discuss in detail in chapter 6, strain relaxation in sub-micron structures induces a uniaxial magnetic anisotropy which at a first glance may look similar to the above described effects of the demagnetizing field.

### 2.3.3 Magnetization Reversal

In addition to the anisotropy, another important aspect governing the behaviour of (Ga,Mn)As based devices is the mechanism by which the magnetization is reversed when subjected to a varying external field. Domains in (Ga,Mn)As have a characteristic size exceeding hundreds of microns [Welp 03] (in the presence of a strong out-of-plane hard magnetic axis as discussed in sec. 2.3.1). The magnetization reversal proceeds through the formation and expansion of well defined domains, as it does in the case of conventional metallic ferromagnets. This means that during, for example magnetoresistance measurements, single domains can be larger than typical transport structures, which can, for many purposes, be treated within a single domain model (using eq. 2.4). This of course will not always be the case, as patterning of the device may stimulate the breaking up of the layer into multiple domains, in which case the regions are often best analyzed separately.

The magnetization reversal behaviour is a manifestation of the well known process of magnetization reversal by domain wall nucleation and propagation mixed with coherent Stoner-Wohlfarth rotation.

The mechanism of coherent rotation is illustrated schematically in Fig. 2.1. The single domain energy according to Eq. 2.4 is plotted qualitatively on the y-axis as a function of the magnetization orientation  $\vartheta$ . We include the main biaxial and both small uniaxial

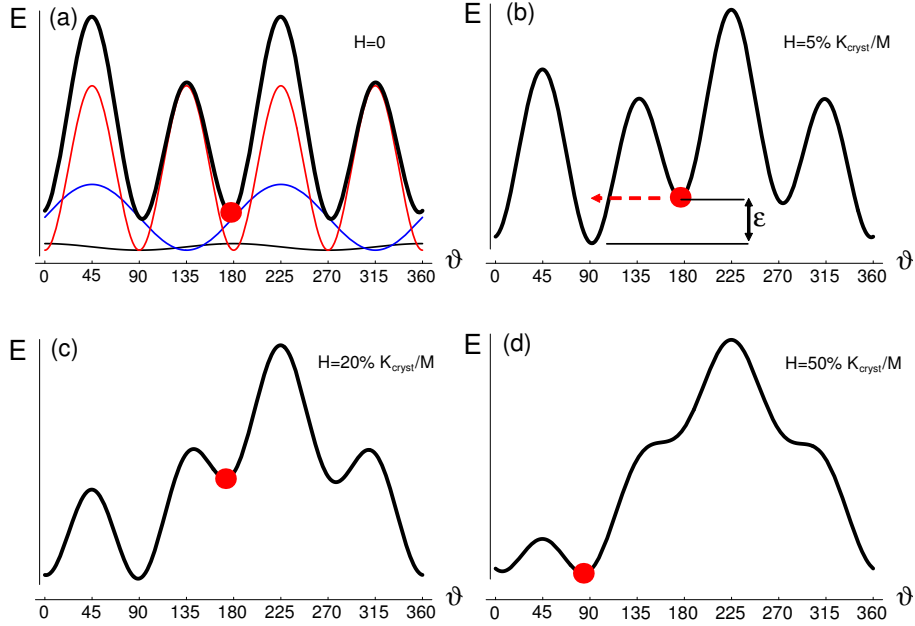


**Abb. 2.1:** Energy landscape at zero field (a). The symmetry components of the anisotropy are shown with thin lines (biaxial red; uniaxial along  $[\bar{1}10]$  blue; uniaxial along  $[010]$  black). The energy surface evolves with increasing field along  $45^\circ$  (b-d) causing magnetization reversal through domain wall nucleation and propagation (b) or through Stoner-Wohlfarth rotation (c and d).

anisotropy components (thin lines in Fig. 2.1a) with a typical ratio of  $K_{cryst} : K_{uni[\bar{1}10]} : K_{uni[010]} = 100 : 10 : 1$  (for details see section 3.1.1), which at zero field add up to the energy landscape (thick line) in Fig. 2.1a. Note that the two uniaxial components play very concrete roles in this picture. While  $K_{uni[\bar{1}10]}$  describes the difference in "height" of the maxima of the energy landscape,  $K_{uni[010]}$  is responsible for the different energy of the minima. In Fig. 2.1a we assume the remanent magnetization to be along  $180^\circ$  (red circle). Figure 2.1b shows the situation in a small external magnetic field along  $45^\circ$ , the magnetization remains in the local energy minimum at  $180^\circ$ . As the magnetic field is increased, the energy profile changes progressively as shown schematically in (c) and (d). Within the coherent rotation picture, the direction of the magnetization gradually follows the local minimum from  $180^\circ$  to  $90^\circ$ . Only when the field becomes sufficient to completely suppress the energy barrier between the various local minima, will the magnetization reach its final state parallel to the applied magnetic field along  $45^\circ$ .

In contrast, the reversal by domain wall (DW) nucleation/propagation is indicated by a red arrow in panel (b). By creating a new domain locally, and having it expand across the sample, the device can reorient its magnetization as soon as the energy gained in doing so becomes larger than the energy required to nucleate and propagate the domain wall. The energetics of domain wall nucleation and propagation are in principle very complex.

---

Experience, however, has shown that a simple model assuming a constant DW nucleation and propagation energy  $\varepsilon$  for a  $90^\circ$ -DW (and  $2\varepsilon$  for a  $180^\circ$ -DW), irrespective of the direction to and from which the magnetization is switching, describes accurately the experimental results for most materials including (Ga,Mn)As. This model will be discussed more in detail in Section 3.1.3. Note also that not only an external magnetic field but also current pulses between regions of different magnetization can initiate magnetization reversal and DW displacement [Yama 04, Goul 06]. This is the focus of chapter 4.



# Chapter 3

## Analyzing Magnetization Behaviour in Transport

The described magnetization behaviour, combined with the principally biaxial in-plane easy axis, can be observed in direct or indirect magnetization measurements, and leads to a very characteristic two-step reversal process in SQUID (superconducting quantum interference device) and magnetoresistance measurements. Three-jump magnetic switching is also possible in very specific situations[Cowb 97].

### 3.1 Biaxial Magnetic Anisotropy

Assume a biaxial magnetic anisotropy with easy axes along the in-plane  $\langle 100 \rangle$  crystal directions (coordinate axes in Fig. 3.1a) as a first approximation of the 4 K anisotropy of (Ga,Mn)As. Assume further that the longitudinal resistance of a Hall bar with its current along the  $[100]$  axis is measured while the external magnetic field is swept from a high negative to a high positive value along a direction  $30^\circ$  away from the  $[100]$  axis. Using eq. 2.4 and 2.2 we can now calculate the corresponding AMR signal shown in Fig. 3.1b(left y-axis scale). At high negative fields, the magnetization is forced along the field direction (not shown). (1) As the field is decreased  $\mathbf{M}$  gradually relaxes through Stoner-Wohlfarth rotation until it is aligned with its closest easy axis. At zero field  $\mathbf{M}$  is thus parallel to  $[\bar{1}00]$  and to the current, yielding the smallest resistance value  $R_{\parallel}$ . (2) At a small positive field  $H_{c1}$  a  $90^\circ$ -DW is nucleated and propagates through the structure resulting in an abrupt change of the magnetization direction to the  $[010]$  direction.  $\mathbf{M}$  is now perpendicular to the current, yielding the maximum resistance value  $R_{\perp}$ . (3) At the second switching field  $H_{c2}$ , another  $90^\circ$ -DW is nucleated and the magnetization jumps close to the  $[100]$  easy axis. (4) With increasing magnetic fields  $\mathbf{M}$  rotates again towards the magnetic field direction. The entire process is of course hysteretically symmetric (not shown).

If another Hall bar is oriented along the  $[110]$  crystal direction (blue in Fig. 3.1a) the easy axes  $[100]$  and  $[010]$  have an angle of  $\pm 45^\circ$  with the current path. An abrupt switch

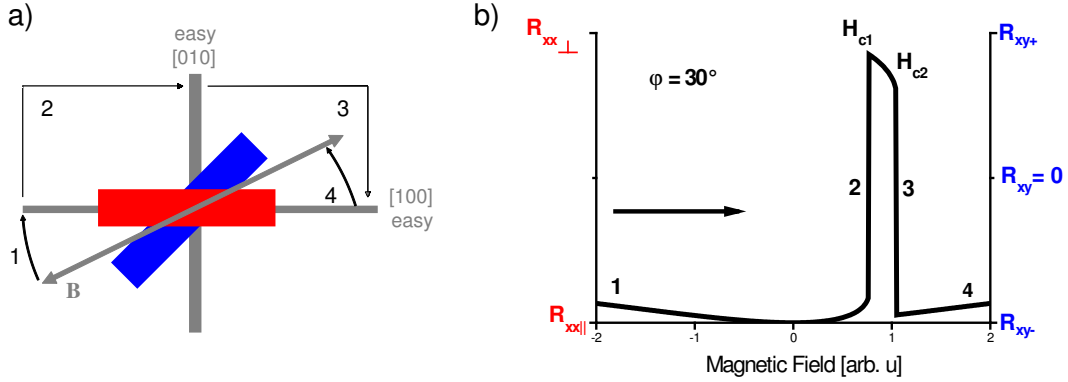


**Abb. 3.1:** Two-step magnetization reversal. a) Sketch showing the magnetization behaviour in hard (blue) and easy (red) axis Hall bars. b) The corresponding calculated AMR scan for the easy axis Hall bar (left scale), which is equivalent to a Planar Hall scan on the hard axis bar (right scale).

of magnetization from one easy axis to the other corresponds according to eq. 2.3 to a sharp switching event between two extrema of the transverse resistance. The calculated Planar Hall signal is thus up to a constant identical with the previously discussed curve in Fig. 3.1b, in this case centered around zero transverse resistance (blue/right y-axis). Because of this, transverse resistance measurements are the method of choice for Hall bars oriented along a crystalline hard axis. For Hall bars along an easy axis, longitudinal resistance measurements are the only useful technique. Indeed, if the current direction is rotated by  $45^\circ$ , Eq. 2.3 transforms into Eq. 2.2 (plus an uninteresting offset).

Fig. 3.2a shows AMR (middle) and Planar Hall effect (right) curves for field sweeps along different angles  $\varphi$  in the plane calculated using Eq. 2.4 in combination with Eq. 2.2 and 2.3 respectively. The domain wall nucleation energy  $\varepsilon$  was exaggerated in these calculations (30% of  $K_{cryst}$  instead of 5-10% as would be typical for (Ga,Mn)As) to illustrate both Stoner-Wohlfarth rotation and DW-related magnetization switching in the same figure. The middle panel of Fig. 3.2a, shows MR curves for a Hall bar along a biaxial easy axis. If the external magnetic field is swept along the [100] easy axis ( $0^\circ$ ), the magnetization is always parallel to the current direction. The resistance (black line) thus takes its lowest value  $R_{\parallel}$  throughout the whole field range. If the field is swept along the [010] easy axis ( $90^\circ$ ), the magnetization is always perpendicular to the current resulting in a high resistance value  $R_{\perp}$  throughout the whole curve (thin cyan). For intermediate magnetic field angles, the magnetization is parallel to the field at high positive and negative fields, yielding intermediate resistance values. At zero field the magnetization relaxes to the closest easy axis, which is [100] for the  $30^\circ$  scan and [010] for the  $60^\circ$  and  $45.1^\circ$  scans, corresponding to the lowest and highest resistance value respectively. The  $45.1^\circ$ -scan (green line) can be used to measure the strength of the magnetic anisotropy. We can read out the anisotropy field ( $-2K_{cryst}/M$ ), at the point where the magnetization starts to turn away from the magnetic field direction. A measurement with two possible

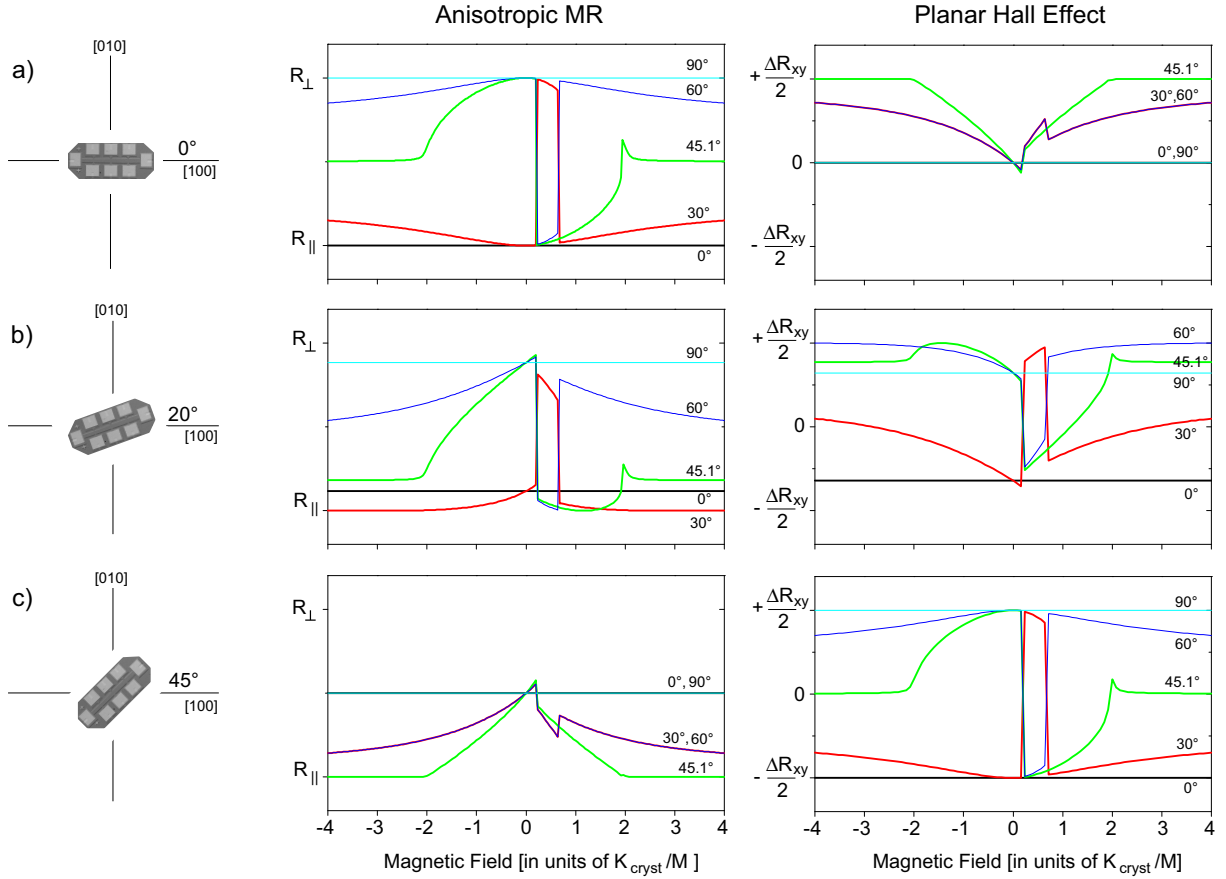


**Abb. 3.2:** Calculated Anisotropic Magnetoresistance (left) and Planar Hall effect (right) curves for magnetic field sweeps along several in-plane angles ( $\varphi = 0^\circ, 30^\circ, 45.1^\circ, 60^\circ$  and  $90^\circ$ ) for Hall bar orientations as indicated in the sketches on the left, with current along a)  $0^\circ$  b)  $20^\circ$  c)  $45^\circ$ . The underlying magnetic anisotropy is biaxial with easy axes along  $[100]$  and  $[010]$ . All angles with respect to the  $[100]$  crystal direction. The domain wall nucleation/propagation energy  $\varepsilon$  is exaggerated with 30% of  $K_{\text{cryst}}$ .

resistance states at zero field always suggests a biaxial magnetic anisotropy. However, note that these two states can correspond to the same resistance value as, e.g., if the easy axis and the current include an angle of  $45^\circ$  (left panel of Fig. 3.2c), where the  $0^\circ$  (black) and  $90^\circ$  (cyan) curve fall on top of each other. The panels on the right show the calculated Planar Hall resistance curves in the respective configurations. Note, that, the AMR signal in Fig. 3.2a is identical to the PHE signal in Fig. 3.2c, as discussed above. The easy axis showing constant resistance throughout the whole scan can easily be identified in any of the configurations, even if current and easy axis include an oblique angle as in Fig. 3.2b.

The switching fields ( $H_{c1}$  and  $H_{c2}$  in Fig. 3.1b) can be derived analytically from eq. 2.4 [Cowb 95] (here for a pure biaxial anisotropy;  $K_{\text{uni}[110]} = K_{\text{uni}[010]} = 0$ ). Typically DW nucleation and propagation dominates the magnetization reversal process, i.e.  $\varepsilon$  is much smaller than the crystalline anisotropy. That is why it can be assumed that the magneto-static energy minima remain to a good approximation along the biaxial easy axes during

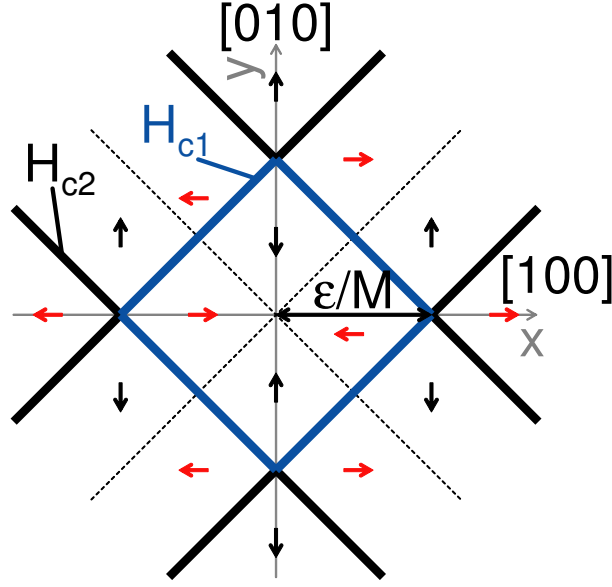


**Abb. 3.3:** *Switching field positions (thick solid lines) in a polar plot for a biaxial material with easy axes along [100] and [010](coordinate axes). The magnetization direction in each region of the plot is indicated by arrows (red/black: high/low resistance) and the hard axes by dashed lines.*

the double-step switching process. The energy difference between stable magnetization states is thus given by the respective difference in Zeeman energy (Eq. 2.4). When the energy gained through a  $90^\circ$  magnetization reorientation is larger than  $\varepsilon_{90^\circ}$ , the nucleation and propagation energy of a  $90^\circ$ -DW, a thermally activated switching event becomes possible. This, on the timescale of our measurement, results in an immediate switching event. For example, to calculate the field required for the magnetization to jump from  $0^\circ$  to  $90^\circ$ , the difference in the Zeeman terms is equated with  $\varepsilon$

$$\Delta E_{0^\circ \rightarrow 90^\circ} = -MH[\cos(0^\circ - \varphi) - \cos(90^\circ - \varphi)] = \varepsilon_{90^\circ} > 0. \quad (3.1)$$

Reorganizing gives the switching field  $H_c$  as a function of  $\varphi$ .

$$H_c = \frac{-\varepsilon_{90^\circ}}{M[\cos \varphi - \sin \varphi]} \quad (3.2)$$

This equation is the same for other pairs of angles, except for the signs in front of the sine and cosine functions in the denominator in the following marked with  $\pm$ . The switching field equation above describes straight lines if plotted in a polar coordinate system using  $H$  as radial and  $\varphi$  as angular coordinate. The polar plot in Fig. 3.3 shows the resulting characteristic square pattern[Cowb 95]. We express the switching field positions in this plot (thick lines) in cartesian coordinates using  $x = H_c \cos \varphi$  and  $y = H_c \sin \varphi$  to get a better feeling for the switching field behaviour and to extract important parameters.



$$\begin{aligned}
H_c \cdot M[\pm \cos \varphi \pm \sin \varphi] &= -\varepsilon_{90^\circ} \\
M[\pm x \pm y] &= -\varepsilon_{90^\circ} \\
y &= \pm x \pm \frac{\varepsilon_{90^\circ}}{M}
\end{aligned} \tag{3.3}$$

The characteristic polar-plot-pattern for a biaxial material is thus a square with diagonals along the easy axes (the coordinate axes in Fig. 3.3). The first switching field (thick blue lines) is largest along the easy axes, where  $H_{c1} = \varepsilon/M$ . The DW nucleation/propagation energy can be extracted from the diagonal of the square, whose length is equal to  $\frac{2\varepsilon_{90^\circ}}{M}$ . All switching field lines in Fig. 3.3 have an angle of  $45^\circ$  to the coordinate axes. The dashed lines represent the hard magnetic axes. Arrows illustrate the direction of the magnetization and their color the corresponding resistance state of the respective section in an AMR measurement with current along one of the easy axes.

Neglecting coherent rotation is typically a good model for the first switching fields  $H_{c1}$ , whereas  $H_{c2}$  is influenced by magnetization rotation especially close to the hard axes. Pairs of parallel lines in Fig. 3.3 do not extend to infinity, in practice they move closer to the hard axes (see for example the figures in section 3.1.4). The magnetic field needed to force the magnetization parallel to the external field in the hard axis direction is called the anisotropy field  $H_a$ . It is a measure of the anisotropy strength and can be calculated from Eq. 2.4 using the definition of the anisotropy field:  $H_a$  is the strength of a field along the hard axis (here  $45^\circ$ ) needed to suppress the local minima along the easy axes.

$$H_a = \frac{2K_{cryst}}{M} \tag{3.4}$$

### 3.1.1 The Anisotropy Fingerprint Technique

Traditionally the magnetic anisotropy of the materials discussed here has been investigated by direct measurement of the projection of the magnetization onto characteristic directions using SQUID or VSM. The advent of vector field magnets has recently opened up possibilities for acquiring a detailed mapping of the anisotropy. We present one such method here, which builds on the above discussed angular dependence of the magnetization switching fields. It is based on summarizing the results of transport measurements into color coded resistance polar plots (RPP) which act as fingerprints for the anisotropy of a given structure. Not only is this method faster than the traditional alternatives, but it is also more sensitive to certain secondary components of the anisotropy, in particular those with easy axes collinear to the primary biaxial anisotropy component[Cowb 95]. The technique thus often reveals the existence of components which would be missed using standard techniques. Moreover, the technique can be applied to study the anisotropy of layers by using macroscopic transport structures, or applied directly to device elements.

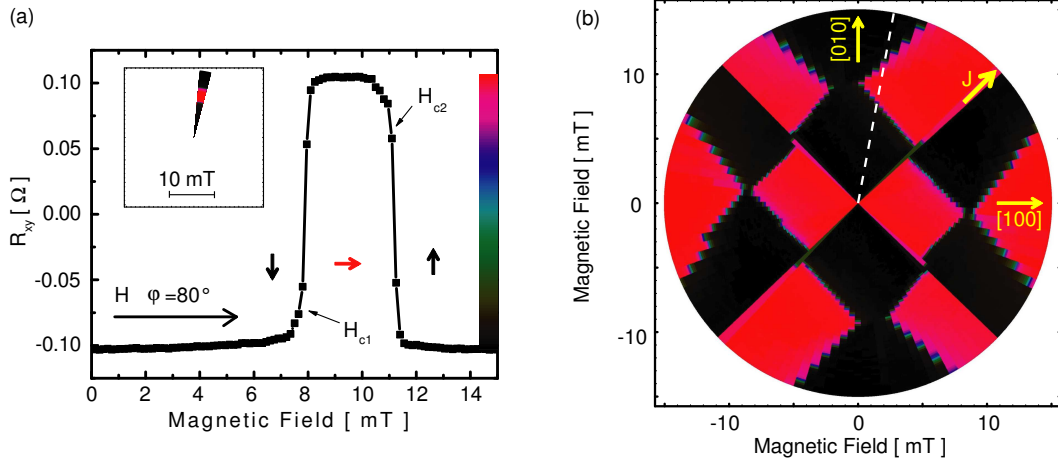


**Abb. 3.4:** *a) Planar Hall Effect measurement along  $\varphi = 80^\circ$  with marked first and second switching field, color scale and the corresponding section of a color coded resistance polar plot (inset). b) Resistance polar plot from a full set of Planar Hall measurements along every  $3^\circ$ . The  $80^\circ$ -section corresponding to (a) is marked by a dashed line.*

It can reveal effects of processing or the influence of small strain fields due to, for example, contacting.

We demonstrate the technique by applying it to the characterization of a typical 20 nm thick (Ga,Mn)As layer grown on a GaAs (001) substrate. It is patterned into a 60  $\mu\text{m}$  wide Hall bar oriented along the  $\langle 110 \rangle$  crystal direction by optical lithography and chlorine assisted dry etching. Contacts are established through metal evaporation and lift off. An angular set of IPH curves is acquired while sweeping the magnetic field along multiple directions in the sample plane. For each individual angle the magnetization state of the sample is first prepared by a strong negative magnetic field along  $\varphi$ . The field is then slowly brought down to zero while assuring that the field vector never deviates from the  $-\varphi$  direction. The IPH curve as a function of positive magnetic field in the  $\varphi$  direction is then acquired from zero to higher fields, and these results are displayed in a RPP as in Fig. 3.4b.

Fig. 3.4a shows a typical IPH measurement. After magnetizing the sample along  $80^\circ$  at  $-300$  mT, the magnetization relaxes towards the  $[0\bar{1}0]$  easy axis, as the field is brought back to zero. This corresponds to the negative resistance state associated with an angle of  $\vartheta = -135^\circ$  between  $\mathbf{J}$  and  $\mathbf{M}$ . The first abrupt resistance change at the field  $H_{c1}$  corresponds to a  $90^\circ$  reorientation of  $\mathbf{M}$  towards the other (Ga,Mn)As easy axis  $\sim [100]$ . A second reorientation of  $\mathbf{M}$  towards  $[010]$  at  $H_{c2}$  completes the double-step magnetization switching. A set of such magnetic field scans along many angles, here every  $3^\circ$ , is compiled into a RPP with the magnetic field  $H$  along the radius and each scan at its angle  $\varphi$  (Half the plot was measured with high resolution and numerically mirrored after confirming hysteretic symmetry by a lower resolution scan). The inset of Fig. 3.4a shows the  $80^\circ$ -segment marked by a dotted white line in the full RPP of Fig. 3.4b. The intensity encodes the normalized resistance value, where low (black) and

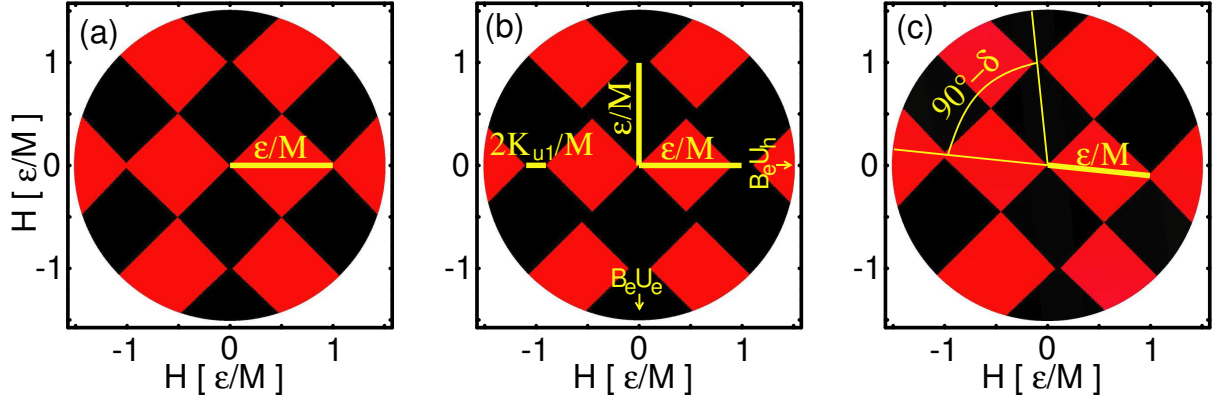


**Abb. 3.5:** Calculated resistance polar plots for a biaxial material with easy axes along the  $[100](0^\circ)$  and  $[010](90^\circ)$  crystal directions(a) and the same material with an additional uniaxial anisotropy along  $[010](b)$  or  $[1\bar{1}0](c)$ . Color scale of the resistance as in Fig. 3.4.  $\varepsilon$  denotes the  $90^\circ$ -DW nucleation/propagation energy.

high(red) denote the minimum and maximum resistance of the entire curve set. The positions of the switching fields in the polar plot and the symmetry of the pattern they form contain information on the underlying magnetic anisotropy.

We can now compare the observed switching field pattern in Fig. 3.4b with the calculated shape in Fig. 3.3. While a cursory examination suggests a similar  $H_{c1}$ -pattern, a more detailed comparison reveals significant differences: Focussing on the innermost switching event, the pattern is indeed strongly square-like, confirming that the (Ga,Mn)As has a mainly biaxial magnetic anisotropy at 4 K. The diagonals of this square-like  $H_{c1}$ -pattern are close to the  $[100]$  and the  $[010]$  crystal direction, the easy axes of the biaxial anisotropy term. However, the inner region is elongated (a rectangle and not a square) - the signature of an additional uniaxial anisotropy term with an easy axis bisecting the biaxial easy axes (Fig. 3.5c), as will be discussed in section 3.1.3. Additionally we observe a discontinuity in the middle of the rectangle sides and dark "open" corners close to the  $[010]$  direction. This is characteristic of a uniaxial magnetic anisotropy term collinear with one of the biaxial easy axes (Fig. 3.5b) and will be discussed in detail in section 3.1.2.

These qualitative changes in the behaviour of  $H_{c1}$  are a key signatures of the different anisotropy terms of the (Ga,Mn)As layer. A set of high resolution transport measurements compiled into a color coded resistance polar plot thus constitutes a fingerprint of the symmetry components of the anisotropy. It allows for the qualitative and quantitative determination of the different anisotropy terms. It can prove their existence and visualize their respective effects on the magnetization reversal.

### 3.1.2 Signature of a $\langle 010 \rangle$ Uniaxial Term

The fingerprint of a magnetically biaxial material in Fig. 3.5a is equivalent to the switching field pattern in Fig. 3.3. An additional small uniaxial anisotropy  $K_{uni[010]}$  along one of the

biaxial easy axes (here along  $90^\circ$ ) alters the square pattern as shown in Fig. 3.5b. The symmetry between the two biaxial easy axes is lifted, since one of them is parallel (biaxial easy, uniaxial easy;  $B_e U_e$ ) and one perpendicular (biaxial easy, uniaxial hard;  $B_e U_h$ ) to the easy axis of the uniaxial component. The angle dependent switching field can be derived as discussed in section 3.1 following [Cowb 95]: Again it is assumed, that the minima of the energy surface remain at their zero field angles throughout the switching process. In the present case however, the energy minimum along the  $[010]$  direction is favored. Its energy is  $\Delta E = K_{uni[010]}$  smaller compared with the  $[100]$  direction, which results in

$$\begin{aligned} H_c &= \pm \frac{\varepsilon_{90^\circ} \pm K_{uni[010]}}{M[\cos \varphi \pm \sin \varphi]} \\ y &= \pm x \pm \frac{\varepsilon_{90^\circ}}{M} \pm \frac{K_{uni[010]}}{M} \end{aligned} \quad (3.5)$$

$90^\circ$ -switches away from the  $B_e U_e$  axis occur now at higher magnetic fields compared to the pure biaxial anisotropy; switches towards  $B_e U_e$  at lower fields. The signs in eq. 3.5 are chosen appropriately. As a result typical steps in the  $H_{c1}$ - pattern emerge (Fig. 3.5b, e.g. along  $45^\circ$ ).

The strength of the uniaxial anisotropy can be determined from the separation  $\frac{2K_{u1}}{M}$  between  $H_{c1}$  and  $H_{c2}$  along the  $B_e U_h$  axis. A characteristic feature is the "open corner" of the  $H_{c1}$ - pattern along the  $B_e U_e$  axis. A  $180^\circ$  magnetization reversal becomes energetically more favorable in this angular region, than two successive  $90^\circ$  events. (Because of the underlying biaxial anisotropy, a  $180^\circ$ -DW can be seen as two loosely coupled  $90^\circ$ -DW, thus  $\varepsilon_{180^\circ} \sim 2\varepsilon_{90^\circ}$  [Cowb 95].) Since the isotropic magnetoresistance of typical samples is relatively small compared to the AMR, two magnetization directions differing by  $180^\circ$  are not distinguishable on the scale considered here, and have nearly the same color in the RPP, creating the characteristic "open corner".

### 3.1.3 Signature of a $\langle \bar{1}10 \rangle$ Uniaxial Term

In this section we describe the effects of a uniaxial anisotropy term  $K_{uni[\bar{1}10]}$  with its easy axis (along  $135^\circ$ ) bisecting the biaxial easy axes. This uniaxial anisotropy component flattens the energy surface (eq. 2.4) and shifts the positions of the energy minima by (see Fig. 3.6a)

$$\frac{\delta}{2} = \frac{1}{2} \arcsin\left(\frac{K_{uni[\bar{1}10]}}{K_{cryst}}\right) \quad (3.6)$$

towards the uniaxial easy axis[Dabo 94b]. All four minima have the same energy value. To derive the switching fields we equate the DW nucleation/propagation energy  $\varepsilon$  with the difference in Zeeman energy between the initial and final magnetization angle in the

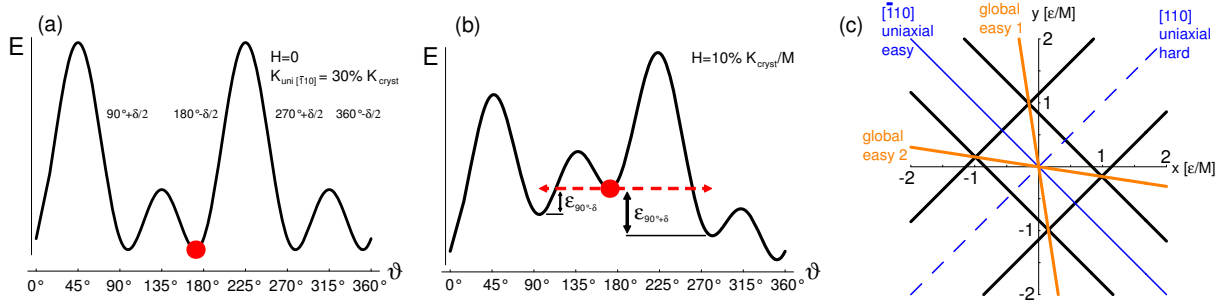


**Abb. 3.6:** *a) A uniaxial  $[\bar{1}10]$  anisotropy component flattens the energy surface (eq. 2.4) and shifts the positions of the energy minima. b) Energy landscape with magnetic field applied along the  $-\delta/2$ -global easy axis direction. A clockwise and counterclockwise jump of the magnetization (with the respective  $\varepsilon$ ) are equally possible. c) Switching field positions in the polar plot (thick black lines), global easy axes (orange) and easy and hard direction of the  $[\bar{1}10]$  anisotropy component (blue).*

respective switching event. As illustrated in Fig. 3.6a, the magnetization direction can change by  $90^\circ + \delta$  or  $90^\circ - \delta$  depending on whether the magnetization rotates clockwise or counterclockwise. We thus assume different DW nucleation/propagation energies [Tang 03]  $\varepsilon_{90^\circ+\delta}$  and  $\varepsilon_{90^\circ-\delta}$  respectively. The switching field positions in the polar plot given in cartesian coordinates are

$$\begin{aligned}
 y_{90^\circ+\delta} &= x \pm \frac{\varepsilon_{90^\circ+\delta}}{M\sqrt{2}[\cos(45^\circ-\delta/2)]} \\
 y_{90^\circ-\delta} &= -x \pm \frac{\varepsilon_{90^\circ-\delta}}{M\sqrt{2}[\cos(45^\circ+\delta/2)]}
 \end{aligned}
 \tag{3.7}$$

Equation 3.7 describes two parallel sets of lines, as shown in Fig. 3.6c, whose distance from the origin is determined by the respective  $\varepsilon$ . MOKE experiments on epitaxial iron films grown on GaAs (with similar anisotropy terms as (Ga,Mn)As) show that the sense of the magnetization rotation changes when crossing a global easy axis [Dabo 94a]. The two line sets of eq. 3.7 represent the clockwise and counterclockwise sense of magnetization rotation. If the field is applied along a global easy axes (minima of Fig. 3.6a) both rotation directions are energetically equivalent. Consequently the line set have to cross along global easy axes directions. Fig. 3.6b shows the energy landscape of Fig. 3.6a when a magnetic field is applied along the  $-\delta/2$ -global easy axis direction. For both rotation directions, the Zeeman term at the first switching field  $H_{c1}$  is equal to the respective  $\varepsilon$ . We can thus calculate the dependence of  $\varepsilon$  on the angle  $\Delta\theta$  between initial and final magnetization direction:

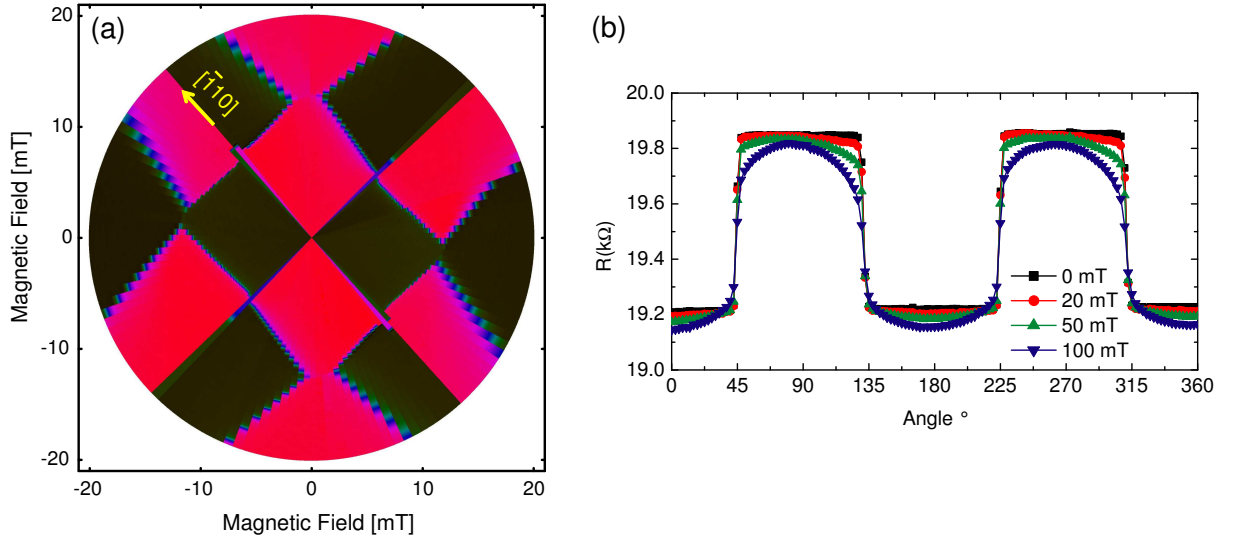


**Abb. 3.7:** *a) Fingerprint of a typical 20 nm thick (Ga,Mn)As Hall bar and b) angle-dependent longitudinal resistance at different fields after magnetizing along  $\varphi$ .*

$$\varepsilon_{90^\circ \pm \delta} = H_{c1} M (1 - \cos(90^\circ \pm \delta)) \quad (3.8)$$

$$\varepsilon_{\Delta\vartheta} = \varepsilon_{90^\circ} (1 - \cos(\Delta\vartheta))$$

which is intuitively reasonable. At the same time we find, that  $H_{c1}$  along a global easy axis is  $\varepsilon_{90^\circ}/M$ . The alternative assumption of a constant  $\varepsilon$  independent of the DW angle  $\Delta\vartheta$ , would lead to the inconsistent conclusion, that the rectangle in the polar plot would have its long axis perpendicular to the uniaxial easy direction.

A summary of the above is shown in Fig. 3.5c. The characteristic pattern of a mainly biaxial anisotropy with a bisecting uniaxial anisotropy component is rectangular. The diagonals of the rectangle are the "global easy axes", their length is  $2\varepsilon_{90^\circ}/M$ . The angle between the global easy axes gives the relative strength of the two anisotropy components (using eq. 3.6). The easy axis of the uniaxial term is along the median line of the longer edge.

The presence and sign of the  $\langle \bar{1}10 \rangle$  anisotropy term can be verified with the help of AMR or IPH measurements at magnetic fields of medium amplitude. For comparison, longitudinal resistance measurements on a Hall bar sample oriented along a (Ga,Mn)As easy axis ( $0^\circ$ ) are converted into the RPP displayed in Fig. 3.7a. This fingerprint shows an overall biaxial anisotropy with easy axes close to  $0^\circ$  and  $90^\circ$ . The central pattern is elongated along  $135^\circ$ , suggesting that a uniaxial anisotropy component with easy axis along this direction (the  $[\bar{1}10]$  crystal direction) is present.

This is confirmed by the measurements in Fig. 3.7b. Here the Hall bar sample is first magnetized in a high magnetic field of 300 mT along an angle  $\varphi$ . The longitudinal resistance is then measured, while the field is slowly stepped down to zero. Fig. 3.7b

shows the resistance values at 100 mT, 50 mT, 20 mT and 0 mT as a function of the field angle. For the interpretation of these curves, imagine for example an energy landscape as shown in Fig. 3.6, where the strength of the  $[\bar{1}10]$  uniaxial anisotropy term is exaggerated. This term describes the width and the height of the "hills" in the energy surface. The "hill" in the uniaxial easy axis direction (here  $135^\circ$ ) is lower than the energy barrier perpendicular to this direction, which is steeper and coincides with the hard magnetic axis of the  $[\bar{1}10]$  uniaxial term. At zero field the magnetization is aligned with one of the biaxial easy axes (black curve in Fig. 3.7). The steps in this curve mark the peak positions of the "hills" in the energy landscape - the biaxial hard axes. At medium fields (e.g. 50 mT in Fig. 3.6b), the magnetization is rotated away from the global easy axes, causing deviations from the step-like behaviour at zero field. These deviations occur at smaller field values along the uniaxial easy direction  $[\bar{1}10]$  compared with the uniaxial hard axis  $[110]$ . The direction (meaning the sign of  $K_{uni[\bar{1}10]}$ ) of the  $[\bar{1}10]$  uniaxial anisotropy is thus the same as in Fig. 3.7a: the abrupt resistance change at  $45^\circ$  marks the hard and the smoother behaviour at  $135^\circ$  the easy axis direction.

### 3.1.4 (Ga,Mn)As at 4 K - A Fingerprint Gallery

The typical anisotropy of (Ga,Mn)As at 4 K has long been debated. In addition to the main biaxial anisotropy term, most groups reported the observation of a  $\langle\bar{1}10\rangle$  uniaxial anisotropy component [Tang 03]. Others reported the presence of a much smaller  $[010]$  anisotropy term [Goul 04] which was too small to be verified in standard SQUID measurements. Here we described a method which is sensitive enough to detect both uniaxial anisotropy terms. We apply it to typical (Ga,Mn)As layers from different laboratories and find that all three anisotropy components, the biaxial and the two uniaxial ones, are present in every sample.

In the following we continue with the quantitative characterization of the typical (Ga,Mn)As sample of Fig. 3.4 and show polar plots of other (Ga,Mn)As samples at 4 K. As previously established, the RPP in Fig. 3.4b shows an  $H_{c1}$ -pattern with both an elongation in  $[\bar{1}10]$ -direction and steps along the hard axes. Both uniaxial anisotropy components are clearly present. From the length of the diagonals we estimate  $\frac{\varepsilon}{M} \sim 8$  mT. The step height gives  $\frac{K_{uni[010]}}{M} \sim 1$  mT. From the rectangle side-ratio we obtain  $\delta \sim 8^\circ$ .  $K_{uni[\bar{1}10]}$  is thus  $\sim 15\%$  of  $K_{cryst}$ .  $\frac{K_{cryst}}{M} \sim 100$  mT can be estimated from the asymptotic behavior of the magnetization towards the hard axes at higher fields (using eq. 3.4) and  $M \sim 37,000$  A/m is known from SQUID measurements.

We applied the method to many typical MBE layers from Würzburg and other laboratories to confirm that the biaxial and *both* the  $[\bar{1}10]$  and the  $[010]$  uniaxial anisotropy term are present in all typical compressively strained (Ga,Mn)As layers at 4 K. We found that, as a rule of thumb, the typical relative strength of the anisotropy terms is of the order of  $K_{cryst} : K_{uni[\bar{1}10]} : K_{uni[010]} \sim 100 : 10 : 1$ .

The anisotropy components and  $\varepsilon$  can of course differ from wafer to wafer. Neglecting

coherent rotation is typically a good model for the first switching fields  $H_{c1}$ , whereas  $H_{c2}$  is influenced by magnetization rotation especially along the hard axes, as mentioned above. See for example Fig. 3.8, where AMR curves along every  $10^\circ$  were taken on a Hall bar along  $0^\circ$ . The central region shows a rectangular pattern (signature of the  $[\bar{1}10]$  uniaxial term) with open corners and steps along the hard axes (signature of the  $[010]$  uniaxial term). There is almost no coherent rotation at these low fields. Magnetization reorientations occur through DW nucleation and propagation as seen from the abrupt color changes (between red and blue). The second switching fields along the hard axes (e.g. along  $45^\circ$  at 50 mT) are marked by smooth color transitions proving that coherent rotation is at play. Smooth color transitions at even higher fields (green to black around  $0^\circ$  and red to green around  $90^\circ$ ) finally are caused by the isotropic MR effect.

Figures 3.9a and c show similar AMR fingerprints on two Hall bars made from the same wafer, but oriented along orthogonal crystal directions. Panels c and d show a close up of the central region. Both fingerprints show exactly the same switching pattern with inverted colors because of the orthogonal current directions. Again all three anisotropy components are present. The  $[\bar{1}10]$  uniaxial term with easy axis along the long axis of the rectangle ( $135^\circ$ ) and the  $[010]$  uniaxial component with easy axis along  $90^\circ$  where the open corners are clearly visible.

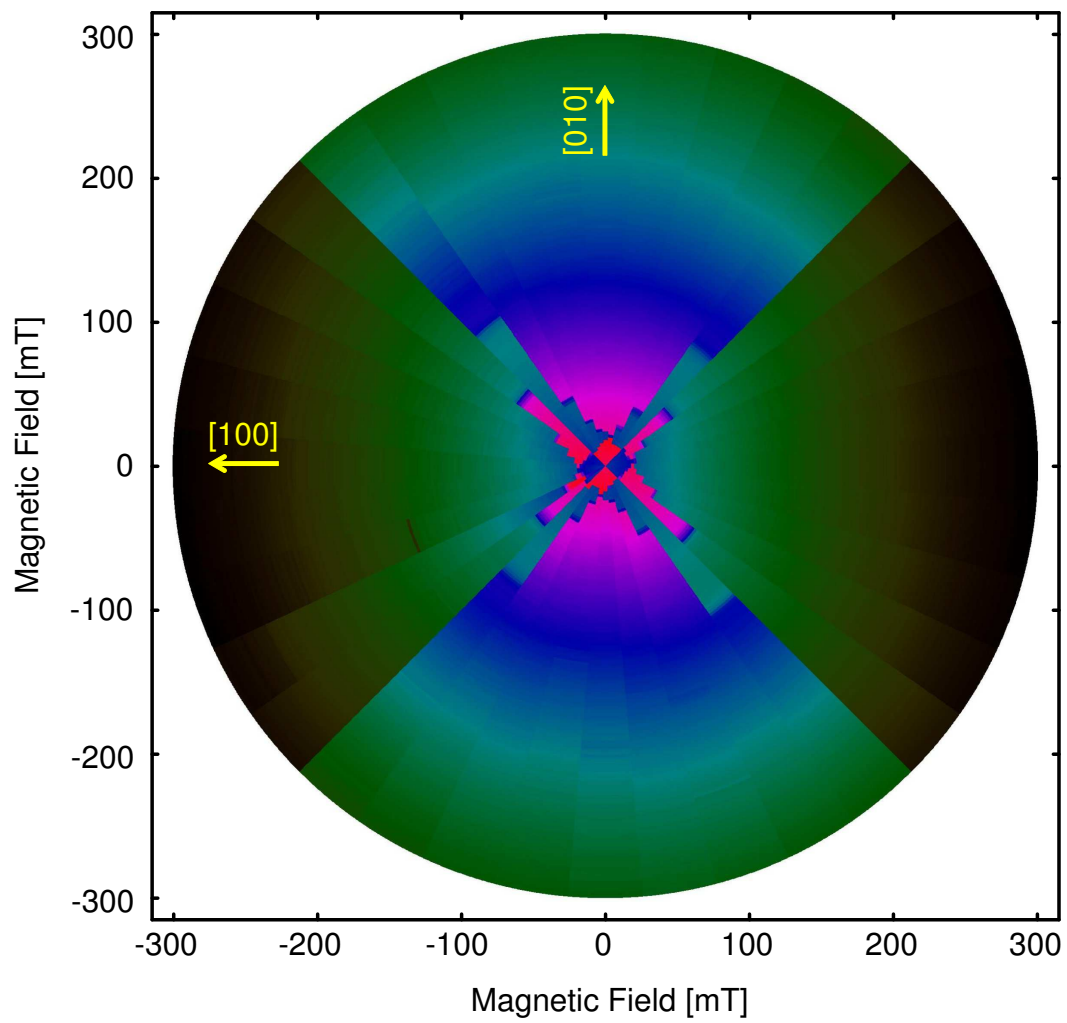
Figure 3.10a shows a fingerprint of a 70 nm thick (Ga,Mn)As layer where the high resolution central RPP shows a strong  $[010]$  uniaxial term; here with the easy axis along the  $[100]$  crystal direction. The pattern has almost no elongation, i.e. the  $[\bar{1}10]$  term is smaller than usual.

Fig. 3.11a shows an AMR fingerprint of a 25 nm thick (Ga,Mn)As layer grown at Nottingham University [Edmo 06]. The layer behaves similarly to the ones discussed above, both qualitatively and quantitatively. The open corner along  $0^\circ$  marks the  $[100]$  uniaxial easy axis. The anisotropy constant of this component is  $K_{uni[010]}/M \sim -0.5$  mT. The  $90^\circ$ -DW nucleation/propagation energy is  $\varepsilon/M \sim 7$  mT. The relatively small elongation along the  $[\bar{1}10]$  crystal direction yields  $K_{uni[\bar{1}10]}/K_{cyst} \sim 7\%$ .

Figure 3.11b shows a similar fingerprint of a 47 nm thick (Ga,Mn)As layer grown at imec in Leuven, Belgium [vanR 06]. This fingerprint also has pronounced open corners along  $0^\circ$  and steps along the hard axes yielding  $K_{uni[010]}/M \sim -1.5$  mT. The diagonal extent of the  $H_{c1}$ -pattern gives  $\varepsilon \sim 8$  mT. And the elongation is the signature of the  $[\bar{1}10]$  uniaxial component with  $K_{uni[\bar{1}10]}/K_{cyst} \sim 10\%$ .

In summary we have shown that RPP compiled from high resolution AMR and IPH measurements constitute a fingerprint of the (Ga,Mn)As anisotropy. They allow both qualitative and quantitative statements about the symmetry components of the magnetic anisotropy and the DW nucleation/propagation energy. The same technique is equally applicable to any transport phenomena which produces a response to the orientation of the magnetization, such as AMR, or Tunneling Anisotropic Magnetoresistance (TAMR) (which will be discussed in Ch. 5). It allowed us to identify the simultaneous presence





**Abb. 3.8:** Typical AMR fingerprint measurement of a 100 nm thick  $(\text{Ga},\text{Mn})\text{As}$  Hall bar. The current direction is along  $0^\circ$ .

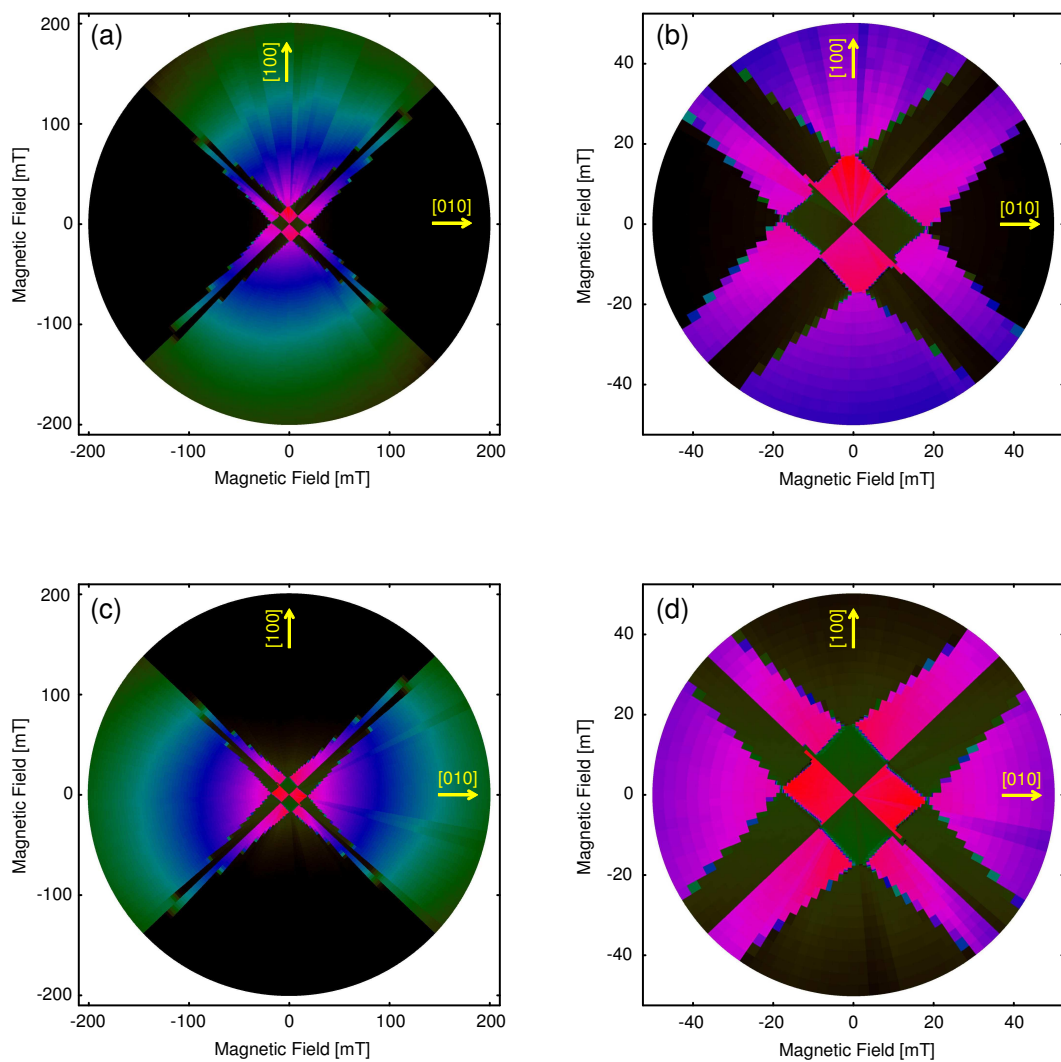


**Abb. 3.9:** High angular resolution fingerprint measurements (a,b) and close ups of the central region (c,d) for two Hall bars made of the same 70 nm thick material but oriented along orthogonal crystal directions. The current flows along  $0^\circ$  in a and b and along  $90^\circ$  in c and d.

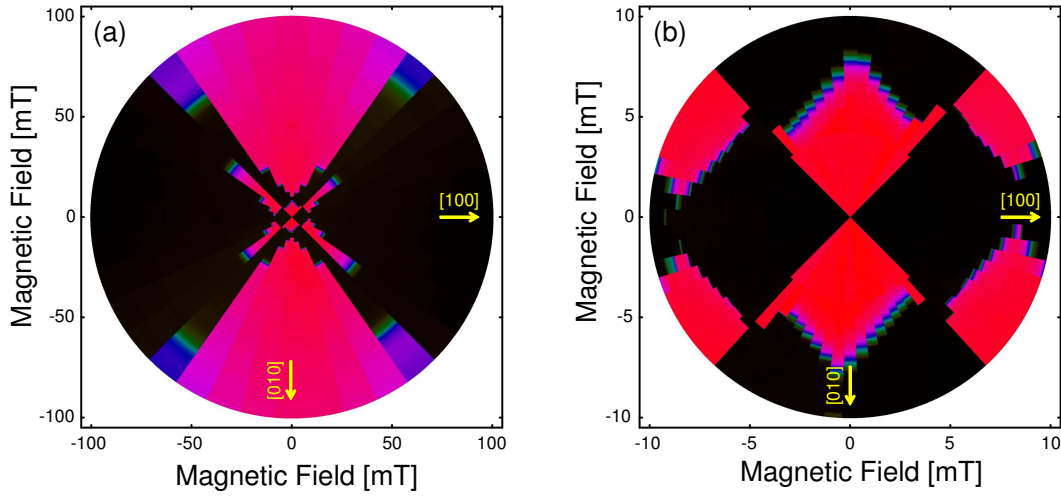


**Abb. 3.10:** Fingerprint measurement and high resolution RPP at low magnetic field for a 70 nm thick (Ga,Mn)As layer with strongly visible  $[010]$  uniaxial anisotropy component but a relatively small  $[\bar{1}10]$  term.

of the biaxial and two uniaxial anisotropy components with a typical  $K_{cyst} : K_{uni[\bar{1}10]} : K_{uni[010]}$  ratio of  $\sim 100 : 10 : 1$  in as grown (Ga,Mn)As at 4 K. Indeed all (Ga,Mn)As layers investigated show both these uniaxial components, including layers where the  $[010]$  component could not be identified in SQUID measurements. Moreover the application of our fingerprint method to previously published data in the literature shows that in all cases where sufficient data is available to make a determination, both uniaxial components are present.

## 3.2 Uniaxial Magnetic Anisotropy

This section deals with the magnetization behaviour of magnetically uniaxial materials and how it manifests itself in transport measurements. The latter with two specific applications in mind:

- The (Ga,Mn)As magnetic anisotropy is strongly temperature dependent with the  $\langle 110 \rangle$  uniaxial anisotropy term being dominant close to the Curie temperature (section 3.3).
- Submicron patterning of (Ga,Mn)As and the corresponding anisotropic strain relaxation can be used to create magnetically uniaxial structures. This is the focus of chapter 6.

Assume a magnetically uniaxial particle that displays uniform magnetization and whose magnetization is confined to the layer plane, such as a very small elongated structure patterned from a compressively strained (Ga,Mn)As layer. How does the magnetization react to in-plane magnetic fields in different directions? We again track the

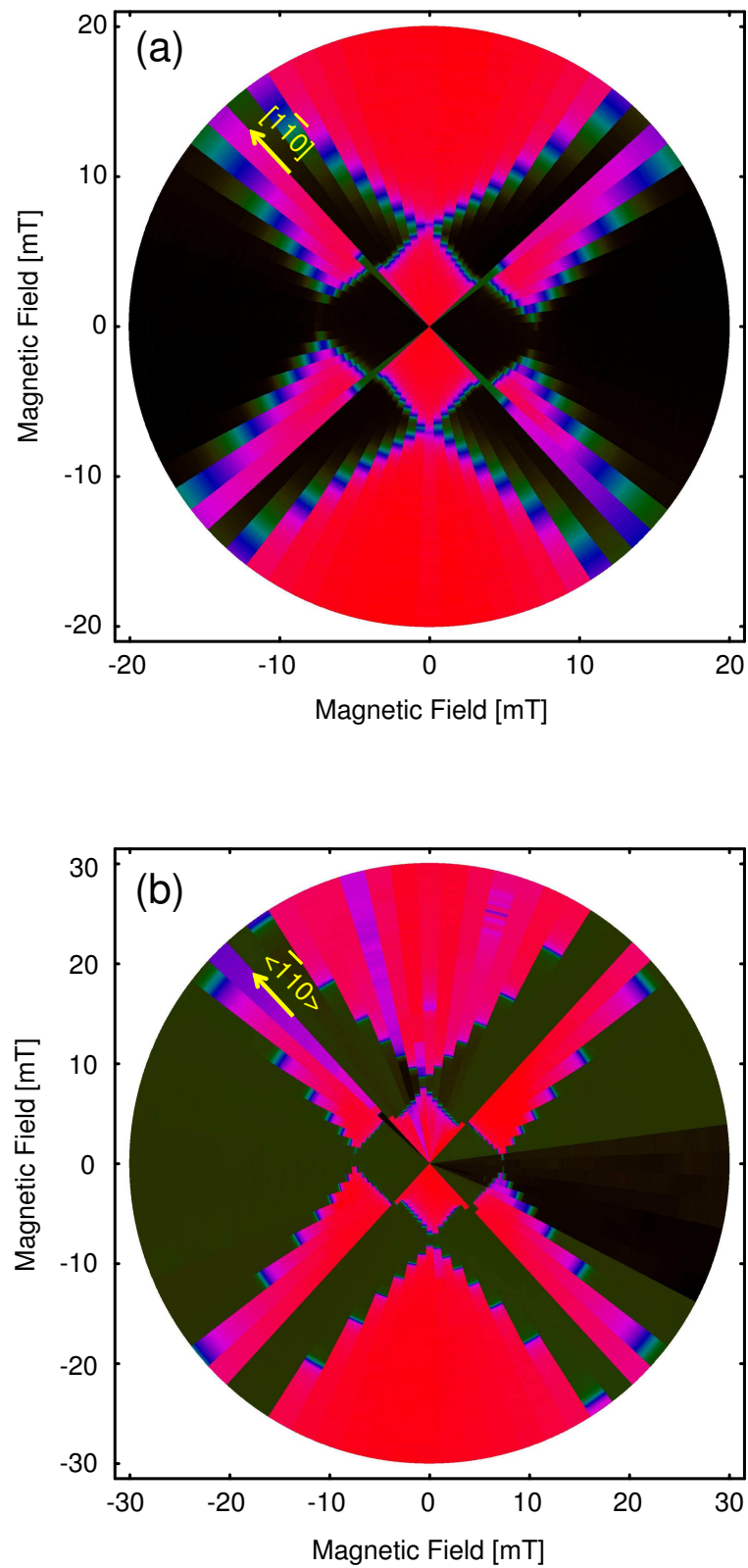


**Abb. 3.11:** Anisotropy fingerprint measurements of two  $(Ga,Mn)As$  layers grown by a) the group at Nottingham university [Edmo 06] and at IMEC in Leuven, Belgium [vanR 06].

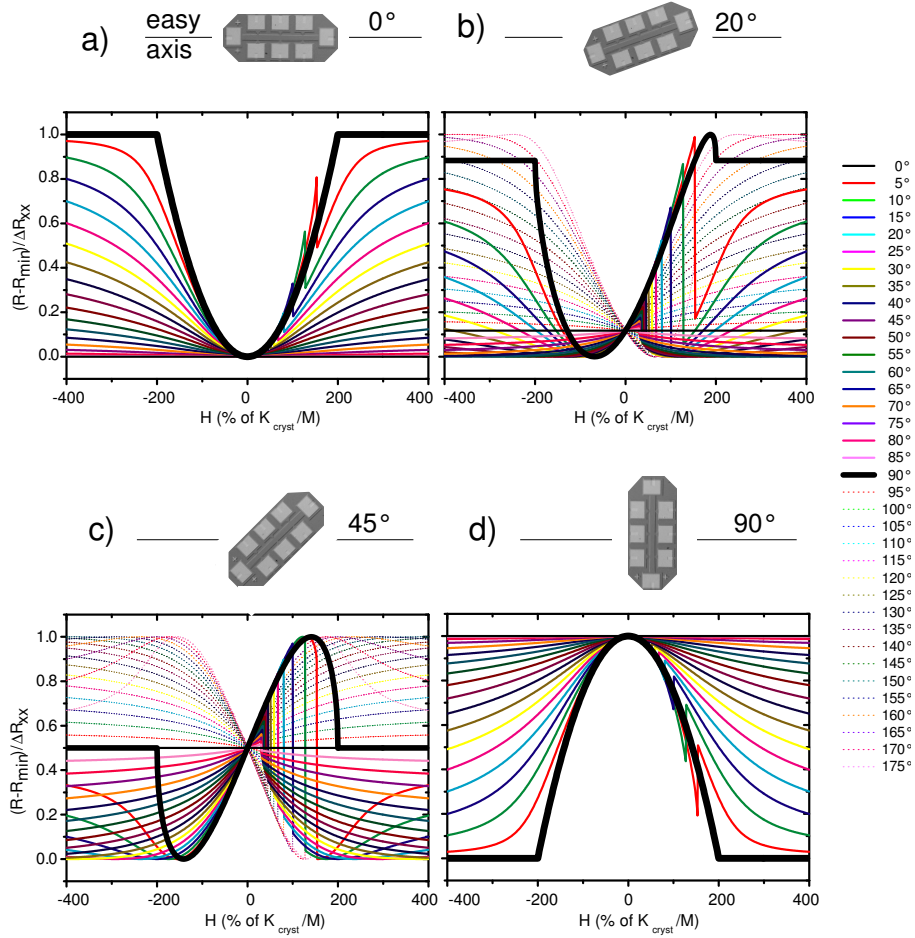


**Abb. 3.12:** Calculated anisotropic magnetoresistance curves in a magnetically uniaxial material for magnetic field sweeps along many in-plane directions ( $0^\circ..85^\circ$  thin solid,  $90^\circ$  thick,  $95^\circ..175^\circ$  dashed) for Hall bar orientations as in the sketches with current along (a)  $0^\circ$ , (b)  $20^\circ$ , (c)  $45^\circ$ , and (d)  $90^\circ$ . All angles with respect to the uniaxial easy axis. The field is swept from left to right.

magnetization angle using AMR measurements and finally discuss the color-coded RPP, the anisotropy fingerprint, expected for a material with uniaxial magnetic anisotropy.

Fig. 3.12 shows AMR curves calculated for a magnetically uniaxial material using Eq. 2.4 with  $\varepsilon = 30\% K_{uni}$ . The individual panels illustrate how the current direction with respect to the easy axis modifies the overall picture of a set of AMR curves. In all four panels a single zero field resistance state can be identified, corresponding to the easy axis magnetization orientation. The resistance value is given by the angle between current and easy axis through Eq. 2.2. If the external field is swept along this easy axis direction ( $0^\circ$ , thin black line), the magnetization is aligned with the easy axis throughout the whole scan, yielding a horizontal line through the focal point at zero field. The hard axis scan (thick line) reveals the anisotropy field; (the same as in the biaxial case, Eq. 3.4)

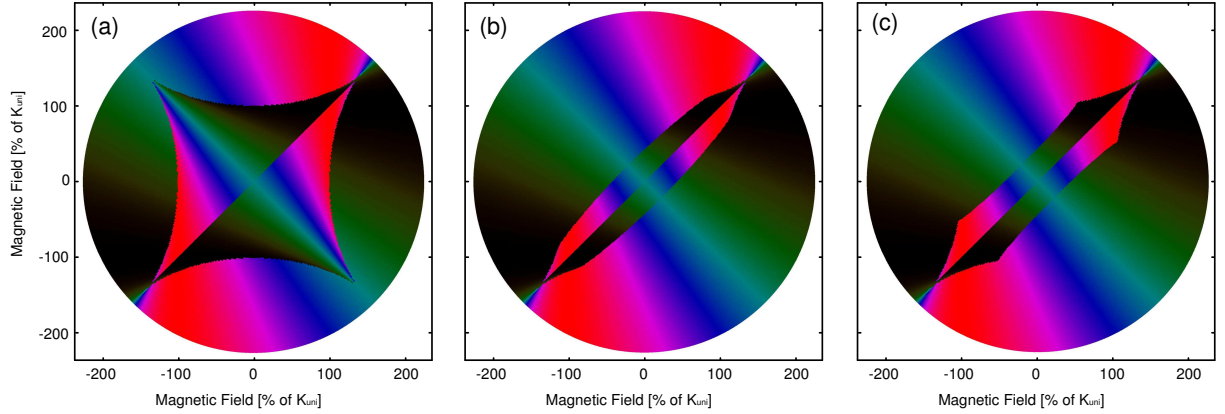


**Abb. 3.13:** *Calculated AMR fingerprints of a magnetically uniaxial material with easy axis along  $135^\circ$  and current along  $0^\circ$ . Magnetization reversal through (a) coherent rotation only (Stoner-asteroid) and (b) DW nucleation and propagation with  $\varepsilon$  according to Eq. 3.8 (c) simplified model assuming a constant  $\varepsilon = 2\varepsilon_{90^\circ}$ . ( $\varepsilon_{90^\circ} = 30\% K_{uni}$ )*

$$H_a = \frac{2K_{uni}}{M} \quad (3.9)$$

the external magnetic field perpendicular to the easy axis, where the magnetization starts to deviate from the field direction. The magnetization rotation in panels (a) and (d) yields parabolic dependence of the resistance on the field amplitude [West 60]. In all other MR scans the magnetization relaxes to the closest easy axis direction while the field is decreased from high negative values, reaching the focal point at zero field. After zero, the magnetization direction reverses by circa  $180^\circ$  through DW nucleation and propagation, which is visible as abrupt resistance changes in Fig. 3.12, for example the spikes around  $100\% K_{uni}$  in panel (a). A back sweep results in a hysteretically symmetric curve with the switching events at negative fields (not shown).

Fig. 3.13 shows the results of similar calculations with high angular resolution plotted in RPP fashion. Here the easy axis is oriented along  $135^\circ$  and the current flow along  $0^\circ$ . The colors are a function of the the current direction, for example dark color at high magnetic fields along the current, while the switching event pattern is defined by the magnetic properties alone.

If a structure is smaller than the single-domain limit [Brow 68, Ahar 88] it is energetically unfavourable to nucleate a DW. Instead the magnetization rotates coherently (Stoner-Wohlfarth model [Ston 48]). Fig. 3.13a shows the well known Stoner-Wohlfarth asteroid [Ston 48, Hube 00] which describes the switching positions of a uniaxial particle under coherent rotation. Its extend in both the easy and the hard axis direction is given by the anisotropy field.

Allowing for DW nucleation with  $\varepsilon$  according to eq. 3.8 truncates the easy axis corners of the asteroid as shown in Fig. 3.13b. The extent  $\varepsilon_{90^\circ}/M$  in the easy axis direction is

a measure for the DW nucleation/propagation energy. A field sweep along the hard magnetic axis, is still fully described by Stoner-Wohlfarth rotation and the extent in this direction is given by the anisotropy field. The detailed shape of the switching field pattern depends on the model used for the  $\varepsilon$ -dependence on the DW angle. Fig. 3.13c shows the RPP calculated assuming a constant  $\varepsilon_{\Delta\vartheta} = 2\varepsilon_{90^\circ}$  independent of the magnetization directions of the domains separated by the DW. While the easy and hard axis extent are the same as in Fig. 3.13b, the difference in shape allows the verification of one or the other model by experiment. As we will see later, experimental data are more suggestive of b than c.

### 3.3 Temperature Dependence of the (Ga,Mn)As Anisotropy

The fingerprint method provides us with the opportunity to investigate the temperature dependence of the magnetic anisotropy. Figures 3.14 and 3.15 show AMR fingerprints at various temperatures for the layer investigated in Fig. 3.9 at 4.2 K. The left column shows results on a Hall bar patterned along  $90^\circ$  (the  $[100]$  crystal direction). In the right column the Hall bar is oriented along  $0^\circ$ . The layer is, as typical, very homogeneous and the switching patterns in the two columns are virtually identical at all temperatures (except for a trivial inversion of the color scales).

The mainly biaxial anisotropy is the origin of the nearly four-fold symmetry in the low temperature fingerprints. The uniaxial anisotropy term with easy axis along the  $[\bar{1}10]$  crystal direction takes over with increasing temperature and becomes the dominant term close to  $T_C$ : already the fingerprints at 30 K exhibit the typical 2-fold symmetry of a uniaxial anisotropy. The short axis of the pattern marks the uniaxial easy axis; the extended feature perpendicular to it the magnetic hard axis (see Sec. 3.2 for details). The AMR amplitude and the switching fields, i.e. the size of the fingerprint pattern, decrease significantly with temperature (note the different magnetic field scales).

This is consistent with detailed SQUID studies by M. Sawicki and coworkers [Wang 05b, Sawi 05]. They extracted the anisotropy constants  $K_{cryst}$  and  $K_{[\bar{1}10]}$  from hard axis magnetization measurements vs magnetic field and showed that the two terms exhibit different temperature dependence. In particular, they showed, that the temperature dependence of the anisotropy constants originates in their power-law dependence on the volume magnetization  $M$ . While the uniaxial anisotropy constant is proportional to the square of  $M$ , the biaxial term depends on  $M^4$ . As a result, the biaxial anisotropy term, which dominates the magnetic behaviour at 4 K, decreases much faster with increasing temperature than the uniaxial term. This is the reason why the magnetic anisotropy undergoes a transition from mainly biaxial to mainly uniaxial when the temperature increases from 4 K to  $T_C$ .

Fig. 3.16a shows SQUID measurements done in Würzburg on the sample of Figs. 3.14 and 3.15. After magnetizing the sample along a given direction, we measure the projection

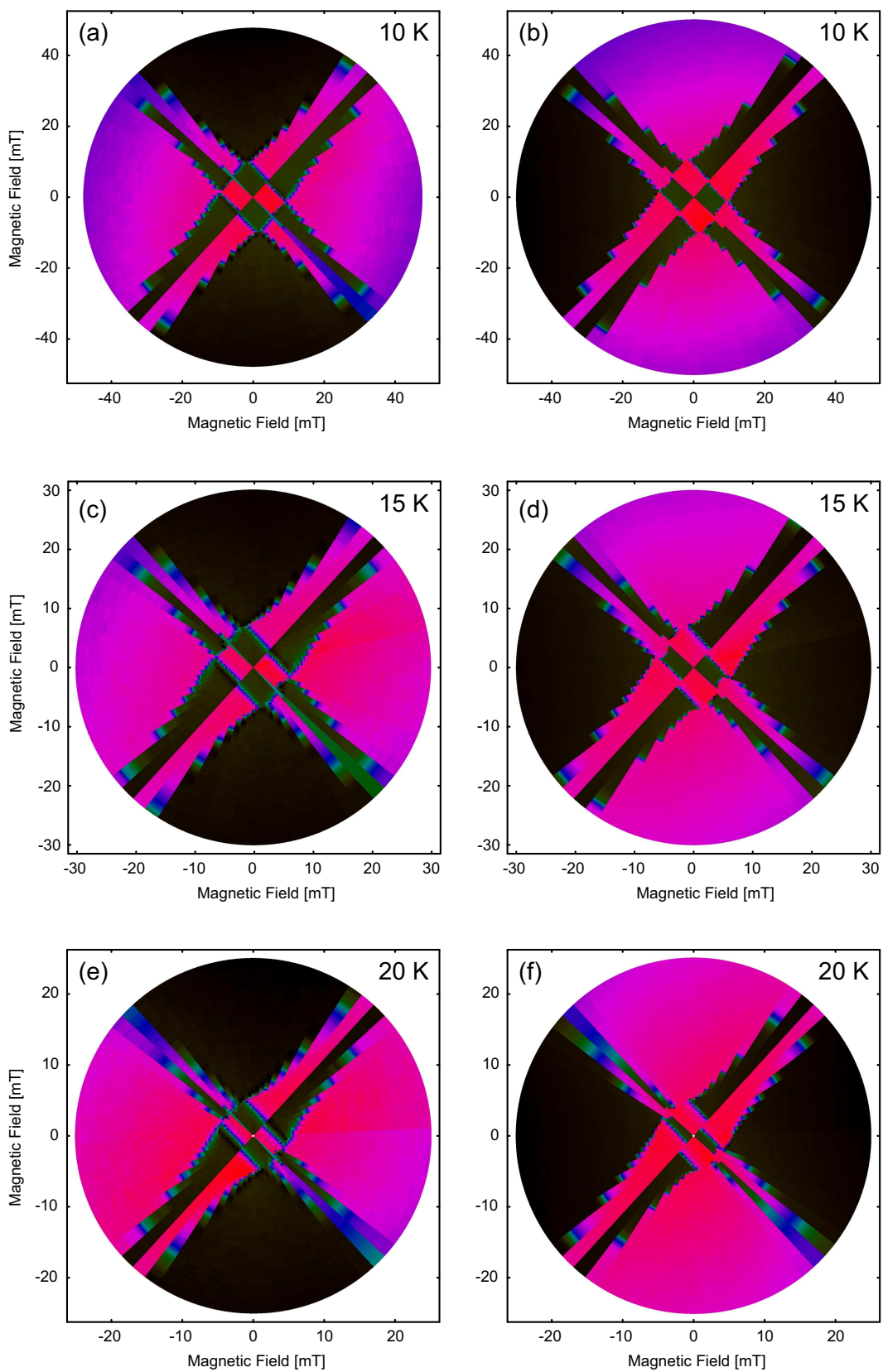


**Abb. 3.14:** Temperature dependent AMR fingerprint measurements of the sample in Fig. 3.9a and b (right column) with current along  $0^\circ$  and Fig. 3.9c and d (left column) with current along  $90^\circ$ .



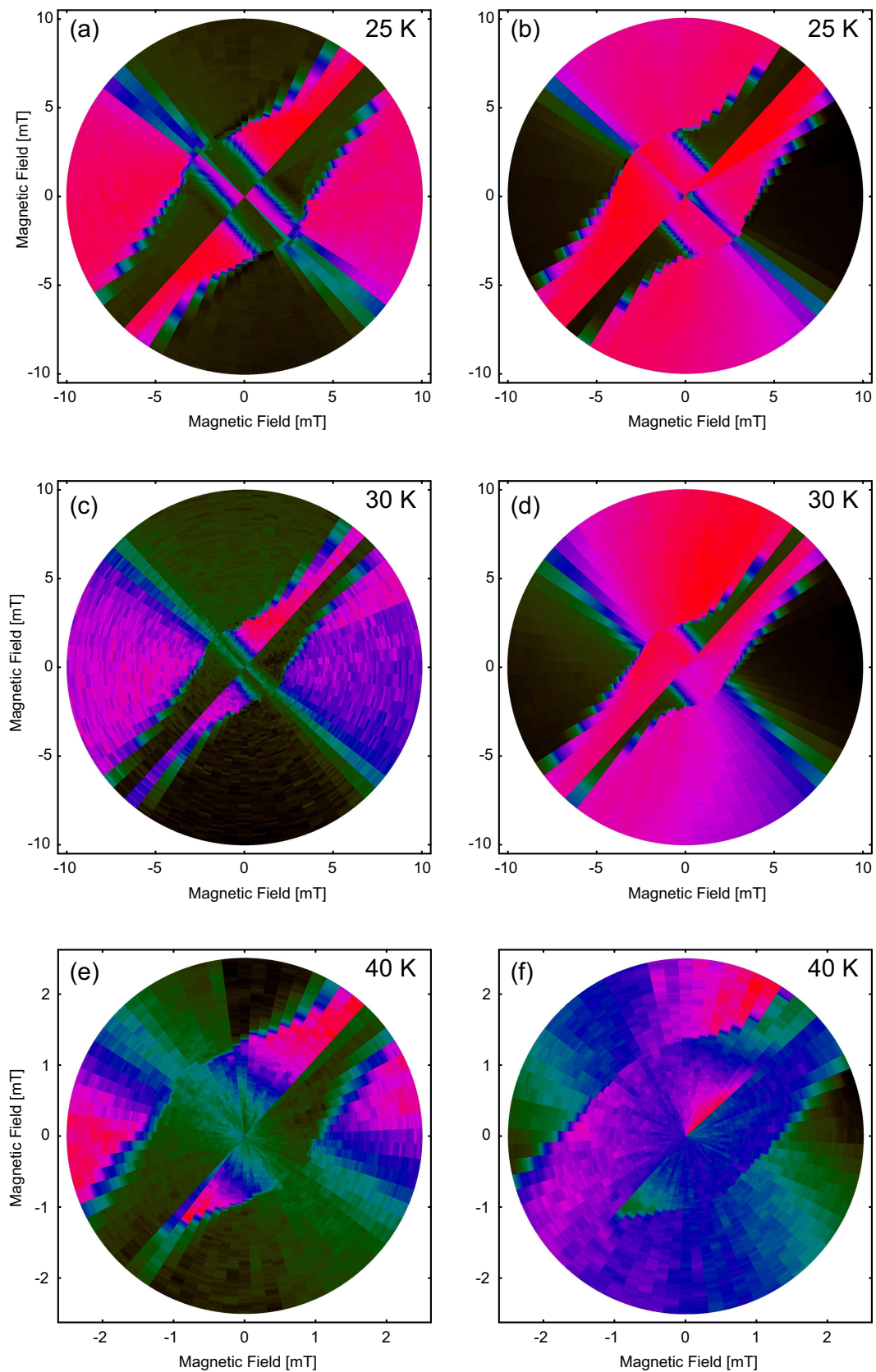


Abb. 3.15: High temperature AMR fingerprint measurements, continuation of Fig. 3.14.

of the remanent magnetization on the respective axis and its evolution with increasing temperature. Displayed are measurements along the two 4 K hard magnetic axes  $[110]$  and  $[\bar{1}10]$  and one of the biaxial easy axes  $\langle 010 \rangle$ . They show the same anisotropy transition as the fingerprints above. At 4K, the  $\langle 010 \rangle$  crystal direction is close to a global magnetic easy axis and thus shows the largest projection of the remanent magnetic moment. The  $[\bar{1}10]$  direction coincides with the easy axis of the uniaxial  $K_{uni[\bar{1}10]}$  anisotropy term. That is why it is closer to a global easy axis than the  $[110]$  direction<sup>1</sup> and consequently shows a larger projection of the remanent moment. As temperature increases, the magnetization decreases and the relative amplitude of the anisotropy terms changes, as described above. This results in a gradual reorientation of the global easy axes with temperature, changing the angle between remanent magnetization (along the global easy axis closest to the sweep direction in Fig. 3.16a) and the respective sweep direction. The result of both the decreasing volume magnetization and changing relative projections onto the different sweep directions, can be seen in Fig. 3.16a. The green  $[\bar{1}10]$  remanence, e.g., gains relative weight with increasing temperature. This supports the observations of the fingerprint measurements, where the  $[\bar{1}10]$  anisotropy term gains in influence at higher temperatures. Given the specific anisotropy behaviour, known from the transport measurements, we can estimate the absolute value of the remanent magnetization from the square root of the sum of the squares of the two magnetization projections along  $[\bar{1}10]$  and  $[110]$  (Pythagorean theorem) [Wang 05b]. The result is displayed in gray in Fig. 3.16a. Such a magnetization measurement with SQUID is complementary to transport investigations, since those can only give energy scales in field units, i.e. normalized to the volume magnetization like  $K/M$  or  $\varepsilon/M$ .

The quantitative determination of the anisotropy constants at higher temperatures is more complex than at 4 K and work is ongoing to find a set of straightforward rules as for the mainly biaxial system at 4 K. Determining the domain wall nucleation/propagation energy  $\varepsilon$ , however, is possible with the described techniques. Black symbols in Fig. 3.16b show preliminary results determined from the fingerprints in Figs. 3.14 and 3.15. The line is a guide to the eye. The method for the extraction builds on the techniques described in section 3.1.1:  $2\varepsilon/M$  is basically given by the diagonal of the rectangular first switching field pattern for mainly biaxial samples and by the easy axis direction diameter for purely uniaxial samples. The strength of this method is that we can extract  $\varepsilon_{90^\circ}$  easily from the plots, because the global easy axes directions are obvious from symmetry considerations. It is not necessary to assume a constant (or known) global easy axis direction and we can thus fully account for the complex temperature dependence of the easy axis behaviour without fitting the data to a complicated model. Both the determination of  $M$  and of  $\varepsilon/M$  are not as accurate in the transition region, where the energy surface at zero field is almost flat over a wide angular range. This is the probable cause of the deviation from perfect exponential behaviour for the data in Fig. 3.16b at intermediate temperatures.

---

<sup>1</sup>See Fig. 3.6, where  $[110]$  is along  $45^\circ$  and  $[\bar{1}10]$  along  $135^\circ$ .

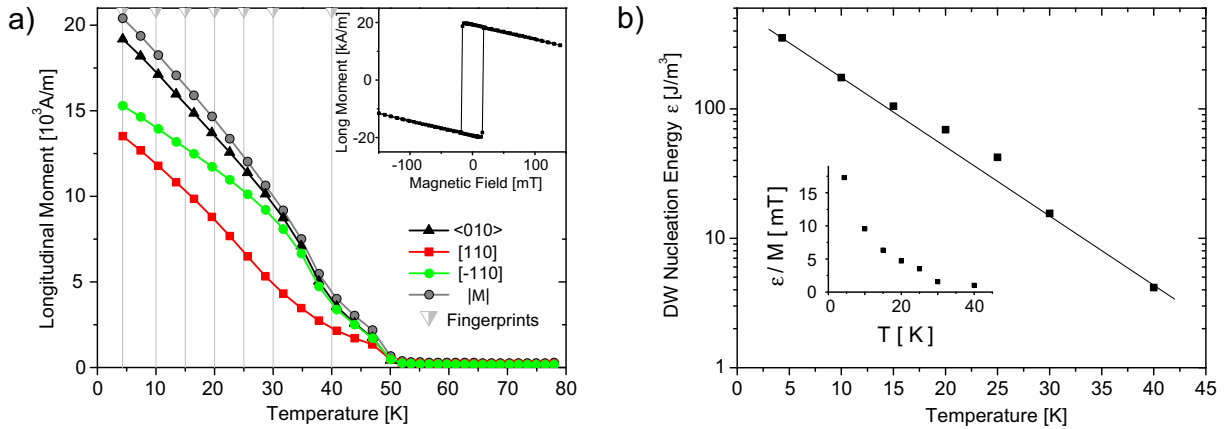


**Abb. 3.16:** a) Measurement of the projection of the remanent magnetic moment of the sample of Figs. 3.14 and 3.15 onto different crystal axes by SQUID magnetometry. Vertical gray lines indicate the temperatures of the fingerprint measurements in Figs. 3.14 and 3.15. b) Domain wall nucleation energy  $\epsilon_{90^\circ}$  (symbols) versus temperature, derived from  $\epsilon_{90^\circ}/M$  (inset) extracted from the fingerprints.

The square hysteresis loop with abrupt switching events, shown in the inset of Fig. 3.16a, points to a DW nucleation dominated process, as opposed to a process, where the energy needed for DW propagation is the limiting parameter [Ferr 02]. Also the temperature dependence of the DW nucleation energy in Fig. 3.16b fits to the standard exponential behaviour expected for the temperature dependence of the coercivity<sup>2</sup> [Chap 07, Vert 95]. Certainly, a more thorough investigation of this and several other samples with different parameters is necessary to complete these preliminary studies. We suggest that the above method is one tool that, in combination with, e.g., time dependent and optical investigations, can clarify the DW nucleation process in (Ga,Mn)As. It can complement recent optical studies, that identify the nature of pinning centers and visualize the process of DW-related magnetization switching in (Ga,Mn)As [Wang 07].

SQUID studies by M. Sawicki on another sample are shown in Fig. 3.17a. As in Fig. 3.16a we plot the projection of the remanent magnetic moment vs temperature. Shown are measurements along the two biaxial easy axes (red and purple) and along the two bisecting directions (green and blue). The absolute value of the volume magnetization estimated as discussed above (gray). The large difference between the two biaxial easy axes directions (red and purple) at intermediate temperatures (25 to 60 K) points to a symmetry breaking caused by a relatively strong uniaxial  $[010]$  anisotropy component. For this reason we investigate this sample at 35 K, where the  $[010]$  component should be strongly visible in the symmetry of the fingerprint pattern, and where the transport

<sup>2</sup>The extraction method already accounts for the correction of the temperature dependence of the anisotropy and the understanding of the respective fingerprint pattern guaranties that only switching events due to DW nucleation are analyzed, as distinct from switching events that are caused by Stoner-Wohlfarth rotation. The "constant anisotropy" criterion for the exponential behaviour is thus satisfied.

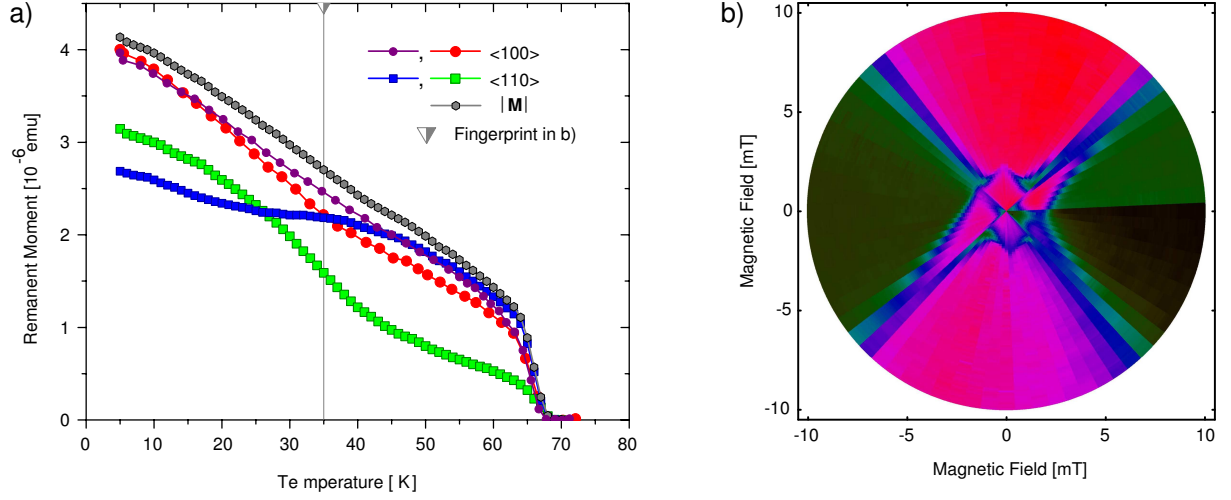


**Abb. 3.17:** a) Projection of the remanent magnetic moment of a 20 nm thick (Ga,Mn)As layer measured with SQUID along different crystal axes. 35 K, the temperature of the anisotropy fingerprint measurement<sup>3</sup> in b) is indicated by a vertical gray line.

signal is still large enough to get clean measurements. Fig. 3.17b shows the resulting fingerprint. The symmetry breaking between the two biaxial easy axes (here along  $0^\circ$  and  $90^\circ$ ) is apparent from the picture. The relatively strong uniaxial  $[010]$  term causes a preference for the magnetization orientation along  $90^\circ$ . The resistance polar plot in turn resembles in parts a typical biaxial fingerprint pattern (between  $45^\circ$  and  $135^\circ$  and the point symmetric region) and in the other quadrants a typical uniaxial fingerprint pattern (between  $135^\circ$  and  $225^\circ$ ).<sup>3</sup> We can thus conclude, that the relatively small uniaxial term gains in importance at intermediate temperatures in this sample. This is where the two stronger anisotropy terms have approximately equal weight, compensating each other in specific angular regions. A small extra term in the energy equation then plays a huge role: it creates an additional local minimum in the energy surface, causing very different switching behaviour in different quadrants of the polar plot.

In summary, the anisotropy fingerprint technique has application potential also at elevated temperatures. Further research in this direction is still needed to find detailed descriptions of the resulting fingerprint patterns and corresponding extraction rules for quantitative analysis. The overall behaviour of the anisotropy terms is consistent with SQUID investigations, showing the typical transition from a mainly biaxial to a mainly uniaxial material with increasing temperature.

First preliminary results show that an extraction of the  $90^\circ$ -DW nucleation energy and its temperature dependence is possible. At the temperatures investigated, the energy to nucleate a DW is orders of magnitude larger than thermal fluctuations  $\sim kTV$ , where  $V$

<sup>3</sup>The small resistance deviation of  $\sim 0.7\%$  in the last quadrant is caused by temperature drift. The temperature decreased by  $\sim 1K$  during the measurement between  $\sim 300^\circ$  and  $360^\circ$ , changing the relative weight of the biaxial and the uniaxial anisotropy components, slightly modifying the fingerprint pattern in this section.

is the volume of a typical sample. Measurements have also shown, that the [010] uniaxial anisotropy term, whose existence is sometimes questioned, can be observed. We show that it can have a particularly strong impact on the switching behaviour for cases where the cooperative effect of the biaxial and the  $[\bar{1}10]$  uniaxial anisotropy term lead to a flattened energy surface. This was exemplified in the above samples at intermediate temperatures.



# Chapter 4

## Current Assisted Magnetization Manipulation

Current induced magnetization switching at temperatures just below  $T_C$  [Yama 04] and resistance associated with domain walls pinned in nanoconstrictions [Rust 03] have both been previously reported in (Ga,Mn)As based devices, but using very dissimilar experimental schemes and device geometries. Here we report on the simultaneous observation of DW pinned at constrictions and of current assisted magnetization switching effects at 4 K in a single nanodevice, which constitutes a significant step forward towards the eventual realization of all electrical spintronic memory devices.

A future all electrical semiconductor memory architecture poses several challenges, typically classified in writing, storing reading and processing information. In this chapter we will discuss the manipulation of magnetization by current, a possible electrical writing scheme. Obviously measuring and understanding the anisotropy of magnetic semiconductor layers and, even more important, of the patterned device components is a prerequisite for these investigations. We will thus build on chapter 2 and 3 and use transport measurements to investigate the magnetization behaviour.

Current induced switching is well established in metals [Slon 96, Berg 00], but currently operates only at switching current densities of  $10^7$ - $10^8$  A.cm<sup>-2</sup>, exceeding the value tolerated in modern integrated circuit technology [Mura 88, Mich 02]. It has however been predicted [Tata 04] theoretically, and recently demonstrated experimentally [Yama 04], that current induced switching in ferromagnetic semiconductors (FS) can be achieved for current densities 2 to 3 orders of magnitude lower than in metals. In that experiment, a variation in layer thickness was used to demark the various regions of a (Ga,Mn)As device with an easy magnetic axis perpendicular to the layer plane. Current induced switching of a central region was observed by magneto-optical Kerr effect (MOKE) and anomalous Hall measurements in this device operating a few degrees below its Curie temperature using a current density of  $8 \times 10^4$  A.cm<sup>-2</sup>.

A second potentially important advantage of FS over their metallic counterparts was the prediction [Flat 01, Vign 02] that domain wall resistance in FS should be significantly

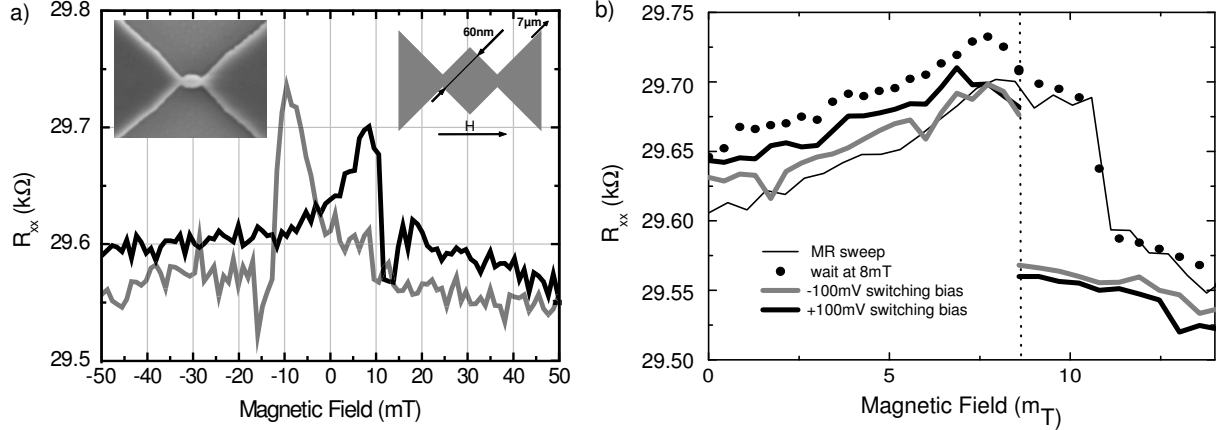


**Abb. 4.1:** (a) Full magnetoresistance scan at 5 mV for magnetic field parallel to the current showing the spin valve signal of the device. The insets show a scanning electron microscope (SEM) image and a schematic of the device. (b) Four magnetoresistance sweeps of the device, after saturating at -50 mT. Three of the sweeps were interrupted at 8 mT as described in the text.

larger than in metals. This has also been experimentally confirmed in (Ga,Mn)As devices [Rust 03], where a large change in device resistance was observed, associated with the pinning of a domain wall in a nanoconstriction between regions of opposite in-plane magnetization.

In the present work, we show results on samples which combine both of the above elements in a single device and show that they can be mutually compatible. Our device is a lithographically defined nanostructure patterned in a 20 nm thick low temperature  $\text{Ga}_{0.94}\text{Mn}_{0.06}\text{As}$  layer grown on a GaAs buffer with an as-grown Curie temperature of  $\sim 70$  K. This layer is then patterned into nanostructures as shown in the SEM image and schematic diagram inset in Fig. 4.1a. The structure is defined using a negative e-beam lithography process, and chlorine based dry etching. It is comprised of a small central island, which is separated from large triangular leads by a pair of nanoconstrictions of  $\sim 10$  nm in width, and is oriented such that the current path is along a (Ga,Mn)As easy axis.

Figure 4.1a shows a 4.2 K magnetoresistance measurement of the device as a magnetic field applied in a direction parallel to the current path is scanned from -50 to +50 mT and back again with a bias voltage of 5 mV. The sample shows a clear spin valve like signature, which can be explained, as discussed in detail in Ref. [Rust 03], by the fact that the large leads will have a much lower coercive field than the small island. As such, when the magnetic field is swept, there exists a field range for which the magnetization in the leads has already reversed while that of the island remains fixed. In this configuration, domain walls will be pinned in each of the nanoconstrictions, and an increase in resistance associated with these domain walls is observed.

We now present evidence that, after setting up the device in this configuration where



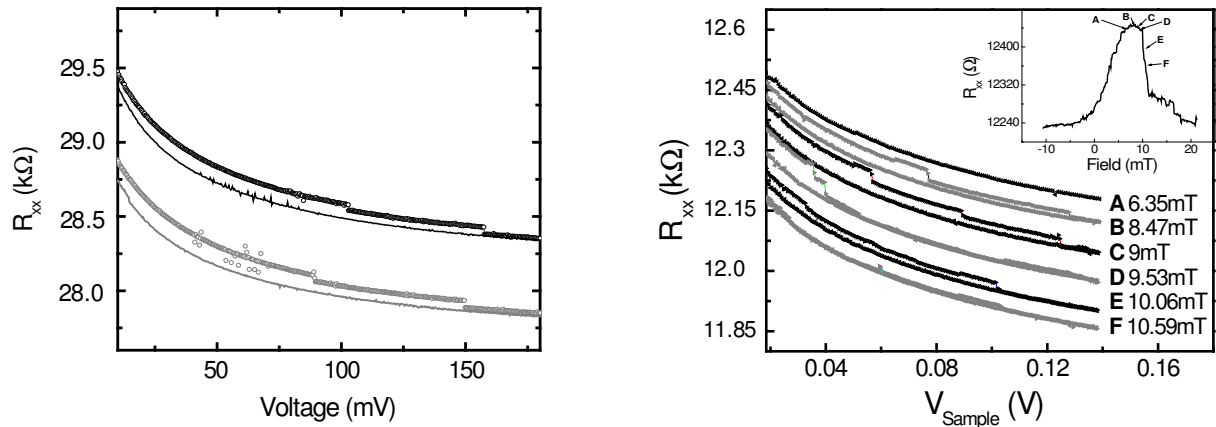


**Abb. 4.2:** (a) Resistance versus voltage measurements at 8 mT for the sample initially prepared in the anti-parallel configuration. The sweeps to higher bias show clear switching events which are absent on the sweeps towards lower bias. (b) Similar measurements on a second sample at different magnetic fields as indicated in the figure. Both sets of curves are offset for clarity.

the central region is anti-parallel to the leads, we can, without further changing the magnetic field, reverse the polarization of the island using a current assisted switching mechanism. This is shown in Fig. 4.1b, where we plot four magnetoresistance measurements. The first, indicated by the solid line is a normal magnetoresistance measurement as in Fig. 4.1a, again taken with a bias voltage of 5 mV. The second scan, with the data displayed as dots, is a similar measurement, except that the scan is stopped at 8 mT (indicated by the vertical dotted line), and several minutes are allowed to elapse before the scan is continued. This interruption has no effect on the measurement. The final two curves are however more interesting. Again, we repeat a similar magnetoresistance measurement, which is stopped at 8 mT. However, this time, instead of simply waiting, we ramp the bias voltage up to +100 mV (dark thick line) or -100 mV (light thick line), and back down to 5 mV before continuing the sweep. The time taken for this process is shorter than the waiting time used for the second curve, but now, when the curves are continued, it is apparent that the central region has already reversed its magnetization as the device is in the low magnetoresistance state. Note that the sign of the magnetization reversing voltage is unimportant as the device and magnetic configuration are symmetric.

While these measurements are done at 4.2 K, well below the Curie temperature of the material, and the total power applied during the current induced reversal is only some 100 nW, because of the small size of the region being switched, one might speculate that local heating is playing a role, warming the (Ga,Mn)As locally above its Curie temperature, and then having it magnetize in the opposite direction as it cools upon removal of the high bias. This hypothesis can however be ruled out by the data presented in Fig. 4.2a. Here we first prepare the sample in the anti-parallel configuration as in Fig. 4.1b, by starting a magnetoresistance scan, and interrupting it at 8 mT. After interrupting the magnetoresistance scan, we remain at this fixed field, and perform a series of resistance

versus voltage measurements. We first measure the resistance while increasing the bias up to 180 mV (dark open circles), and notice, in addition to the smooth and monotonic decrease expected from the non-linear nature of the nanoconstriction resistance, some sharp switching events in the region around 100 mV. Then we measure the resistance as we sweep the bias back (dark solid curve), and find only a smooth increase, without any jumps. At low bias, the two curves differ in resistance by the amplitude of the spin-valve signal. If we now repeat similar bias scans, we obtain the solid curve, both for the sweep up and sweep down, since the sample is in the parallel state, and the high bias voltage can have no further effect. While it is difficult to get exact numbers for the dimensions of the constrictions, using reasonable estimates, we get a typical switching current density of  $\sim 1 \times 10^6 \text{ A.cm}^{-2}$ .

Repeating the full measurement several times by preparing the anti-parallel state before each sweep up in bias does yield qualitatively reproducible results, in the sense that sharp switching events are observed in every attempt. A second such measurement is shown as the light data in Fig. 4.2a (The curves having been offset for clarity). Note that the positions of the switching events vary from one data set to the next (and occasionally, even the number of switching event varies). This is probably due to the fact that the nanoconstrictions, due to their small size, are extremely sensitive to minute imperfections in their side-walls. As a result, each nanoconstriction is seeded with multiple, nearly equivalent, pinning centers, which act to pin the domain wall at slightly different positions in each successive measurement, leading to a different geometrical confinement of the domain wall, and thus a different domain wall resistance. Indeed, a similar effect attributed to multiple pinning centers was observed in the magnetoresistance measurements of Ref. [Rust 03] .

The measurements presented in Fig. 4.2a were performed at a magnetic field of 8 mT. In Fig. 4.2b, we present the results of similar measurements on a second sample, where we repeat the experiment multiple times, stopping at various points on the magnetoresistance curve indicated in the inset of the figure. The curves at 8.47, 9, 9.53, 10.06, and 10.59 mT all show clear switching behaviour. No abrupt switching was observed at magnetic fields below 6.5 mT (as for example in the 6.35 mT curve from the figure) or above 11 mT (not shown). Interestingly, for the entire field range between 6.5 and 11 mT where switching events are observed, there is no correlation between the position (or number) of switching events, and the field at which the experiment was performed. The total amplitude of the sum of all switching events on a given curve does of course depend on the magnetic field at which the measurement is performed since the total amplitude must be consistent with the amplitude of the magnetoresistance spin valve signal.

The mechanism driving the current assisted switching in these devices can not be unambiguously determined. The results of Fig. 4.2a preclude the idea that we are heating above  $T_C$ . The discontinuous change in resistance at the switching event is inconsistent with the idea of heating above  $T_C$ , which is a smooth phase transition in (Ga,Mn)As. The latter can, however, not completely rule out heating as playing a role. One could

speculate that local heating of the sample to a temperature below its Curie temperature, but sufficiently high to change its coercive field, causes a lowering of the switching field causing the reversal of the central region under the applied magnetic field. We find this explanation unsatisfactory however, both because we would not expect significant heating at the power levels used, and because under this model, for measurements done at lower field, a correspondingly greater reduction of the coercive field would be needed. This should lead to a strong dependence of the switching bias on the magnetic field, which is clearly incompatible with the results of Fig. 4.2b.

For this reason, we believe that the mechanism most likely at work here is the same as invoked in Ref. [Yama 04]; namely a p-d exchange mediated spin angular momentum transfer between the current carrying itinerant holes, and the localized Mn spin in the central region [Tata 04]. That controlled current assisted magnetization manipulation is possible in (Ga,Mn)As is also supported by recent experiments in other device geometries [Chib 04, Wund 07].

In summary, we have demonstrated a current assisted reversal of the magnetization in a localized region of (Ga,Mn)As, detected by electrical transport measurements of the resistance associated with domain walls trapped in nanoconstrictions. We believe the combination of these two effects in a single device is an important step forward towards the eventual realization of ferromagnetic semiconductor spintronics memory devices. Its combination with local anisotropy engineering discussed in chapters 6 and 7 has the potential of yielding an all-electrical all-semiconductor memory architecture.



# Chapter 5

## Magnetization-Switched MIT in a TAMR Device

A novel magnetoresistance effect was discovered in 2004 in a (Ga,Mn)As tunnel structure containing only a single magnetic layer [Goul 04]. The effect was dubbed Tunnelling Anisotropic MagnetoResistance (TAMR). The same effect but with much stronger amplitude was later observed in a structure with (Ga,Mn)As layers on both sides of an epitaxial tunnel barrier [Rust 05]. This previous work highlighting the importance of the density of states (DOS) in the tunnel process is briefly reviewed in section 5.1.

We then investigate the origin of the giant amplification of the TAMR signal in the second structure especially at low temperatures. Here we show with the help of DOS spectroscopy that a thin depleted (Ga,Mn)As injector layer is switched from metallic to insulating by a magnetization reorientation. This thin layer is responsible for the transport properties of the structure. That is why its transition from the metallic to the insulating regime causes a large resistance difference between the two non-volatile TAMR states.

### 5.1 Previous Work

#### 5.1.1 Tunnelling Anisotropic Magnetoresistance (TAMR)

The TAMR effect was discovered by Gould et al. [Goul 04] in a (Ga,Mn)As/amorphous AlO<sub>x</sub>/Ti/Au stack with a surrounding W/Au bottom electrode, as illustrated in Fig.5.1a. The AlO<sub>x</sub> tunnel barrier dominates the device resistance in this current perpendicular-to-plane geometry. Magnetoresistance measurements at 4 K with magnetic fields along several in-plane angles yield spin-valve-like signals reminiscent of tunnelling magnetoresistance experiments (TMR), but of varying width and sign (Fig. 5.1b). The switching fields of a full set of magnetoresistance measurements are summarized in the polar plot in Fig. 5.1c. The switching events can be correlated with the magnetization direction changes in the (Ga,Mn)As. Additionally, it can be concluded from the symmetry pattern of the polar plot that the (Ga,Mn)As layer exhibits a mainly biaxial magnetic anisotropy

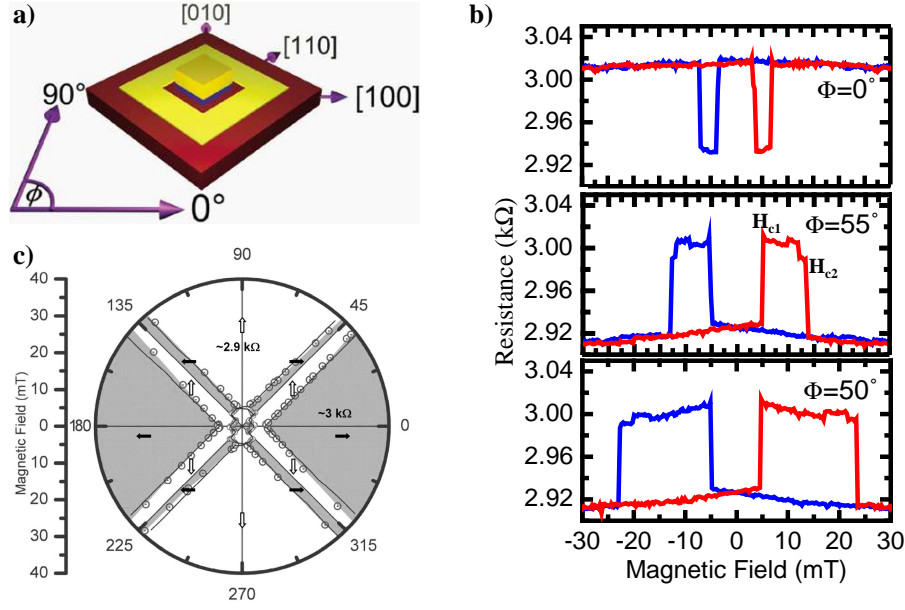


**Abb. 5.1:** a) Sketch of the single sided TAMR structure b) spin-valve like magnetoresistance curves with magnetic field along  $0^\circ$ ,  $50^\circ$  and  $55^\circ$  c) Polar plot summarizing the switching fields for magnetic field sweeps along various angles. [Goul 04]

(easy axes:  $0^\circ, 90^\circ$ ) with a uniaxial component along one of the biaxial easy axes ( $90^\circ$ ) as discussed in chapter 3. Very little elongation compared with the ideal 12-sided polygon pattern (Fig. 3.5b) shows that the typically observed  $[\bar{1}10]$  uniaxial anisotropy component is relatively small in this sample. This is however not relevant to the explanation of the non-volatile TAMR effect because the  $[\bar{1}10]$  anisotropy component does not break the symmetry between the  $[100]$  and  $[010]$  direction.

The explanation of the behavior of the single-sided spin-valve structure (with a ferromagnet only on one side of the tunnel barrier) looks at the dependencies of the tunnel conductance  $G$  on the magnetization direction.

$$G \propto DOS_{Au}(E_F) \times T \times DOS_{GaMnAs}(E_F) \quad (5.1)$$

Both, the DOS of Au and the tunnel matrix element  $T$ , do not depend on the magnetization direction in the (Ga,Mn)As layer. The focus of the explanation is thus the anisotropy of the (Ga,Mn)As DOS with respect to magnetization direction.

The origin of the uniaxial magnetic anisotropy seen in the polar plot is still unclear. It breaks the symmetry between the  $[100]$  and  $[010]$  crystal direction. Theoretically this is modelled phenomenologically by introducing a small in-plane uniaxial strain which leads to a sizable uniaxial anisotropy through spin-orbit coupling. The band structure of (Ga,Mn)As including the strain term is modelled using a k.p-approach. The DOS at the Fermi energy is then calculated assuming partial momentum conservation in the tunnelling

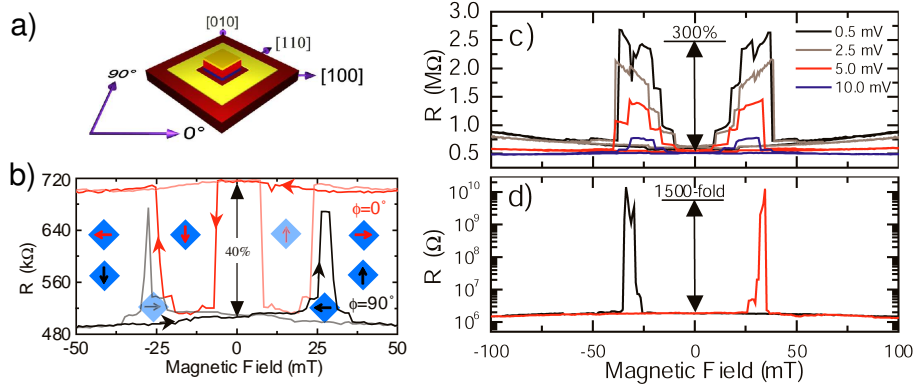


**Abb. 5.2:** a) Sketch of the TAMR device with two magnetic layers. b) Magnetoresistance showing a non-volatile TAMR signal of 40%. Red and black arrows illustrate the magnetization direction in the red ( $0^\circ$ ) and black ( $90^\circ$ ) curve with respect to the  $(\text{Ga,Mn})\text{As}$  cleaving edges  $\langle 110 \rangle$  (blue square) c) Bias dependence of the TAMR signal d) Giant amplification at 1.7 K.

process. The resulting difference in  $(\text{Ga,Mn})\text{As}$  DOS at the Fermi energy for the two easy axes magnetization directions can explain the experimental results. It predicts a stronger TAMR signal with increasing momentum conservation, i.e. for cleaner more crystalline barriers.

### 5.1.2 TAMR in an Epitaxial Structure

In Ref. [Rust 05] TAMR was studied in an epitaxially grown  $(\text{Ga,Mn})\text{As}(10 \text{ nm}) / \text{GaAs}(2 \text{ nm}) / (\text{Ga,Mn})\text{As}(100 \text{ nm})$  structure with 6% Mn (Fig. 5.2a). The stack was contacted in-situ by Ti/Au evaporation and patterned into a  $100 \times 100 \mu\text{m}^2$  pillar with optical lithography and chlorine assisted ion beam etching. The surrounding back side electrode contacting the lower  $(\text{Ga,Mn})\text{As}$  layer was established by optical lithography, W/Au deposition and lift-off.

As in the previous section the current flows vertically through the stack and the resistance is heavily dominated by the tunnel barrier. (Identically patterned control samples have a resistance of  $\sim 10 \Omega$ .) Spin-valve signals with an amplitude of 40% with varying sign and width were observed at 4 K (Fig. 5.2b). The data in Fig. 5.2b can be explained by the TAMR effect as discussed in the previous section. A large number of mid-gap traps pin the Fermi energy of the epitaxial low-temperature GaAs layer in the middle of the semiconductor band gap. It now acts as an epitaxial tunnel barrier with high momentum conservation. A larger TAMR signal compared with the  $\text{AlO}_x$  tunnel barrier is thus expected. Additionally both  $(\text{Ga,Mn})\text{As}$  layers change their magnetization direction approximately at the same magnetic field in a magnetoresistance measurement. The layer magnetizations are thus almost always parallel and both DOS contribute to TAMR.

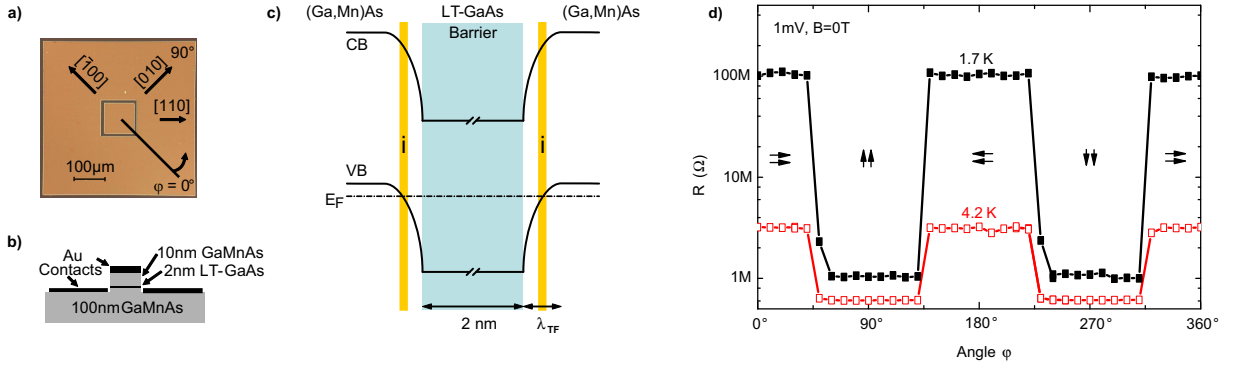


**Abb. 5.3:** a) Optical micrograph of the sample. b) Sample layer structure. c) schematic band diagram illustrating the barrier for hole transport, the depletion region near the interfaces, and the effective injector layers (*i*). d) 4.2 K and 1.7 K magnetoresistance in zero field at 1 mV bias after preparing the sample by magnetizing in various field directions.

The effect is strongly amplified at lower bias voltages (Fig. 5.2c) and is extremely sensitive to temperature changes. Fig. 5.2d shows a magnetoresistance measurement at 1.7 K and 1 mV bias, where the current through the structure in the high state is below the detection limit of the amplifiers (the 150000% corresponds to the amplifier floor). The symmetry of the effect and the smooth bias dependence suggest, that the TAMR effect is still at work, but amplified by an additional mechanism.

## 5.2 Origin of the Giant Amplification

A key element in the explanation of the large amplification is the LT-GaAs tunnel barrier containing many mid-gap traps, and thus acting as an effective carrier sink. The result is a thin depleted (Ga,Mn)As region near the barrier and band bending near the interfaces, as sketched in Fig. 5.3c. As a consequence of this a thin effective injector layer (*i*) in Fig. 5.3c) is responsible for the tunnelling properties of the structure. The following DOS-spectroscopy experiments show that the injector layer is close enough to the Metal-Insulator-Transition (MIT), that it can be driven from the metallic to the insulating regime and back by the DOS-change associated with a magnetization reorientation.

We first concentrate on the two remanent (non-volatile) magnetization states of the structure corresponding to the resistance states shown in Fig. 5.3d. As preparation, the sample is magnetized ("written") along a specific angle  $\varphi$  in the sample plane in an external field of 300 mT. One of the magnetic easy axes of the (Ga,Mn)As layers, defined as  $\varphi = 0^\circ$ , is along the [100] crystal direction. The second, perpendicular, easy axis is along [010] corresponding to  $\varphi = 90^\circ$ . Fig. 5.3a and b show sketches of the structure illustrating the coordinate system used. As the field is swept to zero, the magnetization of both layers relaxes to the nearest easy axis, and this magnetization state determines the resistance. Fig. 5.3d illustrates the results of such measurements at 1 mV for many preparation angles



$\varphi$ . The arrows indicate the magnetization orientation of the two (Ga,Mn)As layers.

The 4.2 K-curve can be understood as resulting from TAMR as explained in the previous section[Goul 04]: the anisotropy in the momentum dependent DOS with respect to magnetization direction ([100] or [010]) causes a resistance difference between the two magnetization orientations.

### 5.2.1 The Metal Insulator Transition (MIT)

While TAMR is a band-structure effect, the extreme amplification between 4.2 K and 1.7 K can only be understood by considering many particle effects. Coulomb interactions between the charges cause a characteristic DOS singularity around the Fermi energy as screening is reduced when the MIT is approached from the metallic side. For disordered metals above the Anderson transition Al'tshuler and Aronov[Alts 79] found that the single particle DOS has a square-root singularity around the Fermi energy because of electron-electron repulsion. This DOS singularity manifests itself in tunnel experiments in square-root-like conductance-voltage characteristics with the lowest conductance at zero bias. Efros and Shklovskii [Efro 75] studied the deeply insulating regime and found that also there the DOS shows a singularity at the Fermi energy. A soft gap (Efros-Shklovskii-gap, ES-gap) induced by Coulomb correlations appears near the Fermi level of a Mott insulator. The DOS vanishes at  $E_F$  and has a parabolic energy dependence in three-dimensional systems. The ES-gap is observable in low-bias tunnelling conductance spectra. It causes a parabolic conductance-voltage dependence with zero conductance at zero bias voltage.

### 5.2.2 Density of States Spectroscopy

The above was experimentally observed by Lee et al. [Lee 99] in their investigations of tunnelling from a metal into disordered boron-doped silicon near the MIT. The DOS-gap around the Fermi energy is observable in the low bias tunnelling conductance. It manifests itself in a different power law behavior  $G(V) \propto V^m$ , with  $m = 1/2$  for metallic (just above the MIT) and  $m \geq 2$  for insulating (below the MIT) material.

To further investigate the effect in our structure the differential conductance  $G(V) = dI/dV$  in Fig. 5.4a is calculated from current-voltage-characteristics taken in the remanent magnetization state after writing the device at an angle  $\varphi$ . In Fig. 5.4a, the  $G(V)$  curves at 1.7 K are segregated into two groups associated with each of the two resistance states identified in Fig. 5.3d. The magnetization of both (Ga,Mn)As layers relaxes into the low resistance state corresponding to magnetization along [010] for all preparation angles between  $45^\circ$  and  $135^\circ$  (upper/green curves in Fig. 5.4a). It relaxes along the [100]-high-resistance state for preparation fields within  $45^\circ$  of the [100] direction (lower/blue curves).

The  $G(V)$  characteristics have a distinct shape for each magnetization direction. High conductance curves are square-root-like and show non-vanishing conductance at zero voltage. As described above this is typical for the metallic behavior of highly doped semicon-

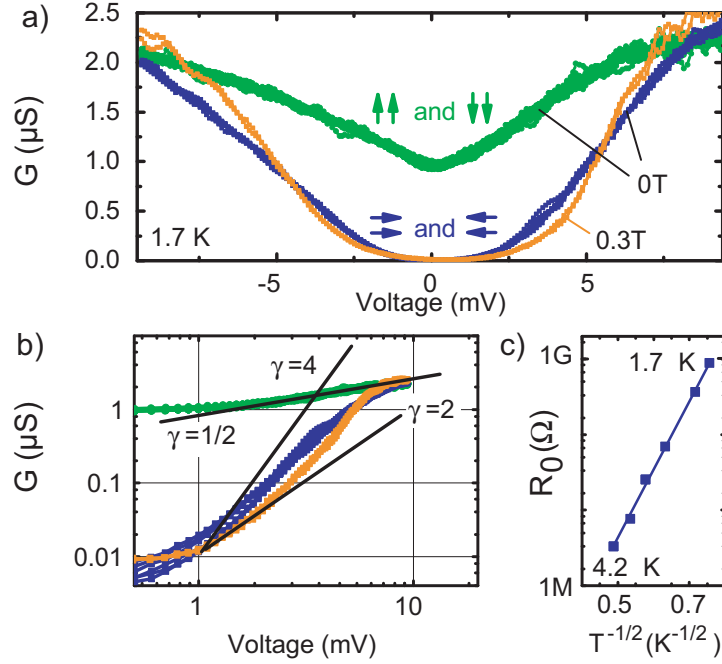


**Abb. 5.4:** a) Differential conductance-voltage curves at  $1.7\text{ K}$  including sets of curves belonging to the two magnetization states at  $B=0$ , and one set at  $B=300\text{ mT}$  along  $\varphi = 3$  and  $6^\circ$ . b) Log-log plot of same data. c) Temperature dependence of the zero bias resistance of the high resistance state.

ductors (here (Ga,Mn)As) taking part in the tunnel process [Alts 79]. The high resistance state, however, shows insulating behavior. The conductance vanishes at zero voltage and the curves follow a higher power law as can be seen in the log-log plot of Fig. 5.4b.

Larkin and Shklovskii [Lark 02] derived a power law behaviour for conductance versus voltage ( $G$ - $V$ ) curves for tunneling between two three dimensional localized materials where the parabolic DOS  $D(\epsilon) \propto \epsilon^2$  on each side multiply and lead to  $G \propto V^6$ . In our case, given the very thin nature of the the injector, a 2-D description of the DOS of the tunneling reservoirs is likely more appropriate. Thus, the DOS is linear in energy, and the expected power of the  $G$ - $V$  curves is 4. Moreover, it is unclear in our experiment whether both sides of the barrier play an equivalent role, or whether the effects are dominated by one electrode. Depending on the relative role of the two barriers, one would thus expect a power law somewhere between  $\propto V^2$  and  $\propto V^6$ . Neglecting very low voltages where thermal smearing is important, this prediction is in good agreement with the experimental observation of Fig. 5.4a and b. Additionally we can of course not rule out that the change in screening causes a slight shift in position of the effective injector thus modifying the tunneling distance, and accounting for part of the observed resistance change.

The transition from metallic to insulating behavior is thermally activated as demonstrated by the zero bias differential resistance data taken at an angle corresponding to the high resistance state at  $1.7\text{ K}$ , shown in Fig. 5.4c. The plot shows that the data is consistent with an exponential activation following  $R \propto \exp(1/T)^{1/2}$  expected for an ES-gap ma-

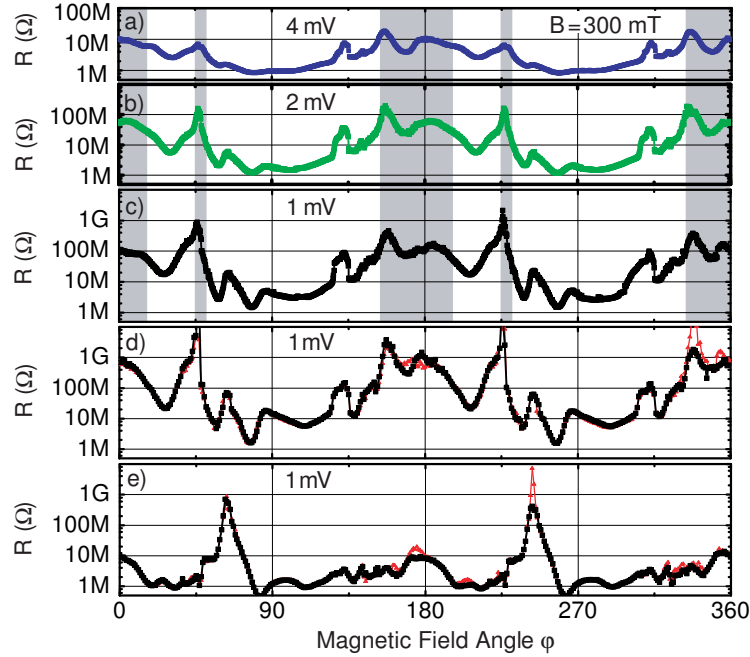


**Abb. 5.5:** Resistance of the sample at 1.7 K and 300 mT as a function of magnetic field direction under various bias and on different cooldowns. d) and e) each show the results of two separate measurement, confirming reproducibility.

terial under the usual assumption of single hop tunnelling [Sand 01, Efro 75, Alts 79]. We note however that because the accessible temperature range spans less than one decade, and we cannot rule out an  $R \propto \exp(1/T)^{1/4}$  dependence expected from a non correlated Mott transition (for which a constant DOS is assumed).

A further clue to the origin of our effect comes from the data of Fig. 5.5 showing the resistance behavior of the sample at 300 mT, a field sufficient to force the magnetization vectors parallel to the field direction for all field angles. The figure shows very strong and apparently random oscillations reminiscent of quantum interference effects, and likely arising from a statistically defined electronic state in the sample. Fig. 5.5 a-c show that the amplitude of these oscillations grows significantly with reduced bias for angular ranges (gray regions in the figure) associated with ES behavior. Fig. 5.5c-e show a significant effect upon thermal cycling to temperatures of some tens of K (above the ES activation temperature). The three curves are nominally identical measurements after subsequent thermal cycling. The main behavior of the device remains unchanged, but the details of the fluctuations change significantly, presumably corresponding to a new impurity configuration. We emphasize that the change in the fluctuation pattern is due to thermal cycling. On a given cooldown, measurements are reproducible as confirmed by the two, almost indistinguishable, sets of measurements included in each of Fig. 5.5d and e.<sup>1</sup>  $G(V)$

<sup>1</sup>The TAMR amplification is such that the current in the high resistant state is comparable to amplifier offsets. A constant offset current was removed from the data before analysis. This brings into question the accuracy of the resistance for values above 1 GΩ.

curves at 300 mT along the  $\varphi = 3$  and  $6^\circ$  given in Fig. 5.4a show similar behavior to the other high resistance angles in Fig. 5.5 marked in gray.

We attribute the fluctuations in Fig. 5.5 to quantum interference effects on the variable range hopping that is the transport mechanism in the insulating state [Raik 87]. In reference [Hugh 96], such quantum interference was confirmed by a statistical analysis of the amplitude of the fluctuations as the Fermi energy is varied using an external gate bias. A similar analysis cannot be reliably applied here as the relation between the magnetization direction and the Fermi energy is complex and non-linear.

The behavior of our sample is fully consistent with the depleted (Ga,Mn)As injection layer undergoing a MIT triggered by a reorientation of the magnetization from [010] to [100], and the formation of an ES-gap. In order to understand how a change in magnetization direction can trigger a MIT, we need to consider the criterion for the passage from metallic to insulating properties.

### 5.2.3 The Wave Function Overlap Determines the MIT

Metallic transport properties require the charge carriers to be in long range itinerant states. This condition implies significant overlap of the wavefunctions between acceptors (Mn atoms). As such, the passage through the MIT depends not only on the carrier density, but also on the volume occupied by the wavefunctions of the states of the individual dopants. Indeed a change in impurity conductivity associated with a strain induced change in Bohr radius has been reported previously [Poll 65].

For (Ga,Mn)As, it is well established [Abol 01, Diet 01] that details of the DOS are influenced by the magnetization direction. To determine if this plays a role in renormalizing the wave function extent of our localized states, we turn to a numerical calculation of bound hole states performed by Manuel J. Schmidt [Schm 07]. The valence band of the host lattice is described in  $\mathbf{k} \cdot \mathbf{p}$  framework by the full Luttinger Hamiltonian [Diet 01] including spin-orbit coupling, pd-exchange, growth strain and a phenomenological uniaxial strain ( $\epsilon_u$ ) term to break the symmetry between the  $\langle 100 \rangle$  directions. Note that, the ferromagnetic properties of (Ga,Mn)As are already contained in the lattice description in this model. The hole wave function is then treated as an envelope function of Bloch waves bound to a non-magnetic Yukawa-like impurity potential. The ground state eigenfunctions in k-space are calculated by solving the time-independent Schrödinger-equation numerically and self-consistently. They are converted to real space using a hydrogen model yielding the representation of a bound-hole wave function shown in Fig. 5.6b. The shape of the wave function depends on the character of the highest valence band, which changes with strain and pd-exchange as can be seen in Fig. 5.6a. Fig. 5.6b shows wave function representations of light-hole like states for the two easy axes magnetization directions. The wave function extent changes strongly with magnetization direction. A magnetization rotation can thus drive a layer which is already close to the MIT from the insulating into the metallic regime (or vice versa) because of the additionally created wave

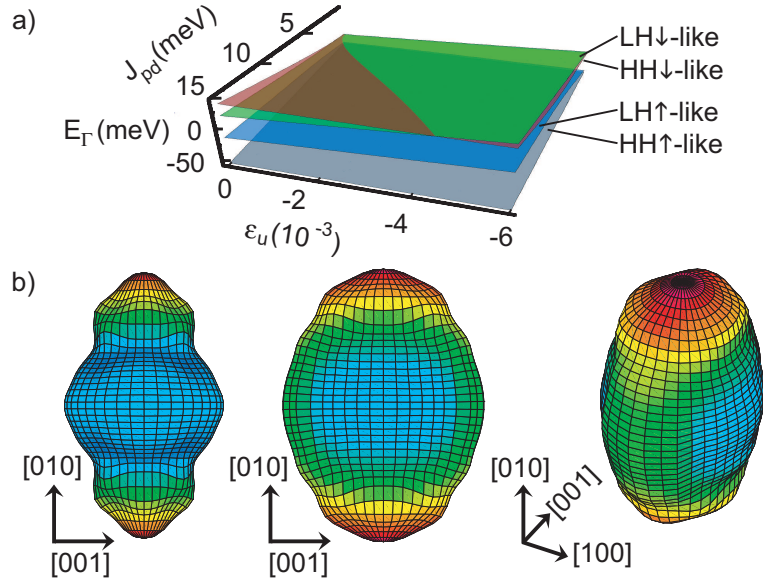


**Abb. 5.6:** a)  $\Gamma$  point energy of the four top bands as a function of strain  $\epsilon_u$  and  $pd$ -exchange. b) Extents of a hole bound to a Mn-impurity.  $[001]$  is the growth direction and  $\epsilon_u$  is along  $[010]$ . Left: Magnetization ( $\mathbf{M} \parallel [100]$ ). Middle: ( $\mathbf{M} \parallel [010]$ ). Right: Perspective view for  $\mathbf{M} \parallel [010]$ . By Manuel J. Schmidt.

function overlap and the herewith formed percolation path for long range transport.

Theoretic calculations can thus explain the experimental observations from DOS-spectroscopy. They yield a different extent of the localized hole wavefunction for the two magnetization directions. This triggers a metal-insulator-transition in a depleted injection layer in the TAMR-sample upon a magnetization reorientation.

It is important to note that the above calculation does *not* predict a MIT for the bulk (Ga,Mn)As which, as typical in high quality (Ga,Mn)As, has nearly temperature independent resistivity in the temperature range of interest. Our prediction is limited to the thin (Ga,Mn)As layer near the interface with the tunnel barrier. The barrier consists of LT-GaAs, a material with many mid-gap traps that lead to gradual spatial depletion of the (Ga,Mn)As near the barrier on the length scale of the Thomas-Fermi screening length of  $\sim 2\text{\AA}$ , and thus to a much lower effective local carrier density, as illustrated schematically in Fig. 5.3c. If the thin depleted layer is close enough to the MIT, a change in the wave function extent can trigger the transition.

A key point here is that while this thin depleted layer plays a limited role in the magnetic properties of the (Ga,Mn)As, it has a dominant effect on the transport. The reason for this lies in the very short mean free path of holes in (Ga,Mn)As which is of the order of a few  $\text{\AA}$ . Combining the fact that, by definition, the transition from diffusive to tunneling transport takes place at a density where holes can no longer classically diffuse, with this extremely short mean free path, must lead to a very thin effective injector layer from which the tunneling originates. This injection layer is characterized by considerably

reduced carrier density relative to the bulk, and thus consistent with our model description above.

In conclusion, we have observed the magnetization reorientation induced MIT in a (Ga,Mn)As based transport sample. The transition can be understood as stemming from a modification of the wave functions of individual dopants due to the coupling of the Mn dopants to the magnetization direction in the bulk. Furthermore, the transition is accompanied by the opening of an ES-gap at the Fermi energy which manifests itself as a change in the power law behaviour in conductance-voltage characteristics in tunneling experiments. While a magnetic induced MIT based on the amplitude of the magnetic field has been reported before [Wojt 86], this is the first observation of a MIT induced by a change in magnetization *direction* in any material. In addition to the fundamental interest intrinsic to these observations, the results may also have technological relevance in opening up new possibilities of controlling the transport properties of devices by magnetization reversal. Indeed, another MIT-related effect is shown to amplify an AMR-related signal in a device presented in chapter 7.

## Chapter 6

# Lithographic Engineering of Anisotropies

The focus of studies on ferromagnetic semiconductors is moving from material issues to device functionalities based on novel phenomena often associated with the anisotropy properties of these materials. Studies so far have primarily made use of the intrinsic anisotropy present in the host (Ga,Mn)As layer.

Before the effects described in section 2.2 can be harnessed to their full potential, a means of engineering the anisotropy locally is needed, such that multiple elements with different anisotropies can be integrated, and their interactions can be properly investigated. Here we present a method which provides patterning induced anisotropy which not only can be applied locally, but also dominates over the intrinsic material anisotropy at all temperatures.

One successful approach to local anisotropy control in metallic ferromagnets has been to make use of shape anisotropy. The same approach has been tried in the prototypical ferromagnetic semiconductor (Ga,Mn)As with lackluster results. In Ref. [Hama 06], the authors reported the observation of shape induced anisotropy in (Ga,Mn)As wires of 100 nm thickness x 1.5 x 200  $\mu\text{m}^2$ , but only over a limited temperature range. Moreover, our own experience in attempting to use wires of similar dimensions have yielded sporadic results with the wires having irreproducible anisotropy, with either biaxial or uniaxial easy axes in inconsistent directions.

Furthermore, a simple calculation of the expected shape anisotropy term in such wires indicates that it should not play a significant role. While the infinite rod model used in [Hama 06] does predict an appreciable shape anisotropy field given by  $\mu_0 M_S/2$ , where  $M_S$  is the sample magnetization, it is not applicable to structures which are much thinner than their lateral dimensions. A more exact rectangular prism calculation [Ahar 98] gives a 5 times weaker shape anisotropy with an anisotropy energy density of 80 J/m<sup>3</sup> which is much too small to compete with the typical crystalline anisotropy of 3000 J/m<sup>3</sup> [Wang 05b, Hama 06] in this material.

The complex magnetic anisotropy of (Ga,Mn)As layers was described in detail in sec-

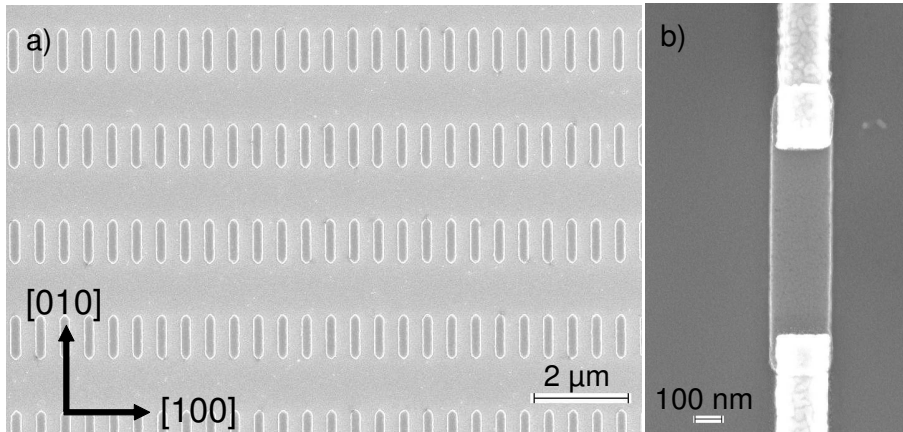


**Abb. 6.1:** a) SEM photograph of a small part of a typical 8 million nanobar array. The individual bars have lateral dimensions of 200 nm by 1 μm. b) An individual nanobar contacted for transport characterization.

tion 2.3. Here we suggest that an additional agent, i.e., lithographically induced strain relaxation, also plays a significant role in nano-patterned structures and is the only reasonable means by which to properly exercise *local* control of the anisotropy in (Ga,Mn)As. We demonstrate that patterning imposed relaxation effects can not only be observed in ferromagnetic (Ga,Mn)As but also that these effects can dominate the magnetic anisotropy in the entire temperature range, up to the Curie temperature  $T_c$ . Our findings pave the way to production of samples with *locally* designed anisotropy behavior.

## 6.1 Nanobars

A pair of nominally identical, high quality, 20 nm thick  $\text{Ga}_{0.96}\text{Mn}_{0.04}\text{As}$  layers grown on a GaAs substrate [Scho 03] with a  $T_c$  of 70 K are chosen for these studies. They are patterned into arrays of either [100] or [010] oriented nanobars for magnetic investigation and equivalent individual nanobars contacted for transport investigations. Fig. 6.1 shows SEM photographs of the above mentioned structures. The patterning was done by Silvia Hümpfner, who also developed the contacting process. Each individual bar has lateral dimensions of 200 nm by 1 μm. The full array of them is defined using electron beam lithography with a negative resist. After developing, the defined pattern is transferred into the (Ga,Mn)As layer using chemically assisted ion beam etching (CAIBE). As many as 8 million nanobars are laid out to provide sufficient total magnetization for the magnetic anisotropy studies carried out in the variable temperature superconducting quantum interference device (SQUID) magnetometer.



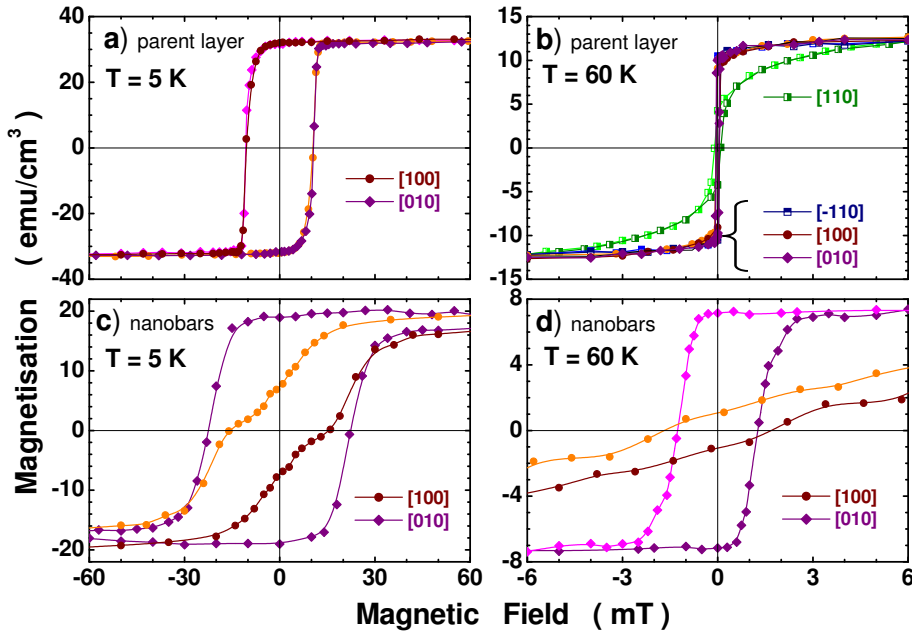


**Abb. 6.2:** SQUID magnetization data for a-b) the parent layer and c-d) the array of nanobars having their long side aligned to [010]. Light shades are used to mark the high resolution data obtained by numerical reflection to mimic the full hysteresis after confirming hysteretic symmetry with coarse measurements.

## 6.2 SQUID Investigations

The SQUID investigations on these nanobar arrays were done in collaboration with M. Sawicki from IFPAN, Warsaw. We investigate the magnetization  $m$  vs.  $H$  dependencies of the sample in applied magnetic fields of up to  $\pm 100$  mT for the four major in-plane orientations. All spurious background signals originating from the substrate and sample holders are subtracted from the data presented.

The salient features of the SQUID investigations are summarized in Fig. 6.2. We start with the unpatterned, "parent" layer (top panels) to show that, as is typical for (Ga,Mn)As, it exhibits equivalent behavior along [100] and [010], both at very low  $T$  (Fig. 6.2a), and near  $T_c$  (Fig. 6.2b). This is simply a manifestation of the fact that the presence of a  $\langle 110 \rangle$  uniaxial anisotropy, which bisects the four-fold  $\langle 100 \rangle$  easy directions and acts equivalently on [100] and [010] does not break the symmetry between these directions. The [010] uniaxial anisotropy is too weak to measurably break the symmetry here.

This behavior is in stark contrast to that of the patterned array, as shown in the bottom panels of Fig. 6.2, where magnetization studies of an array of nanobars oriented such that their long axis is along the [010] direction are presented. This axis is still a magnetic easy axis, similar to that of the host. The magnetic response along the [100] direction, which is along the short side of the nanobars has however been completely modified, and now exhibits pronounced hard axis behavior. From the hard axis measurements, we

estimate the lithographically imposed anisotropy field  $\mu_0 H_L$  produced by our sub-micron patterning to be 25 and 20 mT at 5 and 60 K, respectively. This field is comparable to the crystalline four-fold anisotropy field ( $\lesssim 100\text{mT}$ ) which dominates the behavior of the parent layer at 5 K, and is much larger than the  $\langle 110 \rangle$  uniaxial term ( $\sim 2\text{mT}$ ) which dominates the behaviour of the unpatterned layer at 60 K. For comparison, the shape anisotropy field is only 4 and 1.4 mT at these respective temperatures.

The overall magnetic anisotropy has thus been transformed from a strongly temperature dependent mixture of four-fold and uniaxial contributions into a well defined temperature independent uniaxial behavior imposed locally along the long axis of the nanobars. Arrays of nanobars patterned with their long axis along  $[100]$  give fully equivalent results.

The submicron dimensions of the nanobars have also allowed us to reach the single domain limit in (Ga,Mn)As at low temperatures. As seen in Fig. 6.2c, the magnetization reversal along the easy axis of the nanobars takes place roughly at the uniaxial anisotropy field of 25 mT, indicating a nearly fully coherent behavior of the magnetization inside the nanobar. The situation is more complicated at 60 K where, despite a 20-fold increase in the coercivity of the nanobars compared to the parent layer, the easy axis switch occurs at  $\sim 1.5$  mT, which is only a small fraction of the lithographically imposed anisotropy field of 20 mT at that temperature. The reason for this is that the equivalence of the  $\{[100], [010]\}$  and  $[\bar{1}10]$  anisotropy energy densities (Fig. 6.2b) observed in the parent layer at this temperature facilitates magnetization rotation along the nanobar, thus reducing their coercive field.

### 6.3 Transport Characterization

Having achieved the desired anisotropy control in the arrays, we now turn to electrical investigations, for which individual nanobars are prepared using similar lithography as in the patterning of the arrays. The major challenge in this case is a non-perturbative way of contacting the nanobar. This is non-trivial as it requires the formation of ohmic contacts onto (Ga,Mn)As with a  $\sim 100$  nm length scale. Moreover, our experience has shown that improperly optimized contacts do exert strain onto the layer, significantly altering its anisotropy [Goul 07]. We succeeded by using a Ti layer patterned by lift-off as a mask. After etching, the Ti mask is removed, and Ti/Au contacts are applied by e-beam lithography and lift-off. This yields contacts with a resistance-area product of below  $10^{-6}\Omega \cdot \text{cm}^2$ . In Fig. 6.3 we present transport characterization of two such nanobars patterned along the  $[100]$  and  $[010]$  directions on the same chip.

This sample is cooled in a variable temperature cryostat fitted with a vector field magnet, and its magnetoresistance behavior is measured for magnetic field applied along various angles  $\varphi$  ( $0^\circ$  along  $[010]$ ) in the plane of the layer. Prior to every scan, the sample is magnetized at -300 mT along  $\varphi$ .

The observed behavior (Fig. 6.3) is due to AMR, i.e. the fact, that the resistivity of a

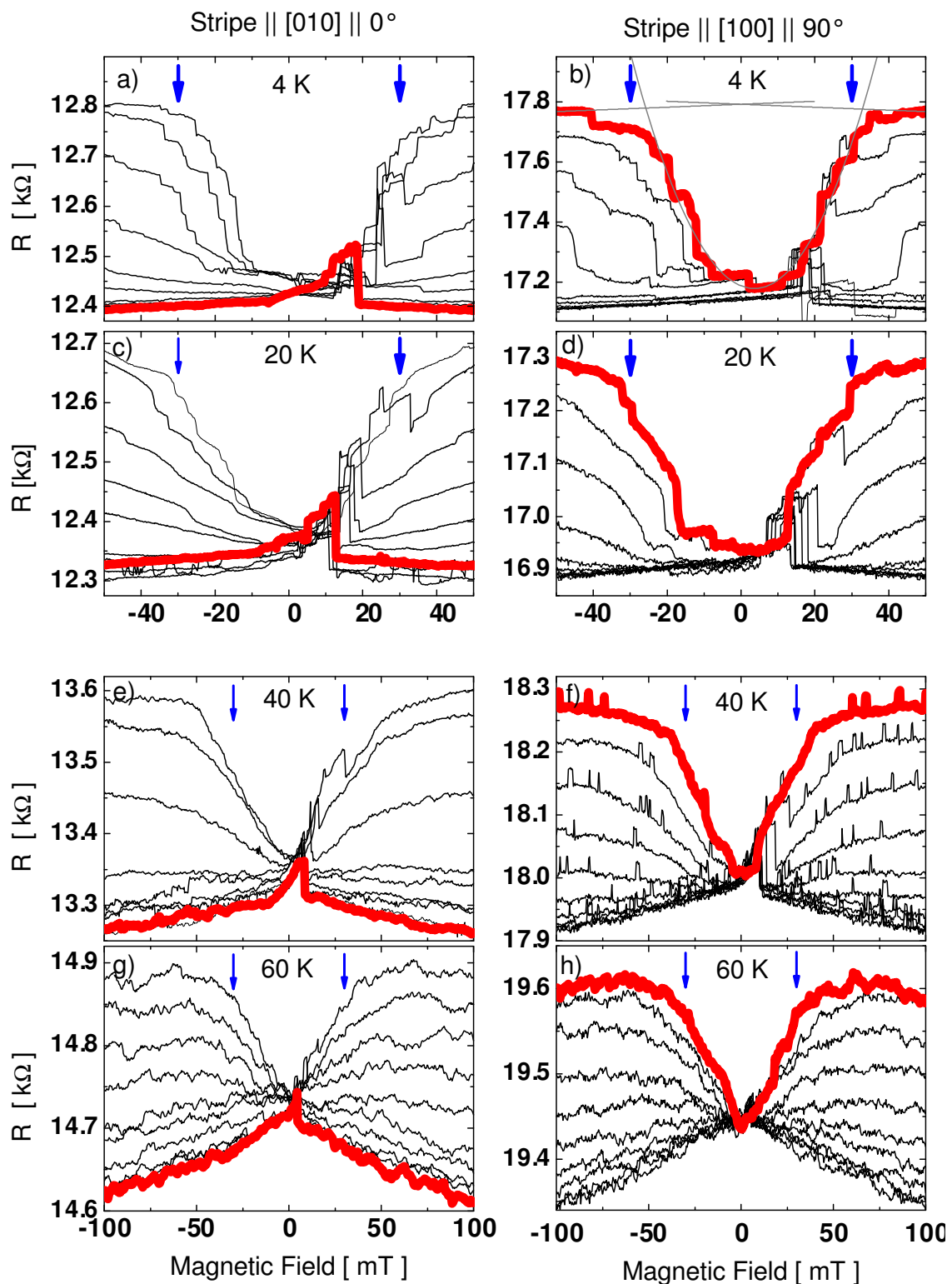


**Abb. 6.3:** Magnetoconductance scans for angles between  $0^\circ$  and  $90^\circ$  in  $10^\circ$  steps on the bars along  $[010]$  (left column) and  $[100]$  (right) at various temperatures and 5 mV bias voltage. The thick (red) line indicates the field sweep along the  $[010]$  crystal direction. The arrows indicate 30 mT an estimate for the uniaxial anisotropy field.

ferromagnetic material depends on the angle between the current and its magnetization as described in section 2.2.1. One can thus infer the angle  $\vartheta$  between magnetization and current from the resistance  $R$  at any field value through Eq. 2.2 and from the magnetization behavior deduce the magnetic anisotropy of the (Ga,Mn)As stripes. The left part of Fig. 6.3 presents MR scans on the nanobar along the [010] crystal direction at various temperatures, while the right column shows the same set of measurements on a [100]-oriented nanobar. All of the panels in Fig. 6.3 exhibit a striking resemblance to the calculated curves for a uniaxial magnetic anisotropy along the current direction in Fig. 3.12a. In the following we will first discuss the details of the measurements on the [010]-oriented nanobar in the left column of Fig. 6.3.

Thick red lines are the field sweeps along  $0^\circ$ , which is the long axis of the [010]-oriented nanobar. Obviously this is the current direction, which, by 'pattern recognition', was identified as the magnetic easy axis in the above paragraph. A detailed analysis of the individual curves confirms the latter. Magnetic field sweeps along  $0^\circ$  yield a low resistance curve at all temperatures, indicating, through Eq. 2.2 that  $M$  remains collinear with the current direction throughout the whole field sweep, as expected for a measurement along the uniaxial magnetic easy axis.

When the field is swept perpendicular to the nanobar (top black curve in each panel), the large values of the resistivity at high magnetic fields confirm that the magnetization is forced perpendicular to the bar. The resistance decreases monotonically as the field is swept down to zero, because the magnetization rotates towards the easy axis direction.

MR scans along other angles between  $0^\circ$  and  $90^\circ$  (in  $10^\circ$  steps) are also shown as black lines. In all these curves we observe the lowest resistance state at zero external field, confirming that the nanobar axis is the magnetic easy axis in the whole temperature range. The observed switching fields are consistent with the SQUID measurements. Finally, the linear back-ground is due to the isotropic magnetoresistance [Mats 04].

The right column of Fig. 6.3 presents results for the [100]-oriented nanobar. Since the coordinate system is fixed to the crystallographic axes, and not the axis of the nanobar, the fully opposite MR properties clearly indicate that the uniaxial behavior is related to the elongated shape of the nanobar. The thick red line, where the field was swept orthogonal to the nanobar (again along  $0^\circ$ ) is a typical hard axis magnetoresistance scan at all temperatures.

We conclude that the parent layer easy axis perpendicular to the wire has been overwritten by the patterning process and the lithographically imposed uniaxial anisotropy is the dominant anisotropy up to  $T_c$ , as was seen in the magnetization investigations in section 6.2.

Employing Eq. 2.2 allows us to assess the strength of this anisotropy. The hard axis MR-scan would be parabolic if only a pure uniaxial anisotropy was present and the field necessary to force the magnetization perpendicular to the easy axis a direct measure for the strength of the anisotropy (see section 3.2 and especially Eq. 3.9 for details). To estimate this anisotropy field, we fit a parabola [West 60] to the low field data of the

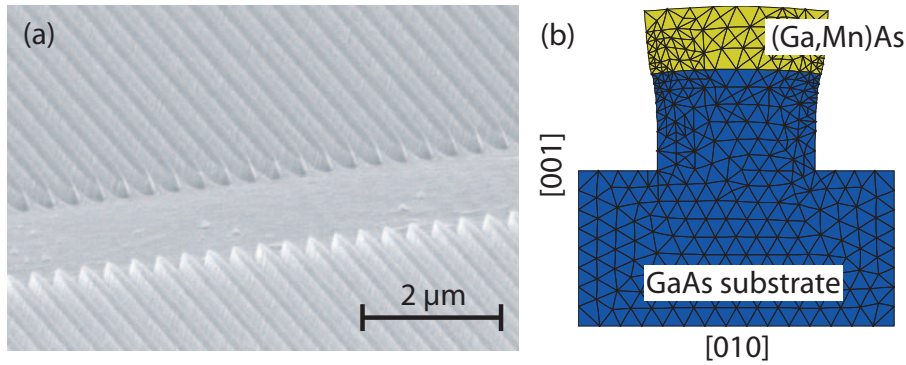


**Abb. 6.4:** *a) SEM image of 1 μm long and 200 nm wide (Ga,Mn)As stripes for X-ray investigations. b) Finite element simulation of the lattice displacement (100 times exaggerated) after strain relaxation in a cross-section of a 200 nm wide stripe by L. Ebel.*

perpendicular field scan in Fig. 6.3b and interpolate the isotropic magnetoresistance of this scan back to the origin (thin grey lines). Indeed, it can be shown mathematically, that an additional linear slope from the isotropic MR does not alter the validity of the parabolic fit for the extraction of the anisotropy field. The fitted parabola is slightly shifted towards positive fields, which indicates the presence of a small biaxial anisotropy contribution. The intersections between the grey lines and the parabola give  $\mu_0 H_a \sim 30$  mT. The same number (marked with blue arrows) is a reasonable estimate for the anisotropy field at all temperatures and for both nanobar orientations. This indicates that indeed the lithography induced uniaxial anisotropy is almost unchanged between 4 K and 60 K. The latter is a strong indication that the present effect is fundamentally different from classic shape anisotropy, which depends on the volume magnetization, and thus decreases with increasing temperature until it vanishes at  $T_c$ . Moreover, while size effects may play a role in the observed increase of the coercive field, they would play no role in modifying the anisotropy.

Obviously, the results presented here do not provide direct evidence of strain relaxation. Direct confirmation would require x-ray diffraction measurements which are not possible on the small structures investigated here. However, we have been able to verify that strain relaxation is the important agent in the effects reported here using X-ray diffraction measurements on long and narrow etched (Ga,Mn)As stripes [Weni 06, Weni 07].

## 6.4 Anisotropic Strain Relaxation

An SEM picture of such long stripes for X-ray investigations is shown in Fig. 6.4 along with a finite element simulation of the lattice displacement, that suggests the presence of anisotropic strain relaxation.

Transport measurements on an ensemble of circa 250 long stripes contacted in parallel are shown in Fig. 6.5a. The MR measurements along in-plane angles between  $0^\circ$  and  $90^\circ$  in

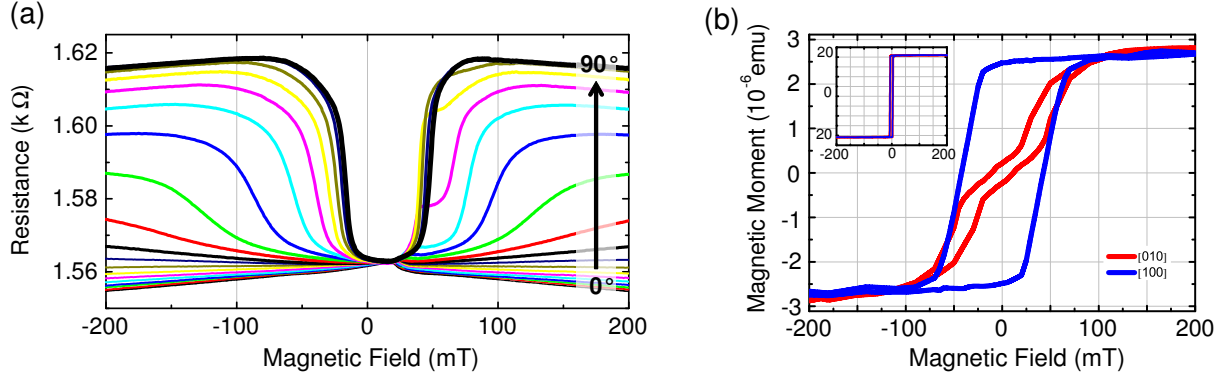


**Abb. 6.5:** a) Transport and b) SQUID confirmation of the dominating uniaxial magnetic anisotropy term induced by lithographic patterning in the long stripes of Fig. 6.4. The inset in b) shows the same SQUID measurements on the unpatterned (Ga,Mn)As parent layer for comparison.

10° steps clearly confirm that the dominating magnetic anisotropy component is uniaxial and has its easy axis along the bars (For a detailed discussion see sections 3.2 and 6.3). Note the very low noise level in this set of raw measurement data. The noise originating from individual Au contacts on (Ga,Mn)As is averaged out through the parallel contacting of many bars and the remaining noise level illustrates the impressive signal-to-noise ratio of the setup and the electronics used.

The uniaxial anisotropy of the long stripes is also confirmed by the SQUID measurements shown in Fig. 6.5b. Here the scan along the bar (blue) is clearly an easy axis loop and the red hysteresis loop perpendicular to the nanobar in the layer plane shows typical hard axis behaviour. Again, the parent layer anisotropy, where both these directions are equivalent magnetic easy axes (as shown in the inset of Fig. 6.5b, the two curves are identical on this scale) has obviously been overwritten by the patterning process. Additionally, as in the nanobars in the previous section, the coercivity in the stripes is tremendously increased compared with the unpatterned layer.

Fig. 6.6 shows the grazing incidence X-ray diffraction (GIXRD) studies on the stripes of Fig. 6.4. The experiments were performed by C. Kumpf at the Synchrotronstrahlungslabor in Hamburg, Germany (HASY-LAB). Here the strain relaxation in the (Ga,Mn)As stripes is determined from GIXRD reciprocal space mapping in the vicinity of the (333) Bragg reflection. Briefly, we are shown two slices of a three dimensional reciprocal space map. The right panel (b) shows the reciprocal space map for material with the GaAs reciprocal lattice constant in growth direction, 3.000 in this figure. The diffraction peak (yellow) is located at (333) - as expected both in-plane lattice constants are equal to the out-of-plane lattice constant in the GaAs substrate.

By mapping the reciprocal space at the out-of-plane lattice constant of the strained (Ga,Mn)As material at an  $l$ -position of 2.98, one is mainly sensitive to the (Ga,Mn)As stripes. This measurement is shown in Fig. 6.6a. The shift of the peak compared with

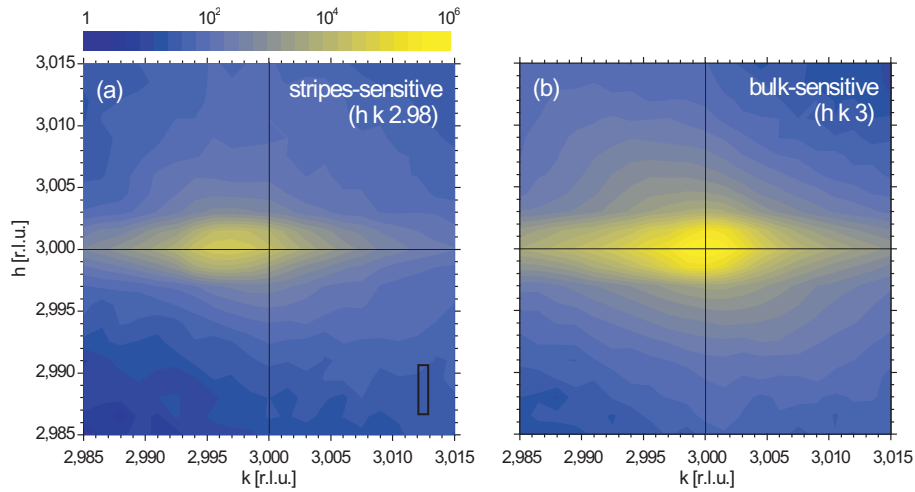


**Abb. 6.6:** *Anisotropic strain relaxation confirmed by grazing incidence X-ray diffraction (GIXRD) measurements on the sample of Fig. 6.4 by C. Kumpf.*

panel b) shows that, while the lattice constant along the stripes is unchanged, the lattice has relaxed perpendicular to the stripe direction.<sup>1</sup> More details on the GIXRD and other X-ray measurements are discussed in Ref. [Weni 07].

## 6.5 Strength of the Induced Anisotropy

The origin of the induced anisotropy was investigated in k.p calculations by M.J. Schmidt [Weni 07]. A calculation similar to the one in Sec. 5.2.3 can be used to determine the full energy of the hole system as a function of magnetization direction, which is equivalent to the energy landscape. The fully strained layer, of course, exhibits the typical biaxial magnetic anisotropy. Anisotropic strain relaxation can produce a pure uniaxial magnetic anisotropy if the layer is fully relaxed in one of the two easy axis directions and fully strained in the other. Intermediate strain conditions are expected to produce a mixture of the biaxial and uniaxial anisotropy terms.

Fig. 6.7a illustrates what effect differently weighted mixtures of the two anisotropy terms have on the energy landscape. The lowest curve shows the purely biaxial case. Adding a uniaxial anisotropy term with easy axis along  $0^\circ$  and amplitude  $K_{uni[010]} = 25\%K_{cryst}$  yields the red curve above. With increasing amplitude of the uniaxial term (in steps of 25%), the local energy minimum at  $90^\circ$  becomes shallower until it is finally flattened out at  $K_{uni[010]} = K_{cryst}$ .

We want to approximate the necessary uniaxial anisotropy term needed to create a

<sup>1</sup>The slight broadening of the peak in k direction in the bulk sensitive measurement in Fig. 6.6b stems from the fact that some of the GaAs material is of course also arranged in stripes. The amplitude of the broadened stripe signal is 1-2 orders of magnitude lower than the bulk signal, which gives the main peak. The impression of a broadened signal is thus mainly due to the logarithmic intensity scale.

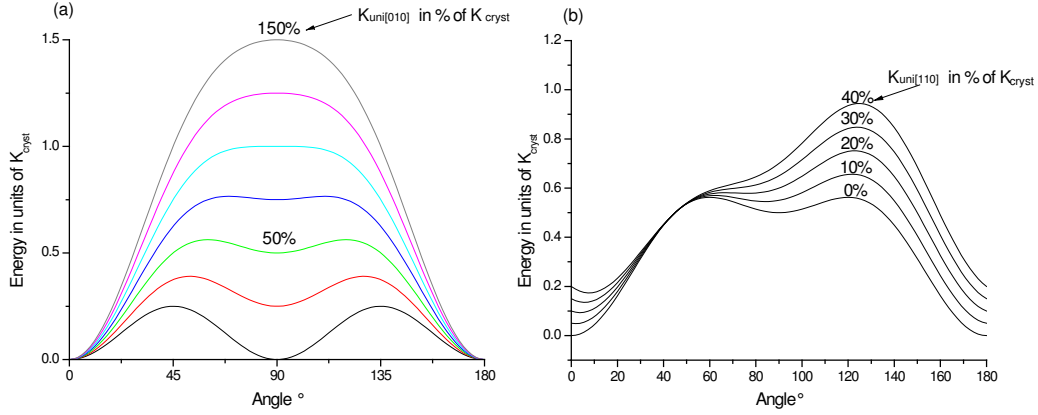


**Abb. 6.7:** a) Energy landscape of a mixed symmetry magnetic anisotropy including a biaxial term and a uniaxial term with easy axis along  $0^\circ$  with a strength of  $K_{uni[010]} = 0\%$  (bottom curve) to  $150\%$  (top) of the biaxial anisotropy. b) Influence of an additional anisotropy term with easy axis along the  $[\bar{1}10]$  crystal direction ( $45^\circ$ ) on the green curve ( $K_{uni[010]} = 50\% K_{cryst}$ ) of a).

mainly uniaxial anisotropy<sup>2</sup>, such as in the nanobars in Fig. 6.2 and 6.3. According to Fig. 6.7a a rather large uniaxial term at least of the order of the biaxial anisotropy strength would be needed. This is not true in practice, as can be seen from the approximated uniaxial anisotropy field of only 30 mT in Fig. 6.3. The two main reasons for the discrepancy between the results of Fig. 6.7a and the measurements are explained below.

Firstly, the interplay between anisotropic strain relaxation and crystalline anisotropy is not a simple superposition of energy terms as implied in the above discussion. Both anisotropy terms are coupled to the crystal lattice. One would thus expect that the crystalline anisotropy term is weakened by anisotropic strain relaxation. At the same time the lithographically imposed uniaxial term is created through this anisotropic strain relaxation. Additionally the simple sine-wave dependence of the energy terms may be altered because the anisotropic strain relaxation is stronger close to the edges of the nanobar compared with its center.

Secondly, a much more pronounced effect is expected from the additional  $[\bar{1}10]$  anisotropy component that is present in (Ga,Mn)As layers. As explained in Section 2.3, the initial layer anisotropy is more complex and not purely biaxial. The influence of the  $[\bar{1}10]$  anisotropy component is of major importance for the magnetization behaviour in this context. Fig. 6.7b illustrates the interplay of the three anisotropy terms. The lowest curve is the energy landscape for a biaxial magnetic anisotropy  $K_{cryst}$  term with a uniaxial anisotropy component with  $K_{uni[010]} = 50\% K_{cryst}$ , the same situation as in the green curve of Fig. 6.7a. Higher curves display the energy surface with increasing uniaxial anisotropy component  $K_{uni[\bar{1}10]}$  along the  $[\bar{1}10]$  crystal direction (with easy axis along  $45^\circ$ ),

<sup>2</sup>”Mainly uniaxial” is used here to describe an energy landscape, that has only two minima in an angular range of  $360^\circ$ .



the numbers give  $K_{uni[\bar{1}10]}$  in percent of the biaxial anisotropy constant  $K_{cryst}$ .

A  $[\bar{1}10]$  component between 10% and 20% of  $K_{cryst}$ , a typical value for as-grown (Ga,Mn)As, causes the local energy minimum at  $90^\circ$  to disappear, i.e. the  $[\bar{1}10]$  anisotropy component assists the lithographically induced anisotropy. Consequently structures show a mainly uniaxial behaviour with the magnetization in the remanent state aligned along the global uniaxial easy axis, defined by the global minimum of the energy surface, here close to  $0^\circ$ , i.e. the long direction of the stripes.

The patterning induced anisotropy in our nanobar structures in Fig. 6.1 can be calculated using Equ. 3.9 in combination with the estimated anisotropy field of 30 mT in Fig. 6.3 (note the method used underestimates the anisotropy field as will be explained later) and the magnetization  $M \sim 37000$  A/m known from SQUID measurements at 4 K. The biaxial magnetic anisotropy of the unpatterned parent layer on the other hand is typically  $3000$  J/m<sup>3</sup> at 4 K, confirmed by both SQUID and transport measurements along the hard magnetic ( $\langle 110 \rangle$ ) axis of our layer. We expect a weakening of this crystalline anisotropy term through anisotropic strain relaxation. For the purpose of this discussion the uniaxial anisotropy component along the  $[010]$  crystal direction is negligibly small and is simply included in  $K_{uni[010]}$ . The uniaxial anisotropy component along the  $[\bar{1}10]$  direction was measured with the help of the anisotropy fingerprint technique (chapter 3) yielding  $K_{uni[\bar{1}10]} \sim 15\%K_{cryst}$ . Assuming that the crystalline anisotropy is reduced to  $\sim 50\%$  of its original value and including the anisotropy constants given above yields the energy landscape depicted in Fig. 6.8a. Where the nanobar is oriented along  $90^\circ$ , the global energy minimum. The lithographically induced term in combination with the  $[\bar{1}10]$  uniaxial term from the parent layer are just strong enough to eliminate the local energy minimum perpendicular to the nanobar (along  $0^\circ$  and  $180^\circ$ ). As a result the energy terms sum up to a uniaxial energy landscape, which at zero field exhibits minima only along the nanobar direction.

Fig. 6.8b shows calculations of the expected AMR signal in a structure with the described mixed anisotropy ( $K_{uni} \sim 600$  J/m<sup>3</sup>,  $K_{uni[010]} = 50\%K_{cryst}$ ,  $K_{uni[\bar{1}10]} = 500$  J/m<sup>3</sup>). The resulting pattern closely resembles the transport measurements on our nanobars in Fig. 6.3. From this calculation it is obvious that an order of magnitude estimate of the uniaxial anisotropy field can be obtained by the parabola method as in Section 6.3. However, this method gives only a lower limit of the uniaxial anisotropy field. The shape of the curves is determined by both the biaxial and the uniaxial components and in the case of a relatively strong biaxial component, the method underestimates the anisotropy field strongly. In Fig. 6.8b one would for example determine an anisotropy field of only  $\sim 35\%$  of  $2K_{uni[010]}/M$  by the parabola method. We note in passing that other groups independently have reported behaviour consistent with the results discussed in this chapter [Wund 07].

In conclusion, we have demonstrated a reliable technique for comprehensively controlling the anisotropy locally in (Ga,Mn)As using a lithographic technique and showed that the observed strong uniaxial anisotropy is due to anisotropic strain relaxation. We believe

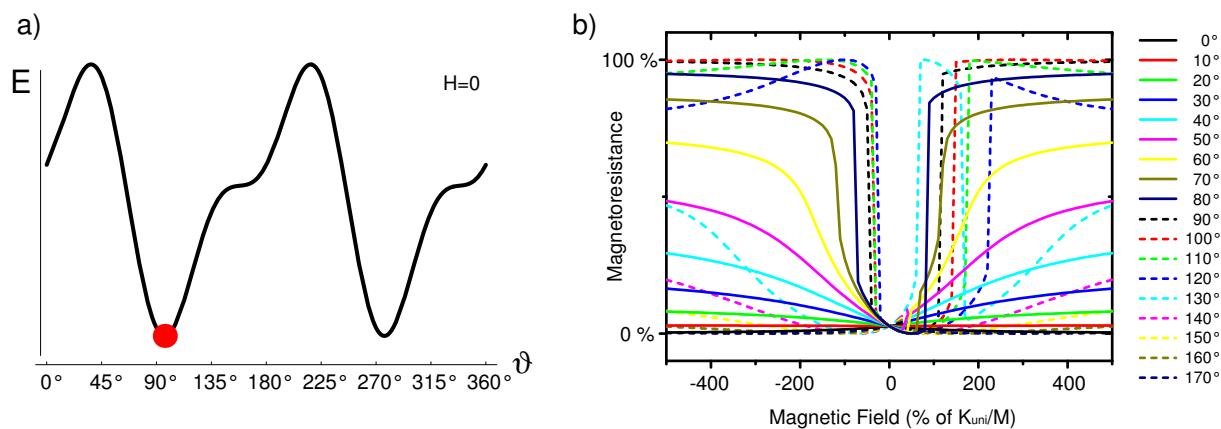


**Abb. 6.8:** a) Energy landscape for a mixed symmetry anisotropy typical for a nanobar ( $K_{uni[010]} = 50\%K_{cryst}$  and  $K_{uni[\bar{1}10]} = 500 \text{ J/m}^3$  and  $K_{uni} \sim 600 \text{ J/m}^3$ ) b) Calculated magnetoresistance behaviour for a nanobar with the energy landscape in a). The magnetic field units are in percent of the uniaxial anisotropy constant normalized to the saturation magnetization.

this will prove itself a useful tool for studying novel spintronics effects related to transport between regions of different anisotropies or unique magnetization configurations within a layer. The first device fabricated using this technique is discussed in the following chapter.

## Chapter 7

# Exploiting Locally Imposed Anisotropies in (Ga,Mn)As

The discussed lithographic anisotropy control greatly enhances the scope of possible device paradigms open to investigation as it allows for devices where the functional element involves transport between regions with different magnetic anisotropy properties. In this chapter we present the first such device, structured by Silvia Hümpfner. It is comprised of two (Ga,Mn)As nanobars, oriented perpendicular to each other (Fig. 7.1), and with each nanobar exhibiting strong uniaxial magnetic anisotropy. The two nanobars are electrically connected through a constriction whose resistance is determined by the relative magnetization states of the nanobars. We show that the anisotropic magnetoresistance effect is responsible for a difference in constriction resistances depending on the relative orientation of the two nanobar-magnetization vectors.

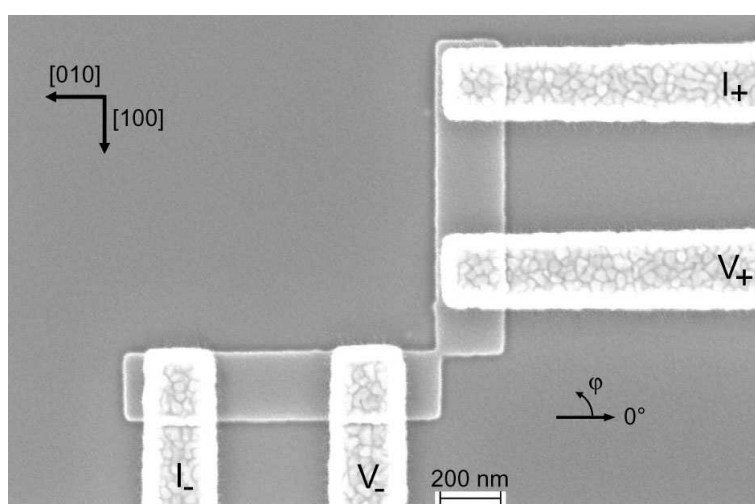


**Abb. 7.1:** SEM photograph of the device identifying the orientation of the nanobars with respect to the crystal directions, and the definition of the current ( $I_+, I_-$ ) and voltage ( $V_+, V_-$ ) leads and the writing angle  $\varphi$ .

The structure can be viewed as the basis of a ferromagnetic semiconductor memory device that operates in the non-volatile regime. It offers a new method of storing information in a magnetic semiconductor: namely saving it in the relative magnetization orientation of two orthogonal bars. The information read-out through the resistance of a depleted constriction offers a tuneable On/Off-resistance ratio. Values up to 280% have already been achieved. This number is expected to increase dramatically upon optimization. In combination with the advances on current induced domain wall motion in magnetic semiconductors [Yama 04, Goul 06] (chapter 4), the presented scheme constitutes a significant step towards an all electrical semiconductor memory architecture.

## 7.1 Device Operation

For the device, we use a 20 nm thick (Ga,Mn)As layer grown on a GaAs substrate [Scho 03] by low-temperature molecular beam epitaxy. Using an electron-beam lithography (EBL) defined Ti-mask and chemically assisted ion beam etching (CAIBE) this layer is patterned into several pairs of coupled nanobars (chapter 6) as shown in the SEM micrograph in Fig. 7.1. Ti/Au contacts are defined in another EBL-step through metal evaporation and lift-off, yielding resistance area products of  $\sim 1 \mu\Omega\text{cm}^2$ . The bars are circa 200 nm wide and 1  $\mu\text{m}$  long and oriented along the [100] and [010] crystal direction. They form a 90°-angle and touch each other in one corner, where a constriction with a width of some tens of nm is formed. In this chapter we show characteristics of two structures that are representative for the two limits of device behavior we have observed. Several other structures have been investigated, which all show qualitatively the same behaviour.

Transport measurements are carried out at 4 K in a magnetocryostat fitted with a vector field magnet that allows the application of a magnetic field of up to 300 mT in any direction with an angular resolution of better than 0.1°. The sample state is first "written" by an in-plane magnetic field of 300 mT along a writing angle  $\varphi$  (as defined in Fig. 7.1). The field is then slowly swept back to zero while ensuring that the magnetic field vector never deviates from the  $\varphi$ -direction. We measure the four-terminal resistance of the constriction in the resulting remanent state by applying a voltage  $V_b$  to the current leads ( $I_+$  and  $I_-$ ), and recording both the voltage drop between contacts  $V_+$  and  $V_-$  and the current that is flowing from  $I_+$  to  $I_-$  (Fig. 7.1). The polar plot of Fig. 7.2 shows the constriction resistance of the remanent magnetization state as a function of the writing angle  $\varphi$ . The resistance, which is dominated by the constriction, has a higher value upon writing the sample in the (extended) first quadrant ( $-3^\circ \leq \varphi < 98^\circ$ ) and a lower value upon writing in the (shrunk) second quadrant ( $98^\circ < \varphi < 167^\circ$ ). As a whole the plot is point-symmetric with respect to the origin.

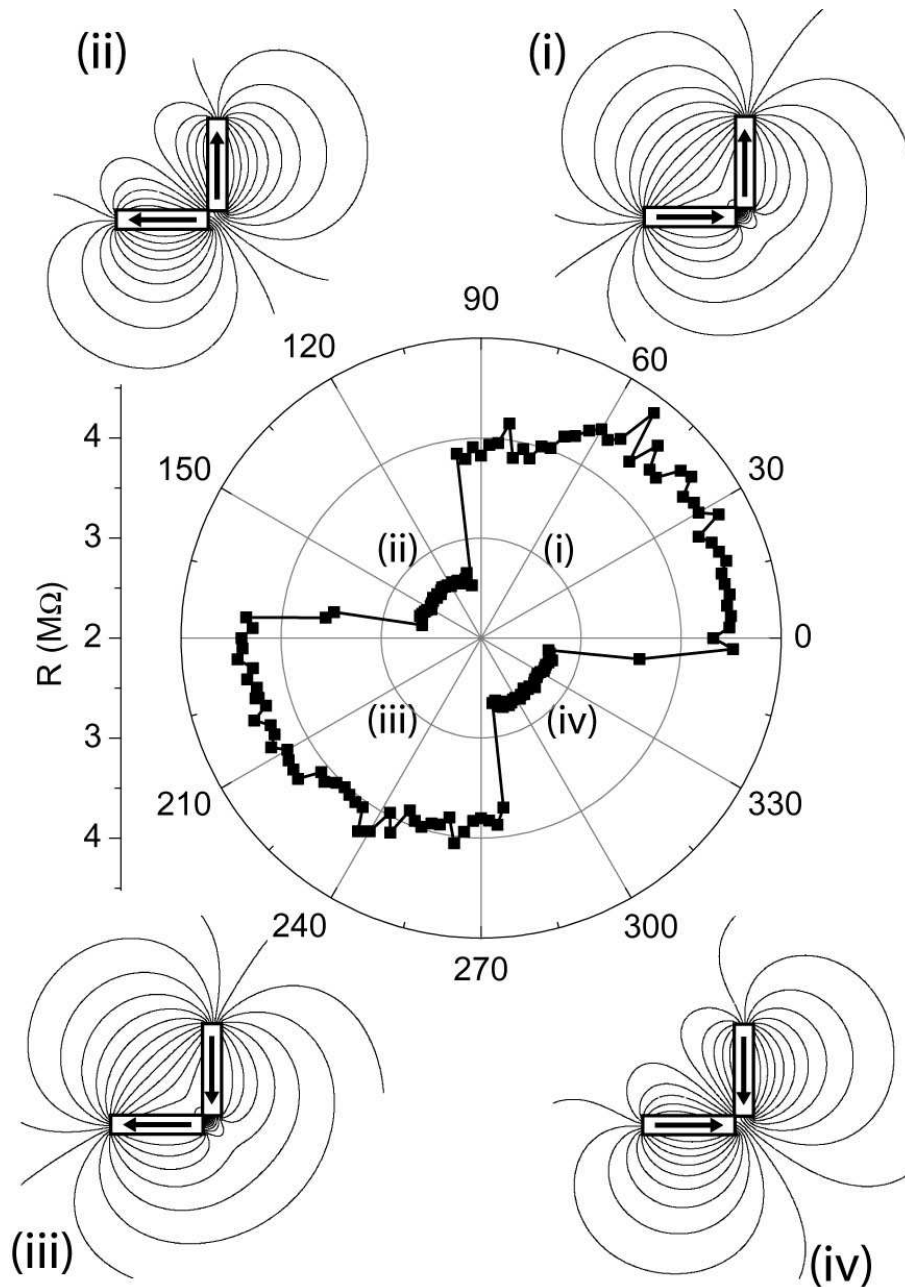


**Abb. 7.2:** Polar plot showing the results of a "write-read" experiment. The state of the device is written by applying a magnetic field of 300 mT in the  $\varphi$  direction. This field is then swept back to zero, and the resistance of the device is measured. The insets sketch the magnetic configuration of the device in each quadrant and the corresponding field line patterns[Vizi 07].

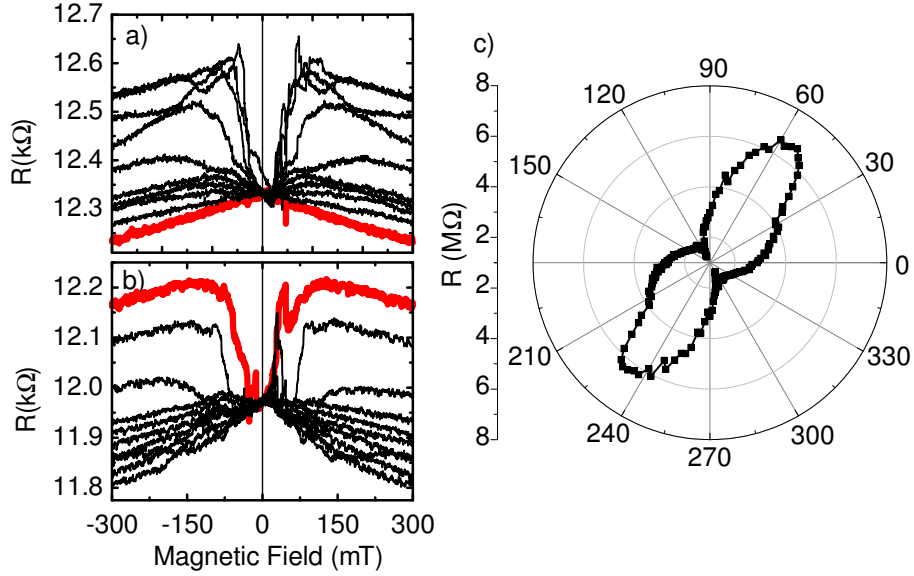


**Abb. 7.3:** Magnetoresistance measurements on the  $0^\circ$ (a) and  $90^\circ$ -nanobar(b) confirming that each exhibits a strong uniaxial magnetic anisotropy along its long axis. Field sweeps from -300 to 300 mT along  $0^\circ$ (thick line)... $90^\circ$  in  $10^\circ$  steps. c) Polar plot showing the resistance of the constriction in a field of 300 mT at various angles.

## 7.2 Magnetic States

To explain these results, we first examine the behavior of the individual nanobars. They are patterned on the sub-micron scale to make use of anisotropic strain relaxation, which in turn causes a uniaxial magnetic anisotropy that is strong enough to overwrite the intrinsic anisotropy of the (Ga,Mn)As layer (see chapter 6). We therefore expect each nanobar to show a uniaxial magnetic anisotropy with a magnetic easy axis along the respective long axis of each of the nanobars.

That our method for lithographically inducing uniaxial anisotropy also works for coupled nanobars is confirmed in Fig. 7.3, which shows two terminal magnetoresistance scans, performed separately on the  $0^\circ$ -nanobar (Fig. 7.3a) and the  $90^\circ$ -nanobar (Fig. 7.3b) pictured in Fig. 7.1, as shown in Fig. 6.3 for the individual nanobars. The plots show field sweeps from -300 to +300 mT for various in-plane field directions  $\varphi$  between  $0^\circ$  and  $90^\circ$ . As explained in Section 2.2.1 metallic (Ga,Mn)As exhibits a higher resistance value when the magnetization  $\mathbf{M}$  is perpendicular to the current  $\mathbf{J}$ , than when  $\mathbf{M}$  is parallel to  $\mathbf{J}$  (the AMR effect). When the field  $\mathbf{H}$  is swept along  $0^\circ$  (thick line in Fig. 7.3a), the resistance of the  $0^\circ$ -nanobar remains in the low state, indicating that  $\mathbf{M}$  is parallel to  $\mathbf{J}$  throughout the entire magnetic field range. All the other MR-scans start at a higher resistance value and merge into the low resistance curve at zero field, indicating that  $\mathbf{M}$ , which is almost parallel to  $\mathbf{H}$  at high fields, relaxes towards the  $0^\circ$  uniaxial easy axis as the field is decreased. Analogously, the uniaxial easy axis of the  $90^\circ$ -nanobar is along  $90^\circ$  (Fig. 7.3b). Consequently, the  $90^\circ$ -MR-scan is a flat low resistance curve. During the  $0^\circ$ -scan (thick

line) the magnetization relaxes from parallel to the field (high resistance) towards the easy axis along the bar (low resistance) at zero field.

Given that both bars show a uniaxial magnetic easy axis along their respective long axis, the structure has four possible magnetic states at zero magnetic field as sketched in Fig. 7.2. In sectors (i) and (iii) the nanobars are magnetized "in series", i.e. the magnetization vectors meet in a configuration which we will call *head-to-tail*. In (ii) and (iv) on the other hand, both magnetization vectors point away from (*tail-to-tail*) or towards (*head-to-head*) the constriction. When the sample is magnetized along a given direction at 300 mT, the magnetization of both bars is almost parallel to the magnetic field. As the field is then lowered to zero, the magnetization of each nanobar relaxes to the respective nanobar easy axis, selecting the direction which is closest to the writing angle  $\varphi$ . For a nanobar along  $0^\circ$  this means, assuming no interaction between the bars, that  $\mathbf{M}$  relaxes to  $0^\circ$  upon writing the bar along any angle between  $+90^\circ$  and  $-90^\circ$ ; otherwise  $\mathbf{M}$  relaxes to  $180^\circ$ . If the bars in our device were non-interacting, one would thus expect the magnetization configuration in each quadrant to be as depicted in the sketches of Fig. 7.2, with each quadrant accounting for exactly one fourth of the total plot.

The deviation from this behavior in the actual device is due to magnetostatic interactions between the two bars, which cause a preference for head-to-tail configurations. A simple magnetostatic calculation shows that the repulsive field felt by the tip of one bar due to being near the wrong pole of the other bar is of the order of 2 mT, which is  $\sim 5\%$  of the uniaxial anisotropy field. The energy density of this field is thus strong enough to overcome a small part of the energy barrier against rotation towards the opposite magnetization direction, which corresponds to an angle of  $\sim 3^\circ$ . The head-to-tail quadrants thus increase commensurably.

Magnetic field line patterns for the four magnetization configurations were calculated (sketches in Fig. 7.2i-iv) using a simple bar magnet model. The field lines are close to parallel to the current in the head-to-tail configuration (Fig. 7.2i and iii). In the tail-to-tail and the head-to-head configuration (Fig. 7.2ii and iv) the field lines are approximately perpendicular to the current.

### 7.3 Origin of the Resistance Signal

Having understood the magnetic configuration of the device in the write-read experiment of Fig. 7.2, we now turn to an explanation of why these should lead to two very distinct resistance states. The above magnetostatic arguments and internal fields, in connection with the AMR coefficient for metallic (Ga,Mn)As can explain a few percent resistance difference (see e.g. the transport measurements in chapter 6) between the head-to-tail and the head-to-head configuration, much smaller and of a different sign than the effect in Fig. 7.2. We have actually observed such a small AMR related effect in similar structures, which have a wider constriction (100 times lower constriction resistance). Fig. 7.4a

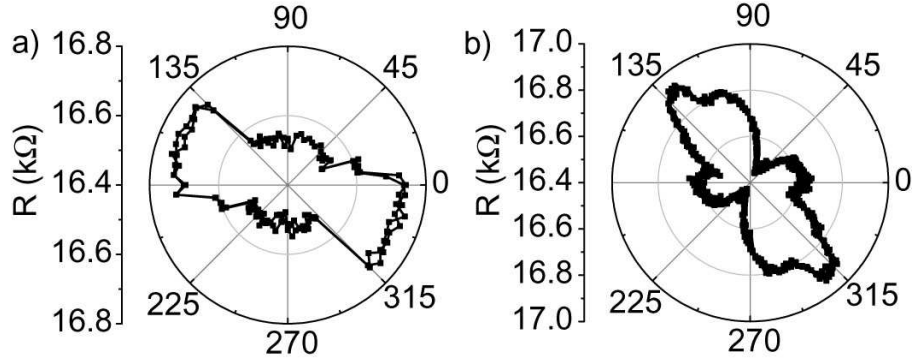


**Abb. 7.4:** (a) Results of a write-read experiment as in Fig. 7.2, for a device with a wider constriction, which exhibits metallic transport behavior and (b) constriction resistance in a rotating 300 mT external magnetic field.

shows similar data on a typical low resistance sample as Fig. 7.2 for a high resistance sample. It is immediately obvious from Fig. 7.4a that this sample shows the same remanent magnetization configurations as the device in Fig. 7.2, except for the slight rotation of the "quadrants" which is due to the stronger magnetostatic coupling between the bars. However, the effect is much smaller and of the opposite sign: where Fig. 7.2 exhibits a high resistance state, Fig. 7.4a shows a low state, and *vice versa*. A systematic summary of the AMR effect in other samples studied is contained in the supplementary information section. In the manuscript we limit ourselves to the discussion of two representative devices, one with high and one with low constriction resistance.

We ascribe the difference in behavior between Figs. 7.2a and 7.4a to the occurrence of depletion in the constriction in the sample of Fig. 7.2a, which drives the transport (in the critical constriction region) into the hopping regime (chapter 5). At the same time, we suggest that in the hopping regime the AMR coefficient *changes sign*, leading to the observed changes in magnetoresistance. Important evidence for this claim comes from the angle-dependent magnetoresistance behavior of the samples at a field of 300 mT, strong enough to force the magnetization close to parallel to the external field. This data is given in Fig. 7.3c for the high-resistance, and in Fig. 7.4b for the low-resistance sample.

The low-resistance device exhibits typical AMR behavior as expected for metallic (Ga,Mn)As: Fig. 7.4b shows that the resistance is lowest when  $\mathbf{M}$  is forced parallel to the current through the constriction ( $\varphi \sim 45^\circ$ ) and ca. 3 % higher for  $\mathbf{M} \perp \mathbf{J}$ . In contrast, the high-resistance constriction of the device in Fig. 7.2 shows a huge and inverted AMR signal, as can be seen in Fig. 7.3c. The resistance at  $\varphi \sim 45^\circ$ , where  $\mathbf{M} \parallel \mathbf{J}$ , is more than 5 times larger than for  $\mathbf{M} \perp \mathbf{J}$ .

This is actually not the first observation of an inverted AMR signal; the same effect has recently been reported in thin (Ga,Mn)As devices [Wund 06, Rush 06] in which the transport is in the hopping regime. This situation is similar to our high-resistance device, where from the resistance one already can infer that the constriction is partially depleted.



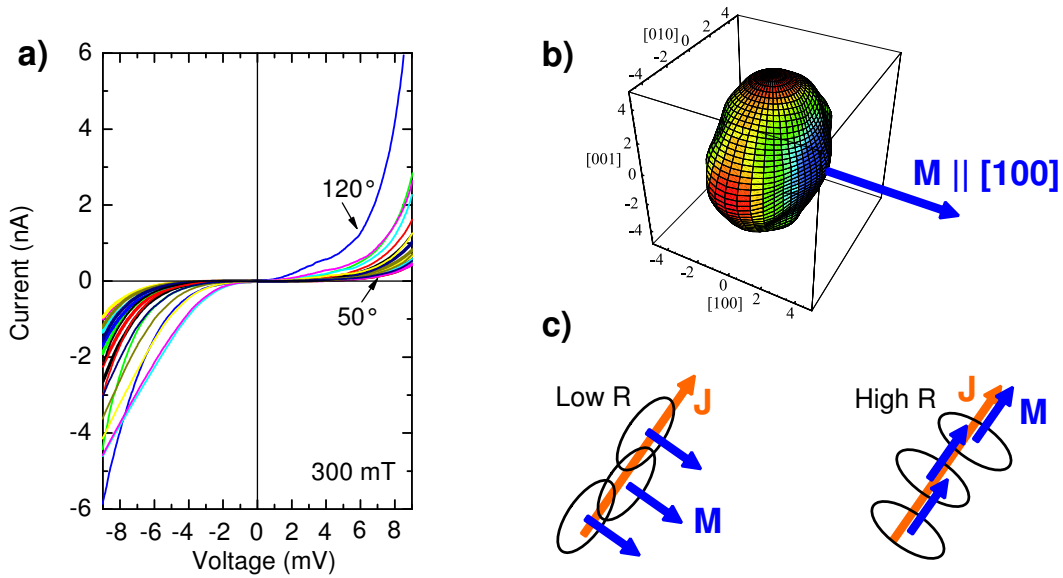


**Abb. 7.5:** Magnetization direction dependent hopping transport. a) The non-linearity of the current-voltage characteristic at 300 mT changes with the magnetic field angle. b) Extend of the bound hole wave function for the magnetization collinear with the [100] crystal direction, calculated by M. J. Schmidt [Schm 07]. c) Illustration of the magnetization direction dependence of the hopping resistance.

Evidence for hopping transport comes from the current-voltage characteristics of the high-resistance constriction, shown in Fig. 7.5, which were taken at 300 mT at different field directions  $\varphi$ . The I-V's are clearly non-linear, with the nonlinearity depending on the magnetization direction. Fields aligning  $\mathbf{M}$  along  $\sim 120^\circ$  cause the strongest and along  $50^\circ$  the smallest non-linearity of the IV-curve.

The strong dependence of the IV-characteristic and the resistance on the magnetization direction are characteristic of transport going through a metal-insulator transition (MIT) from the diffusive into the hopping regime depending on the angle of the magnetization. Such a MIT has previously been observed in a TAMR device (chapter 5) and occurs in partly depleted samples due to the wave-function geometry change depending on the magnetization direction. The localized hole wave-function has an oblate shape with the smaller axis pointing in the magnetization direction. A visualization of the wave function extend, when the magnetization is aligned with the [100] magnetic easy axis was calculated by M. J. Schmidt and is displayed in Fig. 7.5b [Schm 07]. If the magnetization is aligned with the second in-plane easy axis (the [010] crystal direction) the wave function has a similar shape, but rotated by  $90^\circ$ . The short axis is again aligned with the magnetization direction.

Consider the overlap of such oblate shapes statistically distributed with respect to the direction of the current in connection with the Thouless localization criterion. In Fig. 7.5c, we sketch a top view of the individual bound hole wave functions in the depleted constriction region. Each wave function's extent is depicted as an ellipse. The wave

function overlap is much smaller when the sample is magnetized parallel to the current (right sketch in Fig. 7.5c), than for  $\mathbf{M} \perp \mathbf{J}$  (left sketch). A small overlap suppresses hopping transport through the depleted constriction and causes a high constriction resistance if the magnetization is oriented parallel to the current. This implies a magnetoresistance behavior that is exactly the inverse of that expected for the metallic regime and explains the increased resistance value in both the high field measurements (Fig. 7.3c along  $\sim 45^\circ$ ) and the write-read experiment (Fig. 7.2, 1st quadrant).

We thus believe that our observations can be fully explained by the internal magnetic fields and the AMR coefficient as applicable to the transport regime in the constriction. A further candidate to explain our observations could be the presence of a domain wall (DW) between differently magnetized regions of the device in the head-to-head and tail-to-tail configuration, which would be absent in the head-to-tail configurations. However, given the dimensions of the constriction the DW would not be strongly geometrically confined and one anticipates only a very low DW resistance in these samples [Rust 03, Brun 99]. This is confirmed by a comparison of Fig. 7.2 with Fig. 7.3c: The resistance values of both remanent states in Fig. 7.2 are in between the extreme resistance values of the homogeneously magnetized sample. The DW contribution [Rust 03] to the constriction resistance can in the present sample thus only be a minor effect on the resistance of the remanent state and does not explain the different resistance levels in Fig. 7.2. Note also that the resistance of the head-to-head configuration, including a possible DW contribution, is lower than the resistance of the head-to-tail configuration. We can thus exclude the DW as the origin of the two remanent resistance states observed in Fig. 7.2.

## 7.4 Domain Wall Manipulation

To further verify that the experiments described so far do not exhibit a DW effect, we have designed an experiment that would actually bring us in this limit. In this experiment, we have, using well defined field sequences described in detail below, prepared a DW pinned at the smallest part of our depleted constriction (as shown in Fig. 7.6). In this case we observe a large positive DW contribution to the device resistance (as reported in [Rust 03]). Fig. 7.6a shows magnetoresistance (MR) measurements along  $0^\circ$  (red curve) and along the two symmetric <sup>1</sup> directions  $45^\circ$  (green/top curve) and  $135^\circ$  (black/bottom curve) for the same sample as in Figs. 7.2, 7.3 and 7.5. In the following we show, that the peak resistance of the  $0^\circ$ -scan is related to a DW being pushed through the constriction region. Note that its resistance is much higher, than the maximum resistance measured for a homogeneous magnetization distribution (compare the high field measurements in Fig. 7.3c).

The MR curves can be explained taking into account the large inverse AMR signal in the depleted constriction. At high negative fields the magnetization in both bars and

---

<sup>1</sup>We call the  $45^\circ$  and  $135^\circ$  field directions symmetric which treat the two bars equivalently.

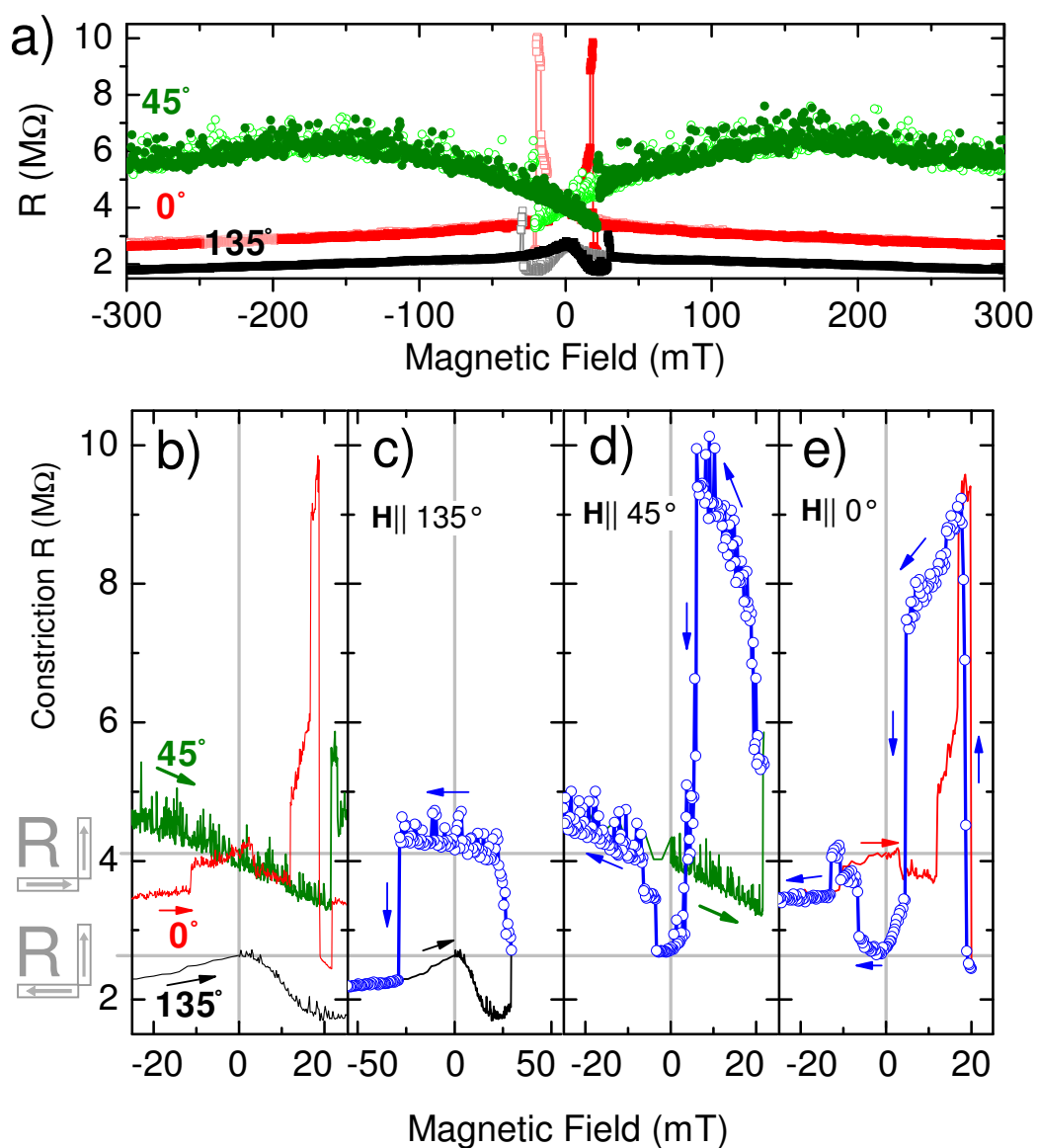


**Abb. 7.6:** Domain wall manipulation. a) Constriction resistance during hysteretic magnetic field sweeps along  $0^\circ$  (red),  $45^\circ$  (green) and  $135^\circ$  (black) and b) close-up of the up-sweeps. c)-e) The sweep (along  $135^\circ$ ,  $45^\circ$  or  $0^\circ$ ) is reversed (blue open circles) after flipping one nanobars' magnetization vector, resulting in a high domain wall related resistance (in d and e) and the opposite resistance state at 0 T.

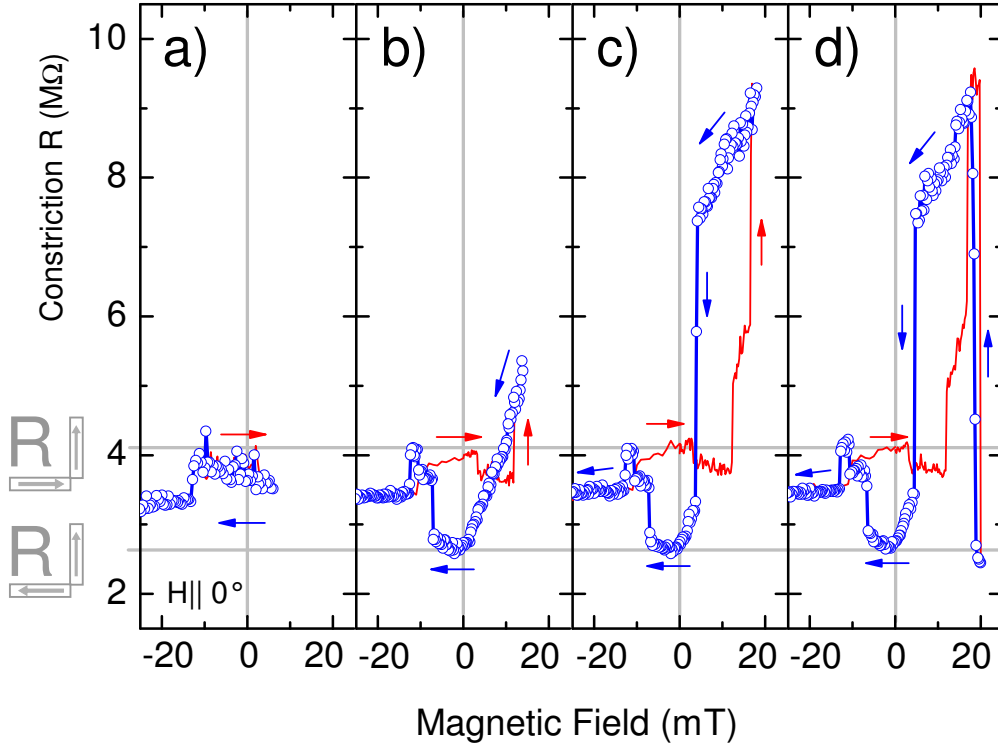


**Abb. 7.7:** Minor loops showing the constriction resistance during magnetic field sweeps along  $0^\circ$ . The sweep direction is reversed at a) 6 mT, b) 14 mT, c) 18 mT and in d) at 20 mT.

the constriction is aligned with the magnetic field vector. The constriction resistance is thus large along  $45^\circ$  almost parallel to the current and low along  $135^\circ$  circa perpendicular to the current, it takes an intermediate value along  $0^\circ$  (as shown in Fig. 7.3c). As the external field is reduced, the magnetization relaxes into the remanent configurations of Fig. 7.2. Finally, at small positive fields, one and shortly thereafter the second nanobar reverses its magnetization (See Fig. 7.6b for a close-up of the central region of Fig. 7.6a). Curves with open symbols in Fig. 7.6a show the hysteretically symmetric back sweep.

Panels (c) to (e) illustrate how the DW can be manipulated in magnetic minor loops. In panel (c) we sweep the field along  $135^\circ$  (black line). The device is in the tail-to-tail configuration at zero field corresponding to the low resistance state. At 29 mT the magnetization of one nanobar flips causing an abrupt increase in resistance. At this point the direction of the field sweep is reversed (blue open circles), where we measure the high resistance level at zero field. This is expected from the fact that only one nanobar was switched, i.e. the configuration changed from tail-to-tail to head-to-tail. This same nanobar magnetization flips back at -29 mT, restoring the initial situation.

A similar measurement along  $45^\circ$  is shown in Fig. 7.6d. The zero field state on the up-sweep (green) corresponds to the head-to-tail configuration which does not contain a DW. A sharp resistance increase at 22 mT marks the reversal of one nanobars' magnetization, which in this case introduces a DW into the constriction. The down-sweep (blue

open circles) shows a high resistance, where the DW is squeezed through the constriction before the low resistance remanent state is reached, again confirming that only one of the nanobars' magnetizations has flipped.

Sweeping the field along  $0^\circ$  parallel to one of the nanobars (Fig. 7.6e) causes very different switching fields for the two bars. As a result we measure the large resistance related to the DW already in the up sweep (red). We start with identifying the individual features of this sweep by investigating the minor loops shown in Fig. 7.7. The magnetic field is swept along  $0^\circ$  from -300 mT to a certain field value, after which the sweep direction is reversed. As above, we measure the four-terminal constriction resistance at all times. In Fig. 7.7a the sweep direction is reversed at 6 mT. The red line shows the up-sweep (negative to positive fields) and the blue curve with open circles the down-sweep. Both scans are identical within experimental error, no hysteretic features were observed. This confirms that no irreversible change of the magnetic configuration happens at fields below 6 mT. Fig. 7.7b shows a similar sweep, reversed at 14 mT, after the first abrupt resistance increase at 12 mT. The remanent magnetization state on the back sweep corresponds to the low resistance state. We can thus identify the abrupt resistance increase at 12 mT with one of the nanobars reversing its magnetization direction. A rapid resistance increase towards the high resistance state marks the magnetic field (-7 mT) where this magnetization flips back to its initial direction.

Reversing the magnetization of one nanobar means, changing the magnetization orientation of one of the bars in the Head-to-Tail configuration. This introduces a DW which is then pushed through the constriction causing the large resistance increase seen in Fig. 7.7c around 17 mT. The scan direction is reversed on the peak at 18 mT. When reducing the field strength, the DW is released and the resistance decreases, reaching the low resistance state at zero field. The remanent magnetization configuration on the back sweep is thus still the same as in Fig. 7.7c, the magnetization orientations of the nanobars are unchanged.

Fig. 7.7d shows that the high resistance connected to the DW being confined in the constriction, decreases rapidly (around 19 mT) when the DW is released from the narrowest point of the constriction. We reverse the sweep at 20 mT (in the dip of the red MR curve in Fig. 7.6b). The DW is squeezed back through the constriction yielding a large resistance, before the low resistance state at zero field is reached. This confirms that only one of the bars was switched during the whole procedure. If the original up-sweep is continued the second nanobar switches just above 20 mT. Reversing the sweep direction after this event produces a hysteretic curve as shown in light red in Fig. 7.6a. The large positive resistance in Fig. 7.6 and Fig. 7.7 thus obviously relates to a DW being pushed through a narrow constriction region by the increasing magnetic field. This DW is clearly released at zero field and consequently has only a negligible impact on the resistance of the non-volatile states.

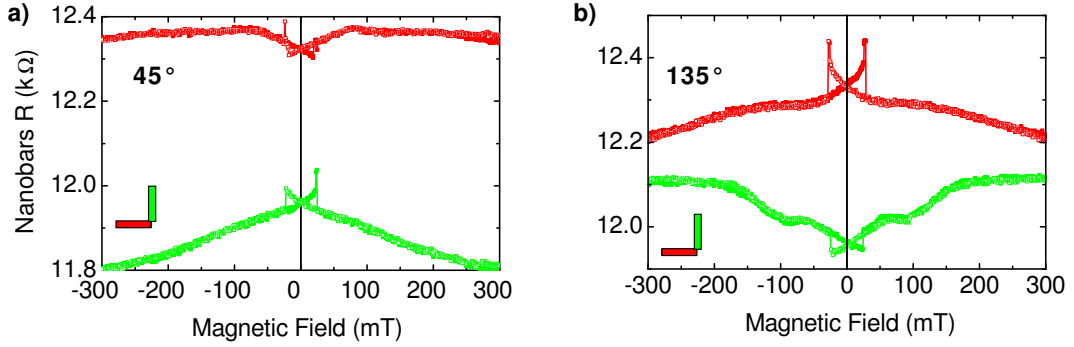


**Abb. 7.8:** Hysteretic magnetoresistance measurements on both nanobars taken during MR measurements of the constriction as in Fig. 7.6a. The field is swept along the symmetric directions (see text)  $45^\circ$ (left) and  $135^\circ$ (right).

## 7.5 Detailed Magnetoresistance Measurements

In this section we will discuss details of the magnetoresistance measurements, demonstrating the consistency and applicability of the explanations given above.

Apart from the minor loop method of section 7.4, one can identify features in the constriction magnetoresistance, by monitoring both nanobars' resistance at the same time. An example is illustrated in Fig. 7.8. It shows the resistance of the nanobar along  $0^\circ$  (red/top curve) and the nanobar along  $90^\circ$  (green/bottom curve) during magnetoresistance measurements with the field along  $45^\circ$  (left) and  $135^\circ$  (right). Each curve shows the three-terminal resistance<sup>2</sup> of one nanobar while the field is swept from  $-300$  mT to  $+300$  mT (filled symbols) and back (open symbols). The sharp feature occurs when the magnetization of this respective nanobar is flipped. The magnetization direction changes by almost  $180^\circ$  in this event. This has almost no impact on the AMR signal since the angle between current and magnetization is nearly unchanged. The feature seen in Fig. 7.8 is mainly due to the isotropic MR effect, which depends on the absolute value of the induction  $\mathbf{B}$ . The flipping magnetization  $\mathbf{M}$  changes  $\mathbf{B}$  by  $2\mathbf{M}$ , which in turn causes an abrupt resistance change. We can now compare the switching fields with the corresponding four-terminal constriction resistance measurements in Fig. 7.6a and confirm that the abrupt resistance changes in the  $45^\circ$  and  $135^\circ$  MR curve are related to the fact that the magnetization of the nanobars flips at the respective fields. Fig. 7.8 also confirms that the switching fields of the two bars are very similar as expected for the symmetric field directions  $45^\circ$  and  $135^\circ$ .

Fig. 7.9 shows the behaviour of the DW-related resistance as a function of the field angle. Shown are magnetoresistance measurements of the constriction region as in Fig. 7.6a

<sup>2</sup>In this measurement, the current flows from  $I_-$  to  $I_+$  (as defined in Fig. 7.1) and the voltage is measured on all contact pairs during the magnetic field sweep. The three terminal resistance of the nanobar along  $0^\circ$  is then given by the voltage measured between  $I_-$  and  $V_-$  divided by the current. The three terminal resistance of the other nanobar analogously by  $V(V_+-I_+)/I$ .

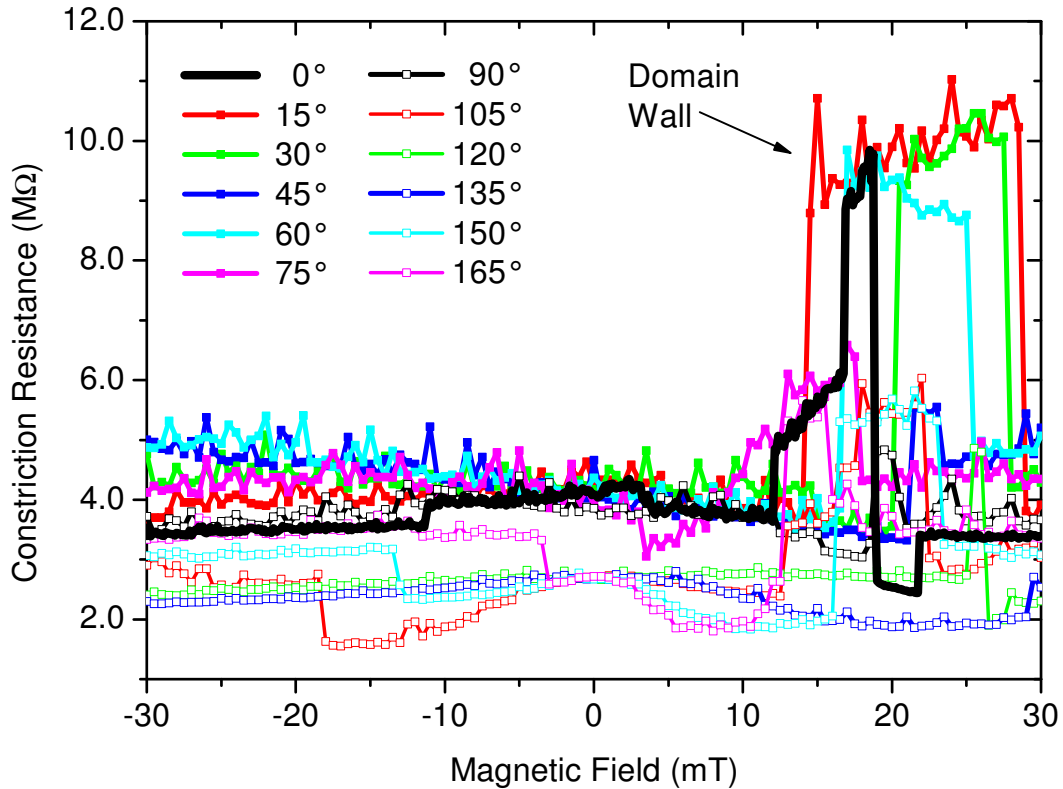


**Abb. 7.9:** High resolution magnetoresistance measurements on the high resistance constriction of Figs. 7.2 along many in-plane directions  $\varphi$ .

and b. The four-terminal resistance of the constriction is measured while the magnetic field is swept from -300 mT to 30 mT and only the low field part of each curve is displayed. The thick black curve is the sweep along  $0^\circ$  that was analyzed in detail in Fig. 7.7. Measurements along every  $15^\circ$  in the first quadrant are marked with filled symbols and measurements in the second quadrant with open symbols. As discussed above, the curves segregate into two groups at zero field, corresponding to the remanent states depicted in the insets of Fig. 7.2. All first quadrant curves show the high resistance state at zero field. This state is the magnetostatically preferred configuration and is therefore also assumed by measurements at the 'edges' of the first quadrant, along  $0^\circ$  and  $90^\circ$  (black open symbols) (see section 7.2 for details). Magnetoresistance measurements in the second quadrant, on the other hand, cause either the head-to-head or the tail-to-tail magnetization configuration at zero field, both connected to the low resistance state.

The large feature between 15 and 30 mT was identified in section 7.4 as resistance that is related to a confined DW in the constriction region. This is confirmed by the measurements in Fig. 7.9. The feature occurs only in scans that yield a head-to-tail configuration on the up-sweep which does not contain a DW at zero field. When the magnetization of one nanobar is flipped by the external magnetic field, a DW is introduced and pushed through the narrowest point of the constriction. Here the resistance increases rapidly to

a value much higher than  $\sim 6 \text{ M}\Omega$ , the maximum resistance for a homogeneous magnetization distribution (Fig. 7.3c), because of geometrical confinement [Rust 03, Brun 99]. The width of the feature of course depends on the detail of the DW moving through the constriction and is thus angle-dependent. The resistance value is however mainly defined by the geometry and the impurity configuration in the constriction and is thus similar in all the shown curves.

## 7.6 A Non-volatile Memory Cell

In conclusion we have shown that locally imposed magnetic anisotropies in different regions of one ferromagnetic semiconductor device allow for novel device designs. The orthogonally magnetized nanobars discussed in this chapter are a first demonstration of the type of devices that can be fabricated using this approach. We have shown that this device exhibits two stable magnetization states, defined by the relative orientation of the two bars, and which can be used for non-volatile information storage. Measuring the constriction resistance allows for the electrical read-out of the magnetic state. We emphasized that the corresponding on/off-resistance ratio can be amplified by several orders of magnitude using a partly depleted constriction and explained the physical origin of this effect. In this respect we highlighted the difference in AMR behavior between metallic and hopping transport in (Ga,Mn)As, which again should prove useful in future device design. The described mechanism has the potential to be integrated with current induced magnetization manipulation, from both device design and dimensions perspective. This would yield an all electrical semiconductor memory cell.



# Chapter 8

## Conclusions and Outlook

Magnetotransport measurements in general and the anisotropy fingerprint technique in particular allow the measurement of the (Ga,Mn)As magnetic anisotropy at 4 K. This method identifies the three major symmetry components present in all layers and unveils the evolution of the (Ga,Mn)As anisotropy with temperature.

These anisotropy studies laid the ground work for the demonstration of anisotropy engineering through anisotropic strain relaxation in submicron structures (nanobars). This method allows for the first time *local* engineering of the magnetic properties of (Ga,Mn)As structures, and this in the full temperature range up to  $T_C$ . It is now possible to study devices consisting of components with different engineered magnetic anisotropy.

A first such device is presented, showing that the, now possible, different relative magnetization orientations of the individual components yield different resistance states at the connection point of two nanobars (the constriction). The device exhibits two readable non-volatile states. Writing the information requires, at present, an in-plane magnetic field applied at a certain angle. However, current assisted magnetization writing has been demonstrated in a similar structure at 4 K. We are thus optimistic that an electrical writing scheme can be incorporated into a device design similar to our non-volatile device. This would yield an all-electrical all-semiconductor memory cell. In addition to the apparent technological potential of lithographic anisotropy control, it also allows for novel sample designs to study more fundamental physics, such as the resistance connected to the geometrical confinement of a domain wall or possibly the spin-transport between sources of orthogonal spin orientation.

New and exciting physics is also at work in depleted ferromagnetic semiconductors. A metal to insulator transition driven by the magnetic field direction is observed in both a TAMR device with partly depleted (Ga,Mn)As injector layer and in a coupled-nanobar device with partly depleted constriction. In both cases the effect can be explained by the magnetization direction dependent anisotropic extend of the hole wave function that is bound to a Mn impurity. The wave function overlap consequently depends on the magnetization direction and we can, by rotating the magnetization, drive the material from the metallic into the insulating state and back. The current flow in the insulating

state can be very small compared to the metallic state, yielding extremely high on/off ratios for the resistance read out signal. However, even in the on-state, the resistance is typically rather high if part of the device is depleted to the extent that it is close to the MIT. That is usually a drawback and further improvement on this point would strongly increase the technological relevance. Further research on engineering the resistance and the amplitude of the effect, as well as on a method for the intentional depletion of specific material regions would also be useful to investigate the effect in more detail. Specifically for the current in-plane geometry, further investigations are needed to clarify the crystal- and current-direction dependence and to understand the relation to other effects that have been reported in thin and/or inhomogeneous (Ga,Mn)As layers as discussed in [Rush 06, Wund 06].

# Bibliography

- [Abol 01] M. Abolfath, T. Jungwirth, J. Brum, and A. MacDonald. *Phys. Rev. B*, Vol. 63, p. 054418, 2001.
- [Ahar 88] A. Aharoni. *J. Appl. Phys.*, Vol. 63, p. 5879, 1988.
- [Ahar 98] A. Aharoni. *J. Appl. Phys.*, Vol. 83, p. 3432, 1998.
- [Aker 05] J. Åkerman. *Science*, Vol. 308, p. 508, 2005.
- [Allw 05] D. A. Allwood, G. Xiong, C. C. Faulkner, D. Atkinson, D. Petit, and R. P. Cowburn. *Science*, Vol. 309, p. 1688, 2005.
- [Alts 79] B. Altshuler and A. Aronov. *Sov. Phys. JETP*, Vol. 50, p. 968, 1979.
- [Awsc 07] D. D. Awschalom and M. E. Flatté. *Nature Physics*, Vol. 3, p. 153, 2007.
- [Baxt 02] D. V. Baxter, D. Ruzmetov, J. Scherschligt, Y. Sasaki, X. Liu, J. K. Furdyna, and C. H. Mielke. *Phys. Rev. B*, Vol. 65, p. 212407, 2002.
- [Berg 00] L. Berger, F. Albert, J. Katine, R. Buhrman, and D. Ralph. *Appl. Phys. Lett.*, Vol. 77, p. 3809, 2000.
- [Brow 68] W. Brown. *J. Appl. Phys.*, Vol. 39, p. 993, 1968.
- [Brun 99] P. Bruno. *Phys. Rev. Lett.*, Vol. 83, p. 2425, 1999.
- [Chap 07] C. Chappert. private communications 2007.
- [Chib 04] D. Chiba, Y. Sato, T. Kita, F. Matsukura, and H. Ohno. *Phys. Rev. Lett.*, Vol. 93, p. 216 602, 2004.
- [Cowb 95] R. Cowburn, S. Gray, J. Ferré, J. Bland, and J. Miltat. *J. Appl. Phys.*, Vol. 78, p. 7210, 1995.
- [Cowb 97] R. Cowburn, S. Gray, and J. Bland. *Phys. Rev. Lett.*, Vol. 79, p. 4018, 1997.
- [Dabo 94a] C. Daboo, R. J. Hicken, D. E. P. Eley, M. Gester, S. J. Gray, A. J. R. Ives, and J. A. C. Bland. *J. Appl. Phys.*, Vol. 75, p. 5586, 1994.
- [Dabo 94b] C. Daboo, R. Hicken, D. Eley, M. Gester, S. Gray, A. Ives, and J. Bland. *J. Appl. Phys.*, Vol. 75, p. 5586, 1994.

- [Diet 00] T. Dietl, H. Ohno, F. Matsukura, J. Cibert, and D. Ferrand. *Science*, Vol. 287, p. 1019, 2000.
- [Diet 01] T. Dietl, H. Ohno, and F. Matsukura. *Phys. Rev. B*, Vol. 63, p. 195205, 2001.
- [Diet 02] T. Dietl. *Semicond. Sci. Technol.*, Vol. 17, p. 377, 2002.
- [Edmo 06] K. Edmonds. We thank K. Edmonds and B. Gallagher from the University of Nottingham for providing this (Ga,Mn)As layer. 2006.
- [Efro 75] A. Efros and B. Shklovskii. *J. Phys. C*, Vol. 8, p. L49, 1975.
- [Ferr 02] J. Ferré. *Spin Dynamics in Confined Magnetic Structures I*, pp. 127–165. (Eds: . Hillebrands and K. Ounadjela), Springer, 2002.
- [Flat 01] M. E. Flatté and G. Vignale. *Appl. Phys. Lett.*, Vol. 78, p. 1273, 2001.
- [Goen 05] S. T. B. Goennenwein, S. Russo, A. F. Morpurgo, T. M. Klappwijk, W. van Roy, and J. de Boeck. *Phys. Rev. B*, Vol. 71, p. 193306, 2005.
- [Goul 04] C. Gould, C. Rüster, T. Jungwirth, E. Girgis, G. Schott, R. Giraud, K. Brunner, G. Schmidt, and L. Molenkamp. *Phys. Rev. Lett.*, Vol. 93, p. 117203, 2004.
- [Goul 06] C. Gould, K. Pappert, C. Rüster, R. Giraud, T. Borzenko, G. M. Schott, K. Brunner, G. Schmidt, and L. W. Molenkamp. *Jpn. J. Appl. Phys.*, Vol. 45, p. 3860, 2006.
- [Goul 07] C. Gould, K. Pappert, G. Schmidt, and L. Molenkamp. *Adv. Mater.*, Vol. 19, p. 323, 2007.
- [Hama 03] K. Hamaya, R. Moriya, A. Oiwa, T. Taniyama, Y. Kitamoto, and H. Munekata. *IEEE Trans. Magn.*, Vol. 39, p. 2785, 2003.
- [Hama 06] K. Hamaya, T. Taniyama, T. Koike, and Y. Yamazaki. *J. Appl. Phys.*, Vol. 99, p. 123901, 2006.
- [Haur 97] A. Haury, A. Wasiela, A. Arnoult, J. Cibert, S. Tatarenko, T. Dietl, and Y. M. d'Aubigné. *Phys. Rev. Lett.*, Vol. 79, p. 511, 1997.
- [Hube 00] A. Hubert and R. Schäfer. Springer, Heidelberg, 2000.
- [Hugh 96] R. J. F. Hughes, A. K. Savchenko, J. E. F. Frost, E. H. Linfield, J. T. Nicholls, M. Pepper, E. Kogan, and M. Kaveh. *Phys. Rev. B*, Vol. 54, p. 2091, 1996.
- [Jan 57] J. P. Jan. (Eds: F. Seitz, D. Turnbull), Academic Press Inc. New York, 1957.
- [Jung 07] T. Jungwirth. private communications. Calculations based on a band structure approach suggest that this opposite sign is related to scattering amplitudes and peculiarities of the (Ga,Mn)As density of states. 2007.

- [Lark 02] A. I. Larkin and B. I. Shklovskii. *phys. stat. sol. (b)*, Vol. 230, p. 189, 2002.
- [Lee 99] M. Lee, J. G. Massey, V. L. Nguyen, and B. I. Shklovskii. *Phys. Rev. B*, Vol. 60, p. 1582, 1999.
- [Liu 05] X. Liu, W. Lim, L. Titova, M. Dobrowolska, J. Furdyna, M. Kutrowski, and T. Wojtowicz. *J. Appl. Phys.*, Vol. 98, p. 63904, 2005.
- [Maha 04] P. Mahadevan, A. Zunger, and D. D. Sarma. *Phys. Rev. Lett.*, Vol. 93, p. 177201, 2004.
- [Mats 04] F. Matsukura, M. Sawicki, T. Dietl, D. Chiba, and H. Ohno. *Physica E*, Vol. 21, p. 1032, 2004.
- [Mats 98] F. Matsukura, H. Ohno, A. Shen, and Y. Sugawara. *Phys. Rev. B*, Vol. 57, p. R2037, 1998.
- [McGu 75] T. R. McGuire and R. I. Potter. *IEEE Trans. Magn.*, Vol. MAG-11, p. 1018, 1975.
- [Mich 02] N. L. Michael, C. U. Kim, P. Gillespie, and R. Augur. Proc. Advanced Metallization Conf., p42, Tokyo, 29-30 Oct. 2002.
- [Mura 88] S. Murarka. in "VLSI Technology" (ed by S.M. Sze), 2nd ed., McGraw-Hill, New York, 1988.
- [OHan 00] R. C. O'Handley. John Wiley and Sons, New York, 2000.
- [Ohno 02] H. Ohno, F. Matsukura, and Y. Ohno. *JSAP International*, Vol. 5, p. 4, 2002.
- [Ohno 96] H. Ohno, A. Shen, F. Matsukura, A. Oiwa, A. Endo, S. Katsumoto, and Y. Iye. *Appl. Phys. Lett.*, Vol. 69, p. 363, 1996.
- [Ohno 98] H. Ohno. *Science*, Vol. 281, p. 951, 1998.
- [Omiy 01] T. Omiya, F. Matsukura, A. Shen, Y. Ohno, and H. Ohno. *Physica E*, Vol. 10, p. 206, 2001.
- [Papp 07] K. Pappert, S. Hümpfner, J. Wensch, K. Brunner, C. Gould, G. Schmidt, and L. Molenkamp. *Appl. Phys. Lett.*, Vol. 90, p. 062109, 2007.
- [Park 05] S. S. P. Parkin. U.S. Patent No. 6,834,005. 2005.
- [Poll 65] F. H. Pollak. *Phys. Rev.*, Vol. 138, p. 618, 1965.
- [Raik 87] M. E. Raikh and I. M. Ruzin. *Sov. Phys. JETP*, Vol. 65, p. 1273, 1987.
- [Rush 06] Rushforth *et al.* *Phys. Stat. Sol. (c)*, Vol. 3, p. 4078, 2006.

- [Rust 03] C. Rüster, T. Borzenko, C. Gould, G. Schmidt, L. Molenkamp, X. Liu, T. Wojtowicz, J. Furdyna, Z. Yu, and M. Flatté. *Phys. Rev. Lett.*, Vol. 91, p. 216602, 2003.
- [Rust 05] C. Rüster, C. Gould, T. Jungwirth, J. Sinova, G. M. Schott, R. Giraud, K. Brunner, G. Schmidt, and L. W. Molenkamp. *Phys. Rev. Lett.*, Vol. 94, p. 027203, 2005.
- [Sand 01] B. Sandow, K. Gloos, R. Rentzsch, A. Ionov, and W. Schirmacher. *Phys. Rev. Lett.*, Vol. 86, p. 1845, 2001.
- [Sawi 04] M. Sawicki, F. Matsukura, A. Idziaszek, T. Dietl, G. M. Schott, C. Rüster, C. Gould, G. Karczewski, G. Schmidt, and L. W. Molenkamp. *Phys. Rev. B*, Vol. 70, p. 245325, 2004.
- [Sawi 05] M. Sawicki, K. Y. Wang, K. Edmonds, R. Champion, C. Staddon, N. Farley, C. Foxon, E. Papis, E. Kamiska, A. Piotrowska, T. Dietl, and B. Gallagher. *Phys. Rev. B*, Vol. 71, p. R121302, 2005.
- [Schm 00] G. Schmidt, D. Ferrand, L. W. Molenkamp, A. T. Filip, and B. J. van Wees. *Phys. Rev. B*, Vol. 62, p. R4790, 2000.
- [Schm 07] M. J. Schmidt, K. Pappert, C. Gould, G. Schmidt, R. Oppermann, and L. W. Molenkamp. to be published; cond-mat/0704.2028 2007.
- [Scho 03] G. Schott, G. Schmidt, G. Karczewski, L.W.Molenkamp, R. Jakiela, and A. Barcz. 2003. The layers where grown by J. Wenisch following the recipe developed by G. M. Schott.
- [Shen 97] A. Shen, H. Ohno, F. Matsukura, Y. Sugawara, N. Akiba, T. Kuroiwa, A. Oiwa, A. Endo, S. Katsumoto, and Y. Iye. *J. Cryst. Growth*, Vol. 175/176, p. 1069, 1997.
- [Slon 96] J. Slonczewski. *J. Magn. Magn. Mater.*, Vol. 159, p. L1, 1996.
- [Ston 48] E. Stoner and E. Wohlfarth. *Phil. Trans. Roy. Soc. A*, Vol. 240, p. 599, 1948.
- [Tang 03] H. X. Tang, R. K. Kawakami, D. D. Awschalom, and M. L. Roukes. *Phys. Rev. Lett.*, Vol. 90, p. 107201, 2003.
- [Tata 04] G. Tataara and H. Kohno. *Phys. Rev. Lett.*, Vol. 92, p. 086601, 2004.
- [vanR 06] W. vanRoy. We thank W. van Roy from IMEC, Leuven, for providing this (Ga,Mn)As layer. 2006.
- [Vert 95] Vertesy and Tomas. *J. Appl. Phys.*, Vol. 77, p. 6425, 1995.
- [Vign 02] G. Vignale and M. E. Flatté. *Phys. Rev. Lett.*, Vol. 89, p. 098302, 2002.
- [Vizi 07] Vizimag. Field line patterns calculated using Vizimag by J. B. Beeteson (www.vizimag.com) 2007.

- [Wang 04] K. Y. Wang, R. P. Campion, K. W. Edmonds, M. Sawicki, T. Dietl, C. T. Foxon, and B. L. Gallagher. presented at the 27th Int. Conf. on the Physics of Semiconductors (ICPS), Flagstaff AZ, USA, July 26-30 2004.
- [Wang 05a] K. Y. Wang, K. Edmonds, L. X. Zhao, M. Sawicki, R. P. Campion, B. Gallagher, and C. Foxon. *Phys. Rev. B*, Vol. 72, p. 115207, 2005.
- [Wang 05b] K. Wang, M. Sawicki, K. Edmonds, R. Campion, S. Maat, C. Foxon, B. Gallagher, and T. Dietl. *Phys. Rev Lett.*, Vol. 95, p. 217204, 2005.
- [Wang 07] K. Y. Wang, A. W. Rushforth, V. A. Grant, R. P. Campion, K. W. Edmonds, C. R. Staddon, C. T. Foxon, B. L. Gallagher, J. Wunderlich, and D. A. Williams. to be published in *J. Appl. Phys.*; arXiv:0705.0474 2007.
- [Welp 03] U. Welp, V. Vlasko-Vlasov, X. Liu, J. Furdyna, and T. Wojtowicz. *Phys. Rev. Lett.*, Vol. 90, p. 167206, 2003.
- [Welp 04] U. Welp, V. K. Vlasko-Vlasov, A. Menzel, H. D. You, X. Liu, J. K. Furdyna, and T. Wojtowicz. *Appl. Phys. Lett.*, Vol. 85, p. 260, 2004.
- [Weni 06] J. Wenisch, L. Ebel, C. Gould, G. Schmidt, L. Molenkamp, and K. Brunner. *MBE2006 Abstract Workbook*, Vol. , p. 63, 2006.
- [Weni 07] J. Wenisch, C. Gould, L. Ebel, J. Storz, K. Pappert, M. Schmidt, C. Kumpf, G. Schmidt, K. Brunner, and L. Molenkamp. *cond-mat/0701479*, 2007.
- [West 60] F. West. *Nature*, Vol. 188, p. 129, 1960.
- [Wojt 86] T. Wojtowicz, T. Dietl, M. Sawicki, W. Plesiewicz, and J. Jarozynski. *Phys. Rev. Lett.*, Vol. 56, p. 2419, 1986.
- [Wund 06] J. Wunderlich, T. Jungwirth, B. Kaestner, A. C. Irvine, A. B. Shick, N. Stone, K.-Y. Wang, U. Rana, A. D. Giddings, C. T. Foxon, R. P. Campion, D. A. Williams, and B. L. Gallagher. *Phys. Rev. Lett.*, Vol. 97, p. 077201, 2006.
- [Wund 07] J. Wunderlich, T. Jungwirth, A. C. Irvine, J. Zemen, A. W. Rushforth, E. D. Ranieri, U. Rana, K. Vyborny, J. Sinova, C. T. Foxon, R. P. Campion, D. A. Williams, and B. L. Gallagher. *unpublished*, 2007.
- [Xian 05] G. Xiang, A. Holleitner, B. Sheu, F. M. O. Maksimov, M. Stone, P. Schiffer, D.D.Awschalom, and N. Samarth. *Phys. Rev. B*, Vol. 71, p. 1307, 2005.
- [Yama 04] M. Yamanouchi, D. Chiba, F. Matsukura, and H. Ohno. *Nature*, Vol. 428, p. 539, 2004.
- [Zung 05] A. Zunger. presented at Int. Workshop on Wide Band Gap Ferromagnetic Semiconductors 2005.





# Acknowledgements

There are lots of people I would like to thank for their contributions to this work.

- I would like to express my gratitude to Prof. Laurens W. Molenkamp the head of the EP3 chair and PD Dr. Georg Schmidt the leader of the spintronics group for giving me the opportunity to work in their group and for all the discussions, guiding and support.
- Very special thanks to Dr. Charles Gould. It was great to work with you all the time. Thank you for all the inspiring discussions, for the numerous hours we spend in the lab and in the office, and last but not least for many insightful comments on the draft for this thesis.
- Thanks to Jan Wenisch and Giesela Schott for growing the (Ga,Mn)As wafers. And special thanks to Silvia Hümpfner and Tanja Borzenko, but also to Kia Tavakoli, Stefan Mark, Marcel Zimmerman and Volkmar Hock for sample fabrication and for solving all the little clean-room mysteries.
- Thanks to Christian Rüster and many other former PhD students for setting up our transport labs and teaching me how to use the equipment. Thanks also for many scientific and non-scientific discussions.
- Thanks to Manuel Schmidt for many insightful theory discussions.
- Special thanks to Dr. Mike Sawicki from Institute of Physics, Polish Academy of Sciences (IFPAN), Warsaw and many other Nanospin consortium members.
- Not to forget many other people who contributed to discussions, measurement setups, sample fabrication and measurements: Roland Ebert, the mechanics and electronics workshop team, Gert Manger, Marcel Zimmermann, Olivier Rival, Lars Ebel, Jan Storz, Dietrich Roth, Ralf and Michael Scheibner, Bastian Büttner, Andreas Riegler, Tobias Kiessling, Claus Schumacher, Greg Karczewski and everyone else from EP3.
- Financial support from the European Union (NANOSPIN FP6-IST-015728) and the German DFG (SFB 410) is gratefully acknowledged.
- Last but not least I would like to thank my family, my parents and Benno, for their caring support.



# Lebenslauf

Katrin Pappert

geboren in Mühlhausen 15. Mai 1980

- 1986 bis 1991 Besuch der Polytechnischen Oberschule 10 in Mühlhausen
- 1991 bis 1994 Besuch des Albert-Schweitzer-Gymnasiums in Mühlhausen
- 1994-1998 Besuch des math.-naturwissenschaftlichen Spezialschulteils  
des Albert-Schweitzer-Gymnasiums in Erfurt  
Abschluß Abitur
- 1998-1999 Studium Maschinenbau, TU Ilmenau
- 1999-2004 Studium Technische Physik, TU Ilmenau  
Abschluß Diplom-Ingenieur
- seit 2004 Promotionsstudium am Lehrstuhl EP3 (Prof. L.W.Molenkamp)  
der Julius-Maximilians-Universität, Würzburg

